MICROMACHINED ACCELEROMETER BASED ON DIFFERENTIAL MEASUREMENT OF AIR MOVEMENT

by

Maria Pascal

M.Physics(honours), University of Bucharest, Romania, 1982

A THESIS SUBMITTED IN PARTIAL FULFILLMENT OF THE

REQUIREMENTS FOR THE DEGREE OF

MASTER OF APPLIED SCIENCES

in the

School of Engineering Science

SIMON FRASER UNIVERSITY

November 1996

Approval

Name: Maria Pascal

Degree: Master of Applied Sciences

Title of Thesis: Micromachined Accelerometer Based on Differential Measurement of Air Movement

Examining Committee:

Chairman: Dr. Jamal Dean

Dr. Albert Leung
Senior Supervisor

Dr. M. Parameswaran
Supervisor

Dr. John Jones
Supervisor

Dr. Andrew Rawicz
Supervisor

Dr. Glenn Chapman
Examiner

Date Approved: November 6, 1996

PARTIAL COPYRIGHT LICENSE

I hereby grant to Simon Fraser University the right to lend my thesis, project or extended essay (the title of which is shown below) to users of the Simon Fraser University Library, and to make partial or single copies only for such users or in response to a request from the library of any other university, or other educational institution, on its own behalf or for one of its usrs. I further agree that permission for multiple copying of this work for scholarly purposes may be granted by me or the Dean of Graduate Studies. It is understood that copying or publication of this work for financial gain shall not be allowed without my written permission.

Title of Thesis/Project/Extended Essay

"Micromachined Accelerometer Based on Differential Measurement of Air Movement"

Author:

_____
(signature)

Maria Pascal
(name)

August 30, 1996
(date)

Abstract

In recent years the demand for a simple, robust and reliable integrated accelerometer has stimulated research activities at numerous organizations. This thesis investigates the possibility of fabricating a new class of accelerometers that work on the principle of air movement measured in a differential fashion. This measurement technique is a patent pending idea of Dr. Albert Leung of the School of Engineering Science, Simon Fraser University.

Device modeling, design, fabrication and characterization are presented. The device configuration is based on the "hot air bubble" concept developed by Dr.Albert Leung . The device consists of a central heater and temperature sensors placed symmetrically on its sides with surrounding air as thermal coupling element.

The less dense "hot air bubble" generated by the heater will be shifted by an applied acceleration, due to buoyancy force. The symmetrically placed sensors will sense the bubble movement in a differential manner, providing an output that is proportional to the applied acceleration. The advantages of this new device over those of existing accelerometers are its simplicity and robustness. These advantages result from the device having no solid moving parts.

The heater and the sensors are thermally isolated resistors on suspended bridges lying in the same plane. The devices were designed and fabricated using bulk micromachining technique.

Analytical models of the device functional blocks were developed to gain an insight into the device behavior. The analytical model results were used to derive guidelines on device dimensions. Based on analytical solutions, the temperature distribution, heat flow and response time were calculated.

The air temperature distribution is also determined using an ANSYS simulator. Streamlines and isotherms for air flow within the system are presented. The air flow regimes that arise are determined as a function of device geometry and temperature. The numerical results are compared with the analytical model results in order to check the validity of proposed analytical models.

The device was characterized by measuring the device parameters : linearity, dynamic range, frequency response, sensitivity and resolution. Further research work is required for device optimization.

Acknowledgments

I would like to thank my senior supervisor, Dr. Albert Leung for his help and enthusiasm, Dr. Ash Parameswaran for his assistance in device fabrication and Dr.Andrew Rawicz for his help in device frequency response measurements. My gratitude and special thanks go to Dr. John Jones for his help in the simulation of device thermal behavior and for making me step above the mathematical complexity of natural convection phenomena and to understand them.

My appreciation goes to the members of the Micromachining and Microelectronics Lab for their useful suggestions and sustained support. I would like also to acknowledge the contributions of Mr.Bill Woods, Dr.Eva Czyzewska and Mr.Jianming Chen in device fabrication.

Special thanks to all those who helped me with computing systems and lab experiments.

Table of Contents

List of Figures

List of Tables

List of Symbols

a = acceleration

A = area

A_v = circuit gain

B = buoyancy force

Bi = Biot number

C = coefficient

c_p = specific heat

c_c = critical damping

D = diameter

d = depth

E = Young's modulus

E_a = activation energy

F = force

F_d = drag force

F_o = Fourier number

f = frequency

f_n = natural resonant frequency

Gr = Grashoff number

G = gauge factor

g = earth gravity

g_l = units of earth gravity (g level)

h = convective heat transfer coefficient

H = heater

I = electric current

I_m = moment of inertia

J = current density

k = thermal conductivity

k_e = equivalent spring constant

L = length

L_C = characteristic dimension

L_{eff} = effective length

m = mass

M = magnification factor

Nu = Nusselt number

P_e = electric power

P = perimeter

p = pressure

Pr = Prandtl number

Q = heat flow

q = heat flux

Ra = Rayleigh number

r = radius ; radial distance

R = electric resistance

R_{th} = thermal resistance

Re = Reynold's number

S = sensitivity

s = distance, space

t = time ; thickness

T = temperature

TCR= temperature coeffcient of resistance

u = velocity

U = voltage

w = width

v = specific volume

V = volume

V_H = heater voltage supply

V_B = bridge voltage supply

x = displacement

X = displacement amplitude

x_m = length scale over which longitudinal conduction is sensed

Z = measurement resolution

α = thermal diffusivity

β = coeffcient of the volume expansion of the fluid

γ = kinematic viscosity

μ = absolute viscosity

ς = damping factor

ω = angular frequency

Φ = phase of displacement

τ = time constant

δ = boundary layer thickness

δ_t = thermal boundary layer thickness

δ_{st} = statical deflection

ρ = density

ρ_e = electrical resistivity

σ = stress

ε = strain

Thesis Organization

In the past few years, research interest in techniques for fabricating silicon micromachined devices has been high. Micromachined devices exhibit the advantages of reduced dimensions and mass, batch fabrication and easy interfacing or even integration with electronic circuits.

Two major classes of micromachined devices can be identified: sensors and mechanical components or systems, such as motors and graspers.

Thermal sensors measure physical quantities by transducing their signals into thermal quantities first and then transducing the thermal quantities into electrical quantities. Thermal sensors can be air flow, acceleration or infrared sensors, for example. For optimum operation of a thermal sensor, a good thermal and electrical isolation of a sensor from its substrate is desirable. This isolation is accomplished either by bulk or by surface micromachining.

In bulk micromachining, the sensors are shaped by anisotropic etching of a large single-crystal substrate. Thin films are patterned on the surface to provide isolation and transducer functions. The technique of using lithographic process and exposing monocrystalline silicon to anisotropic etchants to produce concave, pyramidal or other faceted holes in Si is known as "bulk micromachining". Suspended structures such as cantilever beams, platforms and bridges can be generated using this technique.

Most of the published thermal sensor structures used to measure accelerations [1, 6, 12, 19, 20, 33, 36] consist of a cantilever beam whose displacement as a function of applied acceleration is determined from a temperature difference registered by a temperature sensor placed on the beam.

This thesis investigates the possibility of fabricating a new type of thermal accelerometer based on differential measurement of air movement. The device configuration is based on Dr. Albert Leung's innovative "hot air bubble "concept [2]. The system consists of a central heater and two temperature sensors placed symmetrically on the heater's sides. The heater and the sensors are thermally isolated resistors on suspended bridges fabricated using the bulk micromachining technique. The surrounding air is the thermal coupling element. The heater will generate a less dense "hot air bubble". When accelerated, the "hot air bubble" will shift due to buoyancy force. The symmetrically placed sensors will sense the bubble movement as a difference between their temperatures, providing the device output. The advantages of this new device over those of existing accelerometers are its simplicity, robustness and wide acceleration range. These advantages derive from a lack of solid moving parts.

Device modeling, design, fabrication and characterization are presented in the following chapters. The device's working principle detailed description and a discussion on materials selection for temperature sensors are in Chapter 1. Chapter 2 covers theoretical analysis of the proposed device consisting of analytical models for steady-state and transient behavior. The analytical solutions for simplified device's representations are used to evaluate temperature distribution, heat flow and device's response time. The calculated values are compared with numerical simulation and measurement results. The air temperature distribution is determined using an ANSYS simulator. Streamlines and isotherms for air flow within the system are also presented. Air flow regimes that arise are determined as a function of device geometry and temperature.

The device layout and process design are presented in Chapter 3. The device characterization was accomplished by measuring the device parameters: linearity, dynamic range, frequency response, resolution and sensitivity. The measurement set-up and results are presented in Chapter 4. Possible applications and several conclusions are drawn in Chapter 5.

Chapter 1. Device Outline

1.1. Principle

The most popular Si based micromachined accelerometers to date are thermal and capacitive sensors. All published approaches use the motion of a solid element, cantilever beam or a combdrive, as primary detection means. The present accelerometer structure uses hot air movement.

The proposed accelerometer is a thermal sensor which consists of a central heater with two symmetrically placed temperature detectors besides it. With a constant voltage supply, V_H, the heater, H, heats up the surrounding air, creating a "hot air bubble" [2]. The "hot air bubble" is a hot air cylinder concentric with the heater, having its radius, r_c. much larger than the heater radius, r_h. Given no air flow or disturbance, the differential measurement at the two detectors is expected to yield a zero output due to device symmetry. An applied acceleration would distort the symmetry, as the air bubble moves. A differential temperature measurement of the two sensors, SNZ, provides the device output. The schematic representation of the device is given in Fig.1.

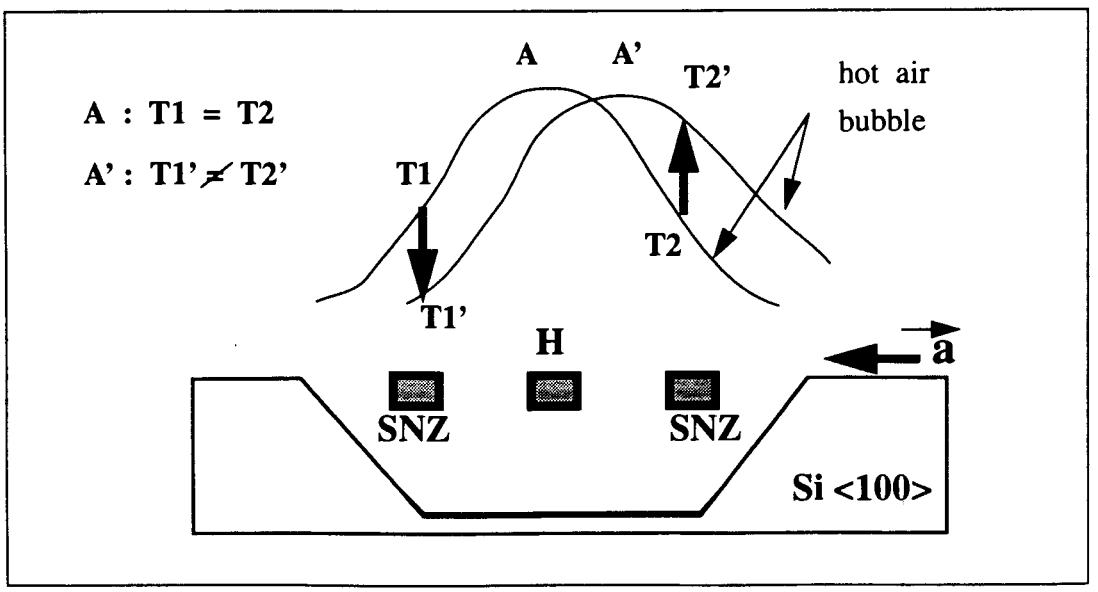

Fig.1 Schematic representation of device's working principle

A thermal sensor is a tandem transducer [1]. It operates in three steps. First, the non-thermal signal, acceleration $\bar{\mathbf{a}}$, is transduced into a heat flow, Q. At equilibrium, the central heater generates a hot air bubble with symmetrical temperature distribution. An applied acceleration would cause the hot air bubble to move in opposite direction so that extra heat is transferred to one of the sensors. Second, the heat flow will be converted into a temperature difference, dT. The amount of transferred extra heat is a measure of mechanical-to-thermal transduction efficiency

The temperature detectors for the proposed structure are equally separated, suspended bridges. Each bridge is a line resistor with a temperature coefficient of resistance, TCR. Due to their temperature coefficient, the detectors will register the extra heat as an imbalance, dT, between their temperatures. Third, the temperature difference, dT, is transduced into an electrical signal, dV.

This is usually accomplished using a Wheatstone bridge configuration [1]. The relative resistance change, dR/R_o, due to dT will be seen as a voltage difference, dV. The magnitude of dV corresponds to thermal-to-electrical transduction efficiency. The air provides the thermal coupling between the heater and the temperature sensors.

The resulting dV is thus a function of applied acceleration, device's materials and geometry. For a constant voltage operated Wheatstone bridge, the differential output voltage is given by the product of resistance's temperature coefficient, TCR, and bridge voltage supply, V_B, for a unit temperature change at detectors. Hence the bridge response to a temperature change will increase for increased TCR and V_B. The device's speed of response to an applied acceleration is dependent on resistor's specific heat and size and rate of temperature change at detectors.

1.2. Materials

Temperature sensors rely on good thermal and electrical isolation of the sensor from its substrate.

An anisotropic Si etching process is used to create free standing structures which offer a very good thermal isolation from the substrate. Two approaches have been used to fabricate resistors as temperature detectors. For the first design, diffused resistors were made out of heavily boron-doped diffused Si layers. For the second design, polySi resistors lying on suspended SiO_2 stripes were fabricated. The later exhibit both good thermal and electrical insulation. The thermal conductivity of silicon dioxide is 1.5W/m^{o}C while its resistivity is 10^{12} ohm. cm [1]. SiO_2 is a good thermal and electrical isolator. Thermal conductivity of resistor's material will influence the longitudinal heat transfer between suspended bridges and substrate.

For a temperature sensor, the characteristics of interest are its temperature sensitivity and speed of response. When resistors are used as temperature sensors, their temperature coefficient and specific heat are the material properties which dictate the sensor sensitivity and speed of response, respectively.

Thermal conductivity, k, specific heat, c_p, electrical resistivity, ρ_e and temperature coefficient of resistance, TCR, values for some common materials used in microelectronics processing are given in Table1.

Table 1: Some materials properties

					observations
materials	Pt, Pa, Au, W	Mo, Ag	Ni, Cr	Si, Al, Ti	
specific heat, c_p [J / kg^{o}K]	130-150	230-250	~ 450	> 650	low c_p desirable for fast device response
materials	Au, Al, Ag	Ni,Mo,Pt,W	Cr,Pa,Ta	Ti	

Table 1: Some materials properties

					observations
resistivity, [μohm.cm]	1- 3	5-10	10-15	> 40	higher values allow higher V_B, bridge voltage
materials	Ti	Cr, Ni, Pt, Ta	Mo, Si, W	Al, Au,Ag, Cu	
thermal conductivity, k [W / m^{o}K]	~ 22	60 - 90	130 - 180	> 230	lower k values desirable for better accuracy
materials	Mo, Ti, W, Cr	Al, Pt, Ti	Ni, Au	-	
temp.coeff of resistance, TCR, [$^oC^{-1}$]	~ 0.003	~ 0.004	0.007 - 0.008	-	higher TCR values allow higher sensitivity
materials	Ti	Ni, Ag	Mo, Au,	-	
density, [g / cm^3]	~ 5	~ 10	16-20	-	

1.2.1. Resistivity

The resistor's resistivity and size determine the final resistance value, thus the maximum allowable bridge voltage supply. Hence higher sensor's resistivity is desirable as outlined in Section 1.1. Thin film resistors made out of refractory metals would exhibit relatively high electrical resistivity. Thermometers made out of W, Ni resistors were reported [6,13]. Metal resistors have the disadvantage of low electric resistance as compared with Si or polySi resistors. The resistivity of doped polySi is always higher than that of single-crystal material for the same impurity concentration level [37]. The highest resistance value can be thus obtained with polySi resistors.

As for heater materials, high resistivity, melting point and low thermal conductivity would be

desirable. Ti shows these features and has the advantage of compatibility with IC processing. Its adhesion properties to SiO_2 and its compatibility with anisotropic etchants are also of great importance.

Next to the resistivity, of particular importance for sensors which operate through a change in their electrical characteristics are the temperature coefficient of resistance, TCR, the strain sensitivity (gauge factor), G, and the long term stability of the resistor.

1.2.2. Temperature Coefficient of Resistance (TCR)

The metals generally have a negative TCR. Ni and Au have the highest TCR (0.007 - 0.008) $^{o}C^{-1}$ as compared with Pt, Ti, Cr and Mo (0.003 - 0.004) $^{o}C^{-1}$.

Even gold has high TCR and low specific heat, hence it would be a fast and sensitive thermometer, it has the disadvantage of high thermal conductivity and very low electrical resistivity. High thermal conductivity would determine less accurate temperature measurement while low electrical resistivity would determine low measurement resolution.

As compared with Au, Ni shows same TCR, higher resistivity and lower thermal conductivity. Thus Ni exhibits the same sensitivity as Au and has the advantage of more precise temperature reading. It might allow higher (about three times) V_B but it'll have slower (about three times) speed response. Hence Ni would be as sensitive as Au, more accurate and slower than Au.

Pt has similar properties to Ni but lower TCR (about two times), lower c_p(about the same as Au), thus it would be as fast as Au but less sensitive temperature sensor. Pt is better than W because it has a lower k, similar other properties, thus it could provide a more precise temperature reading.

Cr has a TCR similar to that of Pt or W and about a two times lower TCR value as compared with Ni. Cr exhibits higher resistivity (about two times) than Ni, Pt and similar k, c_p to Ni. Thus Cr would be as sensitive as a Pt thermometer with two times higher V_B(measurement resolution) and slower (about three times) response time.

It can be concluded that Ni is as sensitive as Au, while Pt is as fast as Au, without associated disadvantages to Au thermometers. Unlike refractory metals, Si has positive TCR values between [0 - 0.002]$^oC^{-1}$, which are fairly constant over a wide temperature range.

The TCR of B-doped polySi layer over a specified temperature range is a function of doping concentration, grain size and trap state [6,14]. The external stress and non-ohmic contact resistance are extrinsic factors which can also change the temperature dependence. The TCR for B-doped polySi exhibits the following features:

i) the TCR can be selected + or - through selective doping; it is + for high doping levels

ii) the resistance change with temperature is not linear; there is a limited temperature range over which TCR can be assumed constant

iii) the temperature dependence increases with decreasing doping concentration

iv) a decrease in grain size at same doping concentration will correspond to a shift to high doping levels

The TCR values for B-doped polySi are between -0.025 $^oC^{-1}$ and 0.002 $^oC^{-1}$[14].

1.2.3. Strain Sensitivity

A resistance change can be also caused by a mechanical deformation. There is a relative resistance change of B-doped polySi resistors under stress conditions for longitudinal strain, e_l [17,37]. The resistance decreases with compression and increases under tension. The resistance change with strain decreases with increasing doping concentration. This relationship is equivalent

in principle to that of single-crystal silicon. Hence possible bridge mechanical deformations might induce unwanted resistance changes.

1.2.4. Compatibility with Anisotropic Etchants

It was reported that Au, Cr, Ag and Cu are resistant to EDP [1] while W is not etched in 44%KOH at 70°C. It was also reported [13] that Cr, Au are resistant to KOH / water (1:2 by weight) at 75 ° C. I have determined experimentally that Ni is also resistant to EDP; no measurable thickness difference (alpha-step profilometer) could be observed after 12 hours in EDP at 95°C for starting Ni thickness of 3500Å. Because Cr, Ni, Pt have low thermal conductivity, relatively high TCR and are compatible with anisotropic etchants, they are potentially good temperature readers.

Heavily B-doped silicon layers with doping concentration levels > 7 x 10^{19} cm^{-3} are resistant to EDP while layers with doping concentration levels > 1 x 10^{20} cm^{-3} are resistant to hydrazine [1].

PolySi is not resistant to anisotropic etchants and it has to be protected by SiO_2, Si_3N_4 or other EDP / hydrazine resistant layers [21].

Chapter 2. Theoretical Analysis

2.1. Definition of Terms

The three heat transfer mechanisms are conduction, convection and radiation. In this analysis heat transfer by radiation will be neglected.

The heat conduction is governed by Fourier's Law [6-11]. The heat is conducted inside a simple or composite body from a region with higher temperature towards a region with lower temperature. The heat flux, q, is proportional to the temperature gradient:

$$q = -k\nabla T \tag{1}$$

where: q=heat flux, $\left[\frac{W}{m^2}\right]$

k=thermal conductivity, $\left[\frac{W}{(m^2 \cdot K)}\right]$

T=temperature, $[K]$

The thermal conductivity varies with temperature for both gases and solids [8, 11].

The convection of heat is governed by Newton's Law of Cooling [6-11]. The heat flux is proportional to the temperature difference between a body and its surroundings:

$$q = -h\Delta T \tag{2}$$

where h =convective heat transfer coefficient, $\left[\frac{W}{(m^2 \cdot K)}\right]$

For hot bodies immersed in fluids, a temperature distribution will exist in the fluid due to conduc-

tive heat transport [7-9,11]. Fluids with temperature-dependent densities will give rise to a density field. If ρ_∞ is the fluid's reference density, then there will be a local region of lower density, ρ (Fig.2). The density difference can be expressed as a function of the coefficient of volume expansion of the fluid, β,

$$\beta = \frac{1}{v}\left(\frac{\partial v}{\partial T}\right)_p = \frac{1}{v_\infty}\cdot\frac{(v - v_\infty)}{T - T_\infty} = \frac{(\rho_\infty - \rho)}{\rho\,(T - T_\infty)} \qquad (3)$$

where v=specific volume

For ideal gases:

$$pv = RT \quad , \quad R\text{=universal gas constant}$$

and thus:

$$\beta = \frac{1}{v}\cdot\frac{\partial}{\partial T}\left(R\frac{T}{p}\right)_p = \frac{R}{pv} = \frac{1}{T_\infty} \qquad (3a)$$

Such a fluid in a gravitational field of strength g will present a hydrostatic gradient:

$$\frac{dp}{dx} = -\rho g \qquad \text{(instantaneous local values)}$$

which is not the same at various locations because of density dependance on position, $\rho\,(x)$.

If $\rho_\infty > \rho$, then: $\left|\frac{dp_\infty}{dx}\right| > \left|\frac{dp}{dx}\right|$

The difference in pressure gradient drives the fluid motion. A buoyancy force (B(x,y) in Fig.2) is defined [8] as the difference between the two body forces:

$$B = \frac{dp_a}{dx} - \frac{dp}{dx} = g\,(\rho_\infty - \rho) \qquad (4)$$

This force is positive if the resulting flow is upwards.

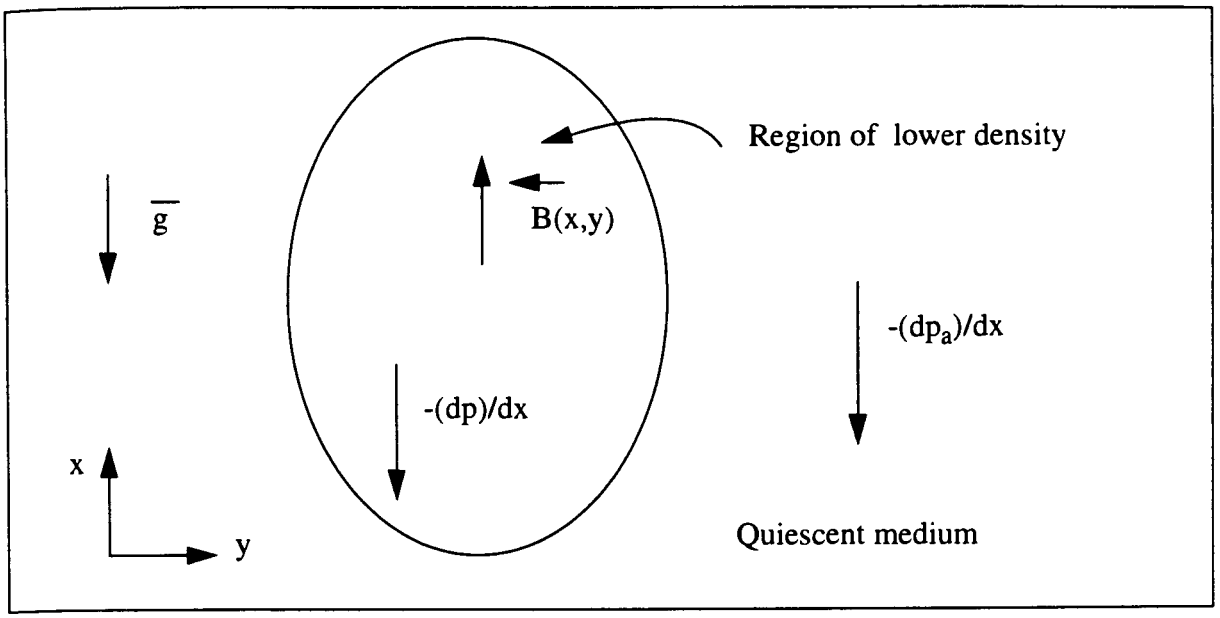

Fig.2 Density disturbance and the resulting transport in a quiescent medium for which $\rho = \rho(T, p)$. The quiescent ambient medium density in this figure is $\rho_\infty = \rho_\infty(T_\infty, p_\infty)$

By substituting eq.(3) in eq.(4), the buoyancy force becomes:

$$B = g\rho\beta(T_S - T_\infty) \tag{5}$$

for an object at a temperature T_S immersed into a fluid at a temperature T_∞, $T_S > T_\infty$.

Thus the buoyancy force can be expressed in terms of the variables β, g and ΔT. These three variables, as well as a linear dimension characteristic of the system, L_C, and fluid properties ρ, μ, c_p, k must be considered in a dimensional analysis.These values will determine, in a first approximation, the system's behavior based on relative importance of viscous or buoyant effects.

2.1.1. Some Useful Quantities

According to Buckingham's Pi theorem [6-11], for n independent variables in a problem with these variables having m dimensions, there will be n-m dimensionless numbers, composed from

the available variables, to characterize the problem. The following dimensionless numbers are sufficient to correlate data for heat transfer in natural convection:

$$\Pi_1 = h\frac{L}{k} = N_{uL}$$

$$\Pi_2 = c_p \cdot \frac{\mu}{k} = P_r$$

$$\Pi_3 = \frac{\beta \cdot g \cdot \rho^2 (T_S - T_\infty) L^3}{\mu^2} = G_{rL}$$

where:

N_{uL}=Nusselt number

P_r=Prandtl number

G_{rL}=Grashof number.

Their physical significance is as follows:

Prandtl number

$$P_r = \frac{molecular'diffusion'of'momentum}{molecular'diffusion'of'thermal'energy} = \frac{\gamma}{\alpha}$$

with $$P_r = \frac{c_p \cdot \mu}{k} = \frac{c_p}{k}\left(\frac{\gamma}{\rho}\right) = \gamma \cdot \frac{1}{\frac{k}{c_p \cdot \rho}} = \frac{\gamma}{\alpha} \qquad (6)$$

For air $P_r = 0.7$. For gases it depends weakly on temperature.

From Prandtl number definition it is apparent that it controls the relation between the velocity and the temperature distributions.

The region where the thermal transport takes place is defined as thermal boundary layer, δ_t. The

region where the momentum transport takes place is defined as boundary layer, δ, or velocity layer. The two quantities are related to Prandtl number by:

$$\frac{\delta}{\delta_t} = \sqrt{P_r}$$

For air, $\frac{\delta}{\delta_t} = 0.8$ [11]. Thus thermal boundary layer is larger than velocity layer. Buoyancy force penetrates out of velocity layer as far as the temperature does and causes motion. It can be concluded that δ_t and δ remain locked together as δ_t increases. This does not occur in forced flows.

Grashof number

$$G_r = \frac{buoyancy'force'effects}{viscous'force'effects} = \frac{\beta \cdot g \cdot \rho\,(T_S - T_\infty)\,L}{\left[\mu \cdot \frac{\nu}{L}\right]}$$

Since $\beta \cdot g \cdot \rho\,(T_S - T_\infty)$ is the buoyancy force per unit volume (eq.5), then $\beta \cdot g \cdot \rho\,(T_S - T_\infty)\,L$ would be the buoyancy force per unit area. Thus the ratio of buoyancy to shear force per unit area is $\frac{\beta \cdot g \cdot \rho\,(T_S - T_\infty)\,L}{\left[\mu \cdot \frac{u}{L}\right]}$, where u is the fluid velocity, $\left[\frac{m}{s}\right]$, a dependent variable proportional to $\frac{\mu}{\rho L}$. Hence, the ratio becomes:

$$G_{rL} = \frac{\beta \cdot g \cdot \rho^2\,(T_S - T_\infty)\,L^3}{\mu^2} \qquad (7)$$

In order to get an estimation of the small buoyancy induced velocities, it is useful to define the unit Grashof number:

$$G_{r1} = \frac{gL^3}{\gamma^2} \tag{8}$$

From eq.(8) we have:

$$G_{rL} = \beta \cdot g \cdot (\Delta T) L^3 \cdot \frac{\rho^2}{\mu^2} = \frac{g \cdot \beta (\Delta T) L^3}{\gamma^2} = (\beta \Delta T) G_{r1} = \frac{\Delta \rho}{\rho} \cdot G_{r1}$$

and thus:

$$G_{rL} = \frac{\Delta \rho}{\rho} \cdot G_{r1} \tag{9}$$

The unit Grashof number allows us to see the relative density change as units of buoyancy force. Based on a rough estimation of buoyancy induced velocities, the qualitative influence of relative density change is given in Fig.3.

It can be seen that for the same system's characteristic dimension, L_C, the relative fluid density change at a given temperature will determine the fluid velocity range.

The relative fluid density change is:

$$\frac{\Delta \rho}{\rho} = \frac{\rho - \rho_\infty}{\rho_\infty} = \frac{T - T_\infty}{T_\infty}$$

The characteristic dimension, L_C, for various geometries is:

cylinder.....D=diameter

horizontal concentric annuli.....d=gap=$D_{outer} - D_{inner}$

horizontal plate..... $\frac{wl}{2(w+l)} = \frac{w}{2}$, $l \gg w$, where l=length, w=width.

In the case of horizontal concentric annuli for $D_o \gg 2D_i$, free cylinder case may be considered [8].

Nusselt number

$$N_u = \frac{convection' effects}{conduction' effects} = \frac{hL_C}{k} \tag{10}$$

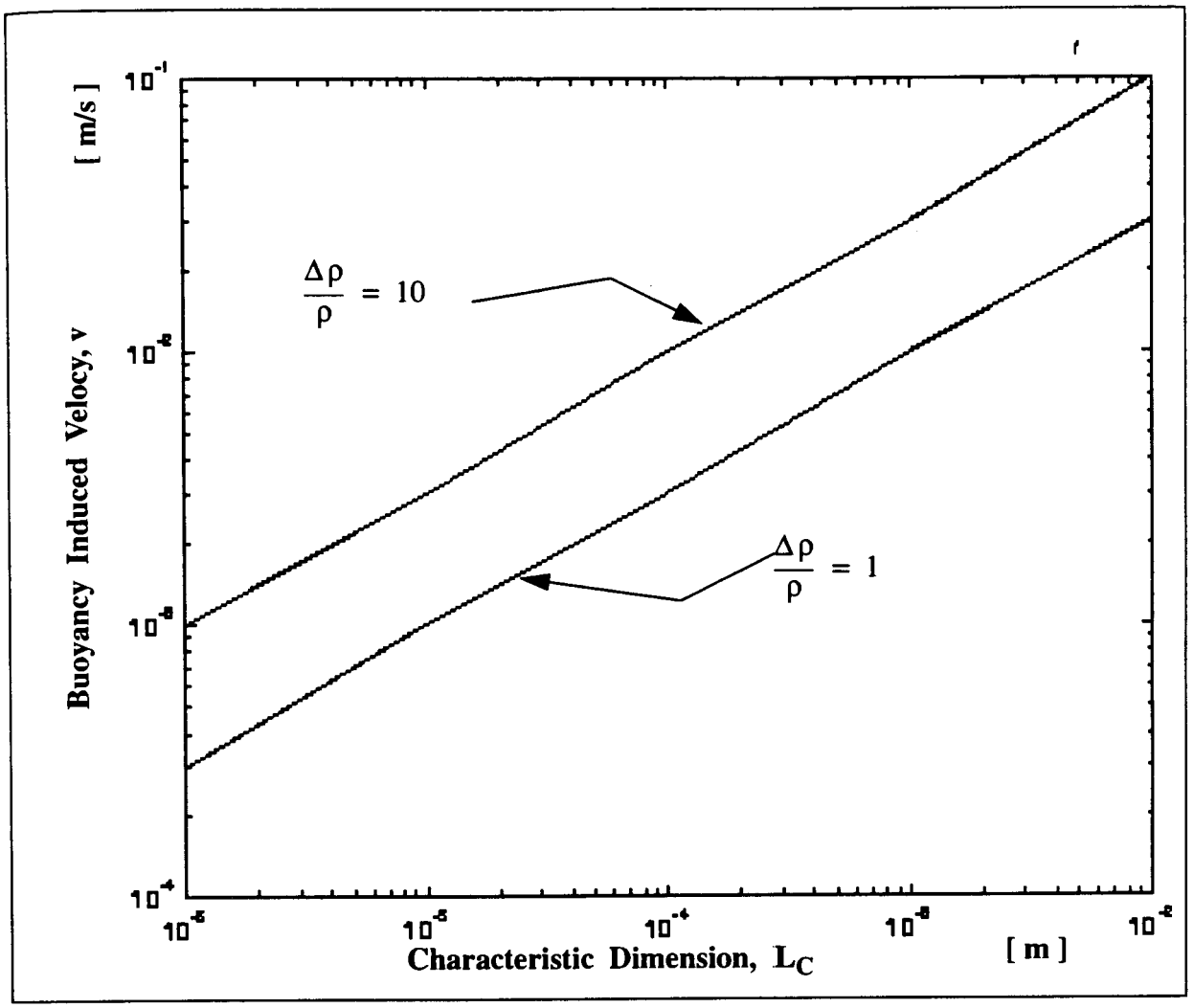

Fig.3 The influence of relative density change on buoyancy induced velocities

where $h = \dfrac{q}{A_S \cdot \Delta T}$ = convective heat transfer coefficient, q =heat flow rate, $\left[\dfrac{W}{m^2}\right]$,

A_S=convective surface area and ΔT=temperature difference between body and ambient.

The Nusselt number is unity if the process is one of pure conduction across the fluid. It has been found that for natural convection the average Nusselt number is related to the Grashof and Prandtl numbers by an equation of the form [6-11]:

$$\overline{N_{uf}} = consi\,(G_{rf} \cdot P_{rf})^{n} \qquad (11)$$

The subscript f indicates that all physical properties should be evaluated at $T_f = \frac{(T_S + T_\infty)}{2}$. The product $G_r \cdot P_r$ is known as the Rayleigh number, R_a:

$$R_a = \frac{\beta \cdot g \cdot \rho\,(T_S - T_\infty)\,L^3}{\mu \cdot \alpha} = \frac{\beta \cdot g\,(T_S - T_\infty)\,L^3}{\gamma \cdot \alpha} = \frac{\beta \cdot g\,(T_S - T_\infty)\,(L^3 \cdot P_r)}{\gamma^2} \qquad (12)$$

For $10^{-6} < R_a < 10^9$, the average Nusselt number for free convection to and from horizontal cylinders is given by [8,11]:

$$\overline{N_{u\,(D,f)}} = \left[0.6 + 0.387 \cdot \left(\frac{R_a}{\left(1 + (\frac{0.56}{P_{rf}})^{9/16}\right)^{16/9}} \right)^{1/6} \right]^2 \qquad (13)$$

For a given body-fluid system, the convective heat transfer coefficient, h, can be evaluated using eq.(10a) with N_u being given by eq.(13).

2.1.2. Convective Heat Transfer Coefficient

In order to evaluate the convective transfer coefficient, the Nusselt number based on eq.(13) should be calculated first.

For air, with $g = g_{earth} \cdot g_{level}$ and $T_\infty = T_{room}$, Rayleigh number can be rewritten as:

$$R_a = \frac{9.8 \cdot \frac{\Delta T}{300} \cdot L^3}{\gamma \cdot \alpha} \cdot g_{level} \qquad (14)$$

Here g_{level} represents a number of g_{earth} units. An applied acceleration, a, of $1 m/s^2$ will correspond to a g_{level} equal with 0.102, so that $a = g_{level} \times g_{earth} = 0.102 \times 9.8 ms^{-2}$.

Assuming that all fluid properties, α, γ, k, except for density, are constant in respect with temperature, we get:

$$R_a = 5.4253 \cdot 10^7 \cdot (\Delta T)\ (L^3 \cdot g_{level}) \qquad (15)$$

The Rayleigh number values for several characteristic dimensions L_C, g_{level} and ΔT are given in Table2.

Table 2: Rayleigh numbers for isothermal, horizontal, cylindrical bodies in air with constant fluid properties, except for density

L_C [m]	$\Delta T = 1K$	$10K$	$100K$	$200K$	$500K$	$1000K$
	$g_{level} = 10^{-3}$					
10^{-6}	$5.42 \cdot 10^{-14}$	$5.42 \cdot 10^{-13}$	$5.42 \cdot 10^{-12}$	$10.85 \cdot 10^{-12}$	$27.12 \cdot 10^{-12}$	$5.42 \cdot 10^{-11}$
10^{-5}	$5.42 \cdot 10^{-11}$	$5.42 \cdot 10^{-10}$	$5.42 \cdot 10^{-9}$	$10.85 \cdot 10^{-9}$	$27.12 \cdot 10^{-9}$	$5.42 \cdot 10^{-8}$
10^{-4}	$5.42 \cdot 10^{-8}$	$5.42 \cdot 10^{-7}$	$5.42 \cdot 10^{-6}$	$10.85 \cdot 10^{-6}$	$27.12 \cdot 10^{-6}$	$5.42 \cdot 10^{-5}$
	$g_{level} = 10^{-2}$					
10^{-6}	$5.42 \cdot 10^{-13}$	$5.42 \cdot 10^{-12}$	$5.42 \cdot 10^{-11}$	$10.85 \cdot 10^{-11}$	$27.12 \cdot 10^{-11}$	$5.42 \cdot 10^{-10}$
10^{-5}	$5.42 \cdot 10^{-10}$	$5.42 \cdot 10^{-9}$	$5.42 \cdot 10^{-8}$	$10.85 \cdot 10^{-8}$	$27.12 \cdot 10^{-8}$	$5.42 \cdot 10^{-7}$
10^{-4}	$5.42 \cdot 10^{-7}$	$5.42 \cdot 10^{-6}$	$5.42 \cdot 10^{-5}$	$10.85 \cdot 10^{-5}$	$27.12 \cdot 10^{-5}$	$5.42 \cdot 10^{-4}$
	$g_{level} = 10^{-1}$					

Table 2: Rayleigh numbers for isothermal, horizontal, cylindrical bodies in air with constant fluid properties, except for density

L_C [m]	$\Delta T = 1K$	$10K$	$100K$	$200K$	$500K$	$1000K$
10^{-6}	$5.42 \cdot 10^{-12}$	$5.42 \cdot 10^{-11}$	$5.42 \cdot 10^{-10}$	$10.85 \cdot 10^{-10}$	$27.12 \cdot 10^{-10}$	$5.42 \cdot 10^{-9}$
10^{-5}	$5.42 \cdot 10^{-9}$	$5.42 \cdot 10^{-8}$	$5.42 \cdot 10^{-7}$	$10.85 \cdot 10^{-7}$	$27.12 \cdot 10^{-7}$	$5.42 \cdot 10^{-6}$
10^{-4}	$5.42 \cdot 10^{-6}$	$5.42 \cdot 10^{-5}$	$5.42 \cdot 10^{-4}$	$10.85 \cdot 10^{-4}$	$27.12 \cdot 10^{-4}$	$5.42 \cdot 10^{-3}$
	$g_{level} = 1$					
10^{-6}	$5.42 \cdot 10^{-11}$	$5.42 \cdot 10^{-10}$	$5.42 \cdot 10^{-9}$	$10.85 \cdot 10^{-9}$	$27.12 \cdot 10^{-9}$	$5.42 \cdot 10^{-8}$
10^{-5}	$5.42 \cdot 10^{-8}$	$5.42 \cdot 10^{-7}$	$5.42 \cdot 10^{-6}$	$10.85 \cdot 10^{-6}$	$27.12 \cdot 10^{-6}$	$5.42 \cdot 10^{-5}$
10^{-4}	$5.42 \cdot 10^{-5}$	$5.42 \cdot 10^{-4}$	$5.42 \cdot 10^{-3}$	$10.85 \cdot 10^{-3}$	$27.12 \cdot 10^{-3}$	$5.42 \cdot 10^{-2}$
	$g_{level} = 5$					
10^{-6}	$27.12 \cdot 10^{-11}$	$27.12 \cdot 10^{-10}$	$27.12 \cdot 10^{-9}$	$5.42 \cdot 10^{-8}$	$135.63 \cdot 10^{-9}$	$27.12 \cdot 10^{-8}$
10^{-5}	$27.12 \cdot 10^{-8}$	$27.12 \cdot 10^{-7}$	$27.12 \cdot 10^{-6}$	$5.42 \cdot 10^{-5}$	$135.63 \cdot 10^{-6}$	$27.12 \cdot 10^{-5}$
10^{-4}	$27.12 \cdot 10^{-5}$	$27.12 \cdot 10^{-4}$	$27.12 \cdot 10^{-3}$	$5.42 \cdot 10^{-2}$	$135.63 \cdot 10^{-3}$	$27.12 \cdot 10^{-2}$
	$g_{level} = 10$					
10^{-6}	$5.42 \cdot 10^{-10}$	$5.42 \cdot 10^{-9}$	$5.42 \cdot 10^{-8}$	$10.85 \cdot 10^{-8}$	$27.12 \cdot 10^{-8}$	$5.42 \cdot 10^{-7}$
10^{-5}	$5.42 \cdot 10^{-7}$	$5.42 \cdot 10^{-6}$	$5.42 \cdot 10^{-5}$	$10.85 \cdot 10^{-5}$	$27.12 \cdot 10^{-5}$	$5.42 \cdot 10^{-4}$
10^{-4}	$5.42 \cdot 10^{-4}$	$5.42 \cdot 10^{-3}$	$5.42 \cdot 10^{-2}$	$10.85 \cdot 10^{-2}$	$27.12 \cdot 10^{-2}$	$5.42 \cdot 10^{-1}$

For $R_a < 10^{-6}$, the viscosity effects prevent buoyancy circulation. It can be seen that for device characteristic dimension $L_C = 1\mu m$ there is no acceleration sensing based on buoyancy effects, for the g_{level} range considered. For L_C in the order of $10\mu m$ and $(\Delta T) \geq 100K$, a minimum acceleration of $1g$ will generate buoyancy effects. This will roughly correspond to an induced velocity of $5\mu m/(ms)$. These considerations neglect the fluid properties (k, μ, c_p) dependence on temperature. In Table3 only Rayleigh values 10^{-6}<Ra<100 are marked.

Table 3: $R_a < 10^{-6}$ values ruled out. $10^{-6} < R_a < 100$ marked.

$L\,[m]$	$\Delta T = 1K$	$10K$	$100K$	$200K$	$500K$	$1000K$
	$g_{level} = 10^{-3}$					
10^{-4}	/	/	$5.42 \cdot 10^{-6}$	$10.85 \cdot 10^{-6}$	$27.12 \cdot 10^{-6}$	$5.42 \cdot 10^{-5}$
	$g_{level} = 10^{-2}$					
10^{-4}	/	$5.42 \cdot 10^{-6}$	$5.42 \cdot 10^{-5}$	$10.85 \cdot 10^{-5}$	$27.12 \cdot 10^{-5}$	$5.42 \cdot 10^{-4}$
	$g_{level} = 10^{-1}$					
10^{-5}	/	/	/	/	/	$5.42 \cdot 10^{-6}$
10^{-4}	$5.42 \cdot 10^{-6}$	$5.42 \cdot 10^{-5}$	$5.42 \cdot 10^{-4}$	$10.85 \cdot 10^{-4}$	$27.12 \cdot 10^{-4}$	$5.42 \cdot 10^{-3}$
	$g_{level} = 1$					
10^{-5}	/	/	$5.42 \cdot 10^{-6}$	$10.85 \cdot 10^{-6}$	$27.12 \cdot 10^{-6}$	$5.42 \cdot 10^{-5}$
10^{-4}	$5.42 \cdot 10^{-5}$	$5.42 \cdot 10^{-4}$	$5.42 \cdot 10^{-3}$	$10.85 \cdot 10^{-3}$	$27.12 \cdot 10^{-3}$	$5.42 \cdot 10^{-2}$
	$g_{level} = 5$					
10^{-5}	/	/	$27.12 \cdot 10^{-6}$	$5.42 \cdot 10^{-5}$	$135.63 \cdot 10^{-6}$	$27.12 \cdot 10^{-5}$
10^{-4}	$27.12 \cdot 10^{-5}$	$27.12 \cdot 10^{-4}$	$27.12 \cdot 10^{-3}$	$5.42 \cdot 10^{-2}$	$135.63 \cdot 10^{-3}$	$27.12 \cdot 10^{-2}$
	$g_{level} = 10$					
10^{-5}	/	$5.42 \cdot 10^{-6}$	$5.42 \cdot 10^{-5}$	$10.85 \cdot 10^{-5}$	$27.12 \cdot 10^{-5}$	$5.42 \cdot 10^{-4}$
10^{-4}	$5.42 \cdot 10^{-4}$	$5.42 \cdot 10^{-3}$	$5.42 \cdot 10^{-2}$	$10.85 \cdot 10^{-2}$	$27.12 \cdot 10^{-2}$	$5.42 \cdot 10^{-1}$

The fluid parameter values should be evaluated at a reference temperature, T_r given by:

$$T_r = T_\infty - 0.38\,[T - T_\infty] \tag{16}$$

This relationship can be approximated by:

$$T_r = \frac{T_\infty + T}{2} \tag{17}$$

with an error $\varepsilon \leq 2.5/100$ in corresponding heat transfer parameters. The above results apply to laminar flows only.

It has been shown that for horizontal, isothermal, cylindrical wires in air the following heat transfer modes are established versus Rayleigh number values [8]:

$R_a < 100$ The heat is transferred by conduction only. Temperature distribution is not affected by the buoyancy flow. Any further decrease in characteristic dimension will result in an increased convective heat transfer coefficient. The flow is symmetrical about the horizontal axis.

$10^2 < R_a < 3 \cdot 10^4$ The transition regime between conduction and boundary layer. The isotherms are ellipsis with heat still transferred essentially by conduction.

$3 \cdot 10^4 < R_a < 10^5$ Steady laminar boundary layer regime.

Hence, for devices in air with $L_C \leq 100\mu m$ and ΔT in the range of hundreds of degrees, the heat transfer takes predominantly place by conduction. The radiation effects were not considered in this analysis.

Based on previous R_a values, the Nusselt number can be now estimated. All fluid properties will be evaluated at: $T_r = \dfrac{T_{body} + T_{amb}}{2}$

The Nusselt values calculated with the equation (from eq.13):

$$N_u = [0.6 + 0.320877 \cdot R_a^{1/6}]^2 \qquad (18)$$

are listed in Tables 4 and 5 for $L_c = 10^{-5}$ m and $L_c = 10^{-4}$ m, respectively.

It can be seen that for the same g_{level} and ΔT, the convective heat transfer coefficient, h, increases as characteristic dimension decreases. For the same L_C and ΔT, h increases as g_{level} increases. The amount of heat Q transferred per unit length by convection is $Q = P\bar{h}(\Delta T)$, where P is the wetted perimeter.

Table 4: Nusselt, h numbers values for horizontal bodies in air with characteristic dimension $L_C = 10^{-5} m$ and $(\Delta T) \leq 1000K$. Here h is the convective heat transfer coefficient $[h] = W/(m^2 \cdot K)$

$\Delta T = 1K$	$10K$	$100K$	$200K$	$500K$	$1000K$
$g_{level} = 10^{-2}$					
0.37217	0.37754	0.384069	0.385006	0.384303	0.381388
972.84	986.88	1140.68	1272.44	1637.13	2170.09
$g_{level} = 10^{-1}$					
0.37792	0.385876	0.3956	0.3970	0.39595	0.39161
987.9	1008.68	1174.95	1312.08	1486.77	2228.3
$g_{level} = 1$					
0.38645	0.3983	0.41284	0.414938	0.413366	0.40686
1010.18	1041.15	1226.14	1371.37	1760.93	2315.05
$g_{level} = 5$					
0.39479	0.41047	0.42982	0.43262	0.43052	0.42185
1031.98	1072.98	1276.58	1429.82	1834.04	2400.36
$g_{level} = 10$					
0.39916	0.41688	0.4388	0.441977	0.43959	0.42976
1043.4	1089.74	1303.23	1460.73	1872.67	2445.38

Table 5: Nusselt, h numbers values for horizontal bodies in air with characteristic dimension $L_C = 10^{-4}m$ and $(\Delta T) \leq 1000K$.Here the convective heat transfer coefficient h = W / (m^2 K)

$\Delta T = 1K$	$10K$	$100K$	$200K$	$500K$	$1000K$
$g_{level} = 10^{-2}$					
0.39916	0.416886	0.4388	0.441977	0.43959	0.42977
104.34	108.974	130.323	146.073	187.267	244.538
$g_{level} = 10^{-1}$					
0.418174	0.444929	0.478342	0.483211	0.479558	0.464527
109.3	116.3	142.07	159.7	204.3	264.31
$g_{level} = 1$					
0.446883	0.487744	0.539467	0.54706	0.541362	0.517993
116.81	127.5	160.22	180.8	308.034	294.74
$g_{level} = 5$					
0.4755	0.530941	0.601865	0.6123615	0.604482	0.57228
124.3	138.8	198.91	222.5	257.51	325.63
$g_{level} = 10$					
0.490748	0.55415	0.6357326	0.647847	0.638552	0.60165
128.28	144.85	188.81	214.11	272.02	342.34

Since [8,11]:

$$\frac{\delta_t}{L_C} \sim \frac{1}{\sqrt[4]{R_a}}$$

for $R_a \in [10^{-6} - 10^{-2}]$, we have:

R_a	10^{-1}	10^{-2}	10^{-3}	10^{-4}	10^{-5}	10^{-6}
δ_t / L_C	1.78	3.16	5.62	10	17.78	31.62

Thus, the thermal boundary layer thickness is larger than the characteristic dimension for the ranges of L_C, g_{level} and ΔT considered here.

It has been shown also that $\delta_t > \rho$. This means that the boundary layer assumptions usually used in deriving the temperature distributions and heat transfer are no longer valid. The region around the heat source should be divided in far region and near region and for each of them the starting equations have to be energy conservation and continuity equations. For horizontal cylinders it has been shown [8] that the main effects in natural convection are the angular temperature dependence and heat transfer mainly by conduction in the near field. In this case the effect of increasing temperature is an increase in heat transfer, temperature distribution remaining about the same. My device simulations show no temperature distribution change over 1000 degree range, but an important increase in heat transfer (Fig.13).

2.1.3. Combined Conduction/Convection Mode of Heat Transfer.

At the contact area between bodies and their gaseous surroundings there will always be a convective heat transfer. Thus, usually the heat is conducted inside the solid bodies and convected at their surfaces. The relative importance of the two heat transfer modes is given by the Biot number, Bi [7-11]:

$$Bi = \frac{\bar{h} L_C}{k} \tag{19}$$

Its significance is:

$$Bi = \frac{\text{conductive resistance in the solid}}{\text{convective resistance in the fluid}}$$

The physical limits on the Biot number are:

$Bi \to 0$ when $R_{conductive} \to 0$ or $k \to \infty$

and

$Bi \rightarrow \infty$ when $R_{convective} \rightarrow 0$ or $\bar{h} \rightarrow \infty$

For practical purposes, if $Bi < 0.1$ then the solid is considered isothermal. The transverse variation of the temperature inside the body, at any axial point, is much less than $T_{surface} - T_{amb}$. The temperature variations take place mostly in the fluid. For $Bi > 1$, the fluid is nearly isothermal and the temperature differences occur predominantly in the solid.

The Biot number values for $g_{level} \in [0.001 - 10]\, g$, $\Delta T \leq 1000K$, $L \in [10^{-5} - 10^{-4}]\, m$ are < 1.5 x 10^{-3} for silicon and most of the metals used in sensor or IC fabrication. For Si even at 1000° C, the Bi is 1.22 x 10^{-3} and for metals < 0.5 x 10^{-3}, so the sensor will be always isothermal.

Thus for $L < 10^{-3} m$ and $\Delta T \leq 1000K$, the bodies can be considered isothermal when Si, Al, Au, Cr, Ni, Pt, Ti, Ta, W or Mo are the body materials. For a given solid body surface temperature and a fluid at the ambient temperature, the temperature differences will occur predominantly in the fluid.

2.1.4. Conclusions

Considering all the above results, it can be concluded that:

I. for $L \sim 10^{-6} m$, $g_l \in [0.001 - 10]\, g$, $\Delta T \leq 1000K$ there are no buoyancy effects.

The heat is transferred by conduction only. $R_a \leq 10^{-6}$.

II. for $L \in [10^{-5} - 10^{-4}]\, m$, $g_{level} \in [0.001 - 10]\, g$, $\Delta T \leq 1000K$, the heat is transferred mainly by conduction; the buoyancy effects generate a symmetrical flow about the axis.

$R_a \ll 1$.

III. the thermal boundary layer is thicker than the velocity layer, the two being locked together.

IV. the thermal boundary layer is thicker than the device characteristic dimension.

Thus the boundary layer solutions for heat transport, the ones usually available, may not be sufficiently accurate. The region around the body might be divided into far and near regions, with conduction being the main heat transfer mechanism in the near region. In the far region, the heat transfer takes place mainly by convection.

V. the Rayleigh number values are greater than 10^{-5} for

$L\,[m]$	$\Delta T\,[K]$	g_{level}
10^{-5}	$\Delta T \geq 100$	$g_l \geq 1g$
10^{-4}	$\Delta T \geq 100$	$g_l \geq 0.001g$

VI. for Si, Al, Au, Ni, Cr, Pt, Ti, Ta, W or Mo as constituent materials, the horizontal solid bodies suspended in air, with $L_C < 10^{-3}m$ and $T_{surface} - T_{amb} \leq 1000K$, can be considered isothermal if $g_{level} \in [0.001 - 10]\,g$.

It has been shown that for $L_c <= 10^{-4}$ m the Rayleigh number is Ra < 100, thus the boundary layer assumption is no longer valid and the near and far fields should be considered.

For horizontal cylinders in an unsteady natural convection, Ra < 100, during initial transition period, curvature effects lead to an increase in skin friction as well as heat transfer rate.

2.2 Mathematical Model

The device's schematic representation is given in Fig.6. The resistors dimensions are length, L, width, w, and thickness, t. The bridges' separation is s and the cavity's depth is d. The suspended structures are surrounded by air at atmospheric pressure. The packaged chip is sealed in a $5cm \times 4cm \times 1cm$ plastic box. Electric power, P_e, is supplied to the central bridge, the heater.

The volumetric power density, $q\,[W/m^3]$, is $q = P_e/V$ where V is the suspended bridge resistor's volume. All bridges are structurally identical in the processing limits. The remaining symmetrically placed bridges, besides the heater, are the sensing elements. A very low current is passed

through the sensing elements in order to measure their electrical resistance. Thus, the Joule effect can be neglected for the sensing elements, while it will warm up the heater in respect with the ambient medium.

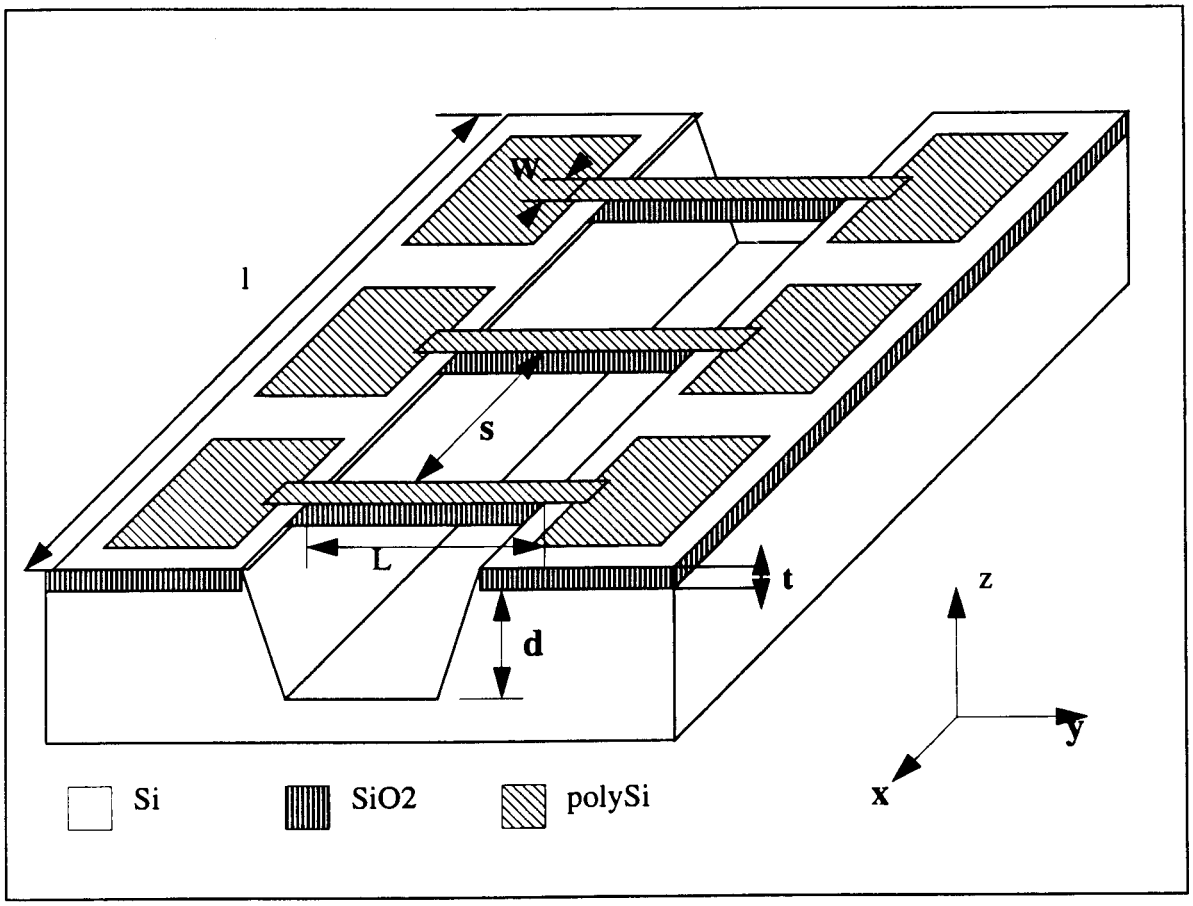

Fig.4 Schematic representation of the device.

The current density, J, through the heater creates a steady-state temperature distribution with the earth gravity as the only applied acceleration. The temperature distribution in the instrument

before an external acceleration is imposed is the steady-state distribution. The temperature distribution during an applied acceleration is the disturbed distribution. The surrounding air provides thermal coupling between the heater and the sensing elements.

In the steady-state, whether or not the detectors act as heat sinks depends on the conduction between the sensor and the Si substrate, the walls of the enclosure. If the resistance of the conduc tion path from the sensors to the walls (substrate) is much higher than the resistance of the gaseous boundary layer surrounding the sensors, i.e. $Bi_l \leq 1$, the sensor will reach a steady-state temperature close to that of the surroundings, irrespective of its thermal mass. Given no disturbance or air flow, a differential measurement of a symmetrical pair of detector resistances will yield zero output voltage.

Under an external applied acceleration, the steady-state temperature distribution symmetry will be distorted. The resulted asymmetry will create a temperature difference between two symmetrically placed detectors. Due to temperature coefficient of the resistance, this temperature difference will create an imbalance between the two sensor resistances, which in turn will give an output voltage proportional to that temperature difference.

Thus the two functional blocks we have are the heater and the sensing elements. The heater will be represented as an electric suspended wire with radius $r_h = (w \cdot t) / (2(w+t))$, length L, internal heat generation q, having both ends clamped at walls kept at room temperature. The sensing elements are represented as electric suspended wires without internal heat generation.

Hence, the encountered heat transfer problems are:

- *steady-state*

i)temperature distribution around an electric heated wire with constant surface temperature and its ends clamped at walls kept at room temperature.

ii)steady-state temperature at the detector.

-transient

iii)warm-up time of the device.

iv)the sensor's speed of response to a change in the air temperature at its surface.

To solve these problems, the following assumptions are made:

1. the surrounding fluid is an ideal gas, thus its coefficient of thermal expansion is

$$\beta = \frac{1}{v} \cdot \left(\frac{dv}{dT}\right)_p = \frac{1}{T_\infty}, \quad pv = RT$$

2. the heater temperature is constant for a given electric power.
3. the temperature along the heater is uniform.
4. the temperature along the detectors is uniform.
5. conduction along the sensing elements is not important so that the ambient temperature is detected.
6. heat losses due to radiation are negligible.
7. all solid bodies are isotropic.
8. convective heat transfer coefficient is assumed constant all along the convective surface.
9. the region outside the cavity is regarded as a free space region; the region inside the cavity is a "at rest" space, i.e. there is no significant movement.
10. heater thermal conductivity nearly independent of temperature; its electrical resistivity increases almost linearly with temperature
11. the actual geometry of the wire, a parallelepiped, is assumed to be a cylinder of radius L_c.

Based on heat transfer parameters h, k, ΔT, $L_C = r_h, r_s$ and q, the conditions for which the above assumptions take place are estimated.

2.2.1 Heater

The heater may be treated as a long fin with internal heat generation. Its schematic representation is given in Fig.5. The heater total length is $2L$.

Inside the heater, the heat is transferred by conduction and, at its surface, is released to the surrounding air by convection. The heater's surface temperature is assumed to be constant in time. The energy balance equation for the heat transfer is:

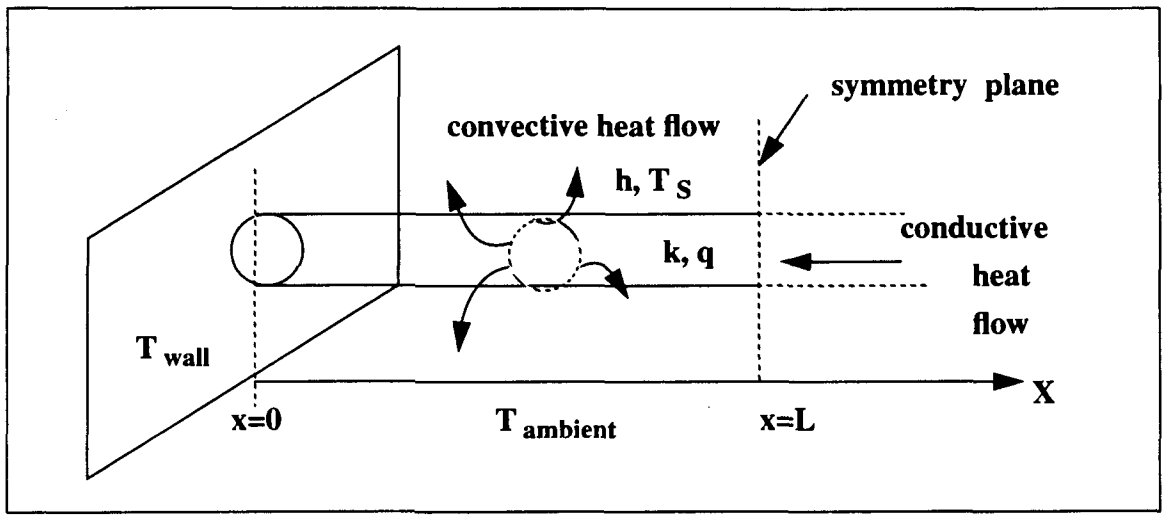

Fig.5 Heater as a long fin with internal heat generation

$$\frac{d}{dx}(kA \cdot \frac{dT}{dx}) - hP(T - T_{\infty}) + qA = c_p \cdot \rho \cdot A(\frac{dT}{dt}) \qquad (20)$$

Since we ask for constant heater temperature, the term on the right side of the equation is set to zero. The heater is in steady-state. The temperature varies with x only. The walls are at ambient temperature. The problem's boundary conditions are:

$$T(x) = T_0 \quad \text{at} \quad x = 0 \tag{21a}$$

and

$$T(x) \to T_\infty \quad \text{as} \quad x \to L \tag{21b}$$

By defining the following parameters:

$$m = \sqrt{\frac{hP}{kA}} \quad ; \quad \Theta(x) = \frac{T(x) - T_\infty}{T_0 - T_\infty} \quad ; \Theta_0 = T_0 - T_\infty$$

eq.(20) can be written as:

$$\frac{d^2\Theta}{dx^2} - (m^2 \cdot \Theta) + \frac{q}{k} = 0 \tag{22}$$

The corresponding boundary conditions are:

$$\Theta = \Theta_0 \text{ at} \quad x = 0 \tag{22a}$$

$$\Theta \to 0 \text{ as} \quad x \to L \tag{22b}$$

The solution of this problem is:

$$\Theta(x) = \Theta_{omogen} + \Theta_{particular}$$

$$\Theta(x) = \Theta_o exp(-mx) + \frac{q}{m^2 k}[1 - exp(-mx)] \tag{23}$$

For $x = \frac{1}{m}$:

$$\Theta\left(\frac{1}{m}\right) = \frac{\Theta_0}{e} + \frac{q}{m^2 \cdot k} \cdot \left[1 - \frac{1}{e}\right] = \frac{\Theta_0}{e} + const$$

thus the interaction by longitudinal conduction with $x = 0$ support is sensed over the long-fin length scale $1/m$. Fig.6 shows the qualitative fin's temperature dependence on distance from the fin support.

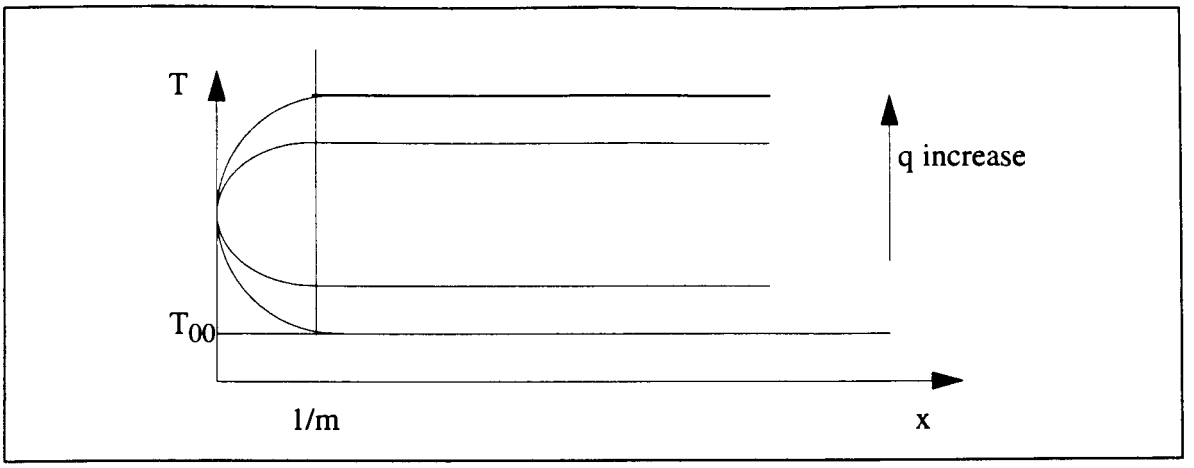

Fig.6 Fin temperature vs. distance from its support. Qualitative representation

The $(mL)^2$ parameter gives a hybrid Bi number. It represents the ratio between internal resistance to heat conduction along the structure and gross external resistance to convective heat removal:

$$(mL)^2 = \frac{hP}{kA} \cdot L^2 = \frac{L/(kA)}{1/(hPL)} = \frac{\text{internal 'resistance 'to 'conduction}}{\text{external 'resistance 'to 'convection}} \qquad (24)$$

The 1/m parameter 's values for different h values are given in Table 6. Here:

$$P/A = \frac{2(W+L)}{WL} = \frac{2}{w} \quad , \quad P/A = \frac{2\pi R}{\pi R^2} = \frac{2}{r_h}$$

It can be seen from Table 6 that the heater length scale, x_m= 1/m, over which longitudinal conduction with x = 0 support is sensed is:

$L_C[\mu m]$	1	10	100
$x_m[\mu m]$	<125	<1200	~10000

for g_{level} = 1.0;10.0 and $\Delta T < 1000K$

and is:

$L_C\,[\mu m]$	~1	10	100
$x_m\,[\mu m]$	—	<1240	<12000

for $g_{level} = 0.001$ and $\Delta T < 1000K$.

Thus, for a given temperature range and device's characteristic dimension, the temperature profile along the heater is almost the same regardless the applied acceleration to the system. The estimated heater's temperature profile for heater length $L \gg 2x_m$ is given in Fig.7.

Table 6: $\frac{1}{m}$ parameter's values vs. h at different P/A ratios. $\Delta T = T_{fin} - T_\infty$.

	$\Delta T = 10K$	$100K$	$200K$	$500K$	$1000K$	L_C $[m]$	g_{lev}
h/k $[m^{-1}]$	62.13	116.68	174.09	487.91	1273.17	10^{-6}	1
m $[m^{-1}]$	$0.8 \cdot 10^4$	$1.12 \cdot 10^4$	$1.32 \cdot 10^4$	$2.21 \cdot 10^4$	$3.54 \cdot 10^4$		
1/m $[m]$	$1.25 \cdot 10^{-4}$	$0.9 \cdot 10^{-4}$	$0.76 \cdot 10^{-4}$	$0.45 \cdot 10^{-4}$	$0.28 \cdot 10^{-4}$		
h/k	6.94	12.38	17.05	41.72	100.6	10^{-5}	
m	$0.833 \cdot 10^3$	$1.11 \cdot 10^3$	$1.3 \cdot 10^3$	$2.04 \cdot 10^3$	$3.17 \cdot 10^3$		
1/m	$1.2 \cdot 10^{-3}$	$0.9 \cdot 10^{-3}$	$0.77 \cdot 10^{-3}$	$0.5 \cdot 10^{-3}$	$0.31 \cdot 10^{-3}$		
h/k	0.85	1.62	2.25	7.3	12.81	10^{-4}	
m	$0.9 \cdot 10^{-2}$	$1.27 \cdot 10^{-2}$	$1.5 \cdot 10^{-2}$	$2.7 \cdot 10^{-2}$	$3.58 \cdot 10^{-2}$		

Table 6: $\frac{1}{m}$ parameter's values vs. h at different P/A ratios. $\Delta T = T_{fin} - T_{\infty}$.

	$\Delta T = 10K$	$100K$	$200K$	$500K$	$1000K$	L_C $[m]$	g_{lev}
1/m	$1.08 \cdot 10^{-2}$	$0.78 \cdot 10^{-2}$	$0.66 \cdot 10^{-2}$	$0.37 \cdot 10^{-2}$	$0.28 \cdot 10^{-2}$		
h/k	62.96	143.3	178.3	501.6	1345.7	10^{-6}	10
m	$7.93 \cdot 10^{3}$	$11.97 \cdot 10^{3}$	$13.35 \cdot 10^{3}$	$22.4 \cdot 10^{3}$	$36.7 \cdot 10^{3}$		
1/m	$0.126 \cdot 10^{-3}$	$0.083 \cdot 10^{-3}$	$0.075 \cdot 10^{-3}$	$0.044 \cdot 10^{-3}$	$0.027 \cdot 10^{-3}$		
h/k	7.26	13.18	18.17	44.38	106.3	10^{-5}	
m	$0.85 \cdot 10^{3}$	$1.15 \cdot 10^{3}$	$1.35 \cdot 10^{3}$	$2.1 \cdot 10^{3}$	$3.26 \cdot 10^{3}$		
1/m	$1.17 \cdot 10^{-3}$	$0.871 \cdot 10^{-3}$	$0.74 \cdot 10^{-3}$	$0.475 \cdot 10^{-3}$	$0.3 \cdot 10^{-3}$		
h/k	0.96	1.91	2.66	6.44	14.88	10^{-4}	
m	$0.98 \cdot 10^{2}$	$1.38 \cdot 10^{2}$	$1.63 \cdot 10^{2}$	$2.54 \cdot 10^{2}$	$3.86 \cdot 10^{2}$		
1/m	$1.02 \cdot 10^{-2}$	$0.72 \cdot 10^{-2}$	$0.61 \cdot 10^{-2}$	$0.4 \cdot 10^{-2}$	$0.26 \cdot 10^{-2}$		
h/k	6.48	11.3	15.49	38.0	92.65	10^{-5}	10^{-3}
m	$0.8 \cdot 10^{3}$	$1.06 \cdot 10^{3}$	$1.24 \cdot 10^{3}$	$1.95 \cdot 10^{3}$	$3.04 \cdot 10^{3}$		
1/m	$1.24 \cdot 10^{-3}$	$0.94 \cdot 10^{-3}$	$0.8 \cdot 10^{-3}$	$0.51 \cdot 10^{-3}$	$0.33 \cdot 10^{-3}$		
h/k	0.69	1.24	1.7	4.17	10.06	10^{-4}	
m	$0.8 \cdot 10^{2}$	$1.11 \cdot 10^{2}$	$1.3 \cdot 10^{2}$	$2.04 \cdot 10^{2}$	$3.17 \cdot 10^{2}$		
1/m	$1.2 \cdot 10^{-2}$	$0.9 \cdot 10^{-2}$	$0.76 \cdot 10^{-2}$	$0.49 \cdot 10^{-2}$	$0.31 \cdot 10^{-2}$		

For $L \gg 2x_m$, the temperature along the heater is constant and proportional to heater's volumetric heat generation rate.

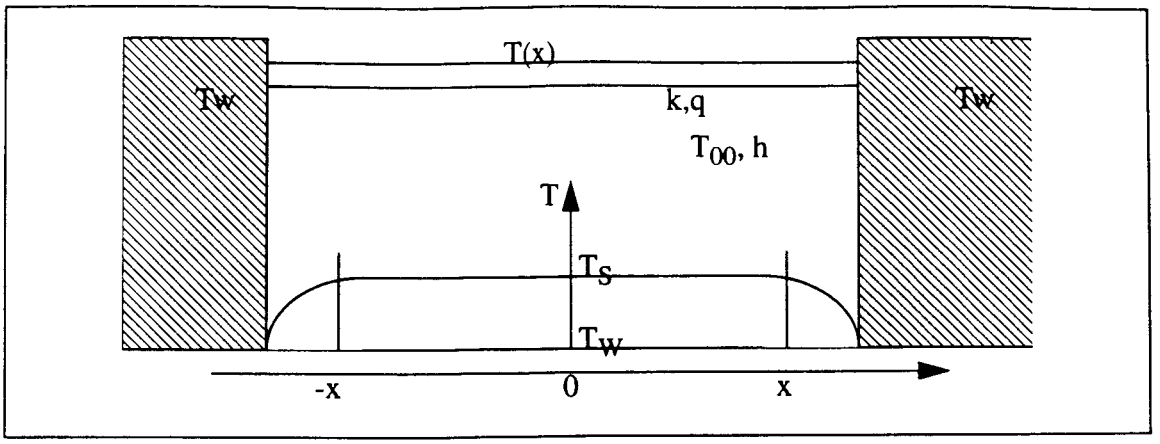

Fig.7 Estimated heater temperature profile for $L \gg 2x_m$.

Beyond $x = 1/m$ length away from the substrate (wall), the heater temperature becomes fairly independent of x, namely:

$$\Theta \approx q/(m^2 k) \qquad , \qquad [q] = W/m^3 \tag{25}$$

Since we have asked for heater temperature to be constant in time, it is assumed that the internal generated heat, $q = (UI)/V$, is released by convection, $q = \bar{h}\Delta T$. Thus $\bar{h} = q/(\Delta T)$.

If $\overline{\Delta T}$ is the average temperature over the length of the heater, then:

$$\frac{\overline{\Delta T}}{const} = \int_0^1 (\frac{x}{L})^{1/5} d(\frac{x}{L}) = \frac{5}{6}$$

Hence, $\overline{\Delta T}$ is within 1/6 of ΔT at the middle of the heater. Thus I can consider $\overline{\Delta T}$ as being the difference between the midpoint value of heater temperature and the surroundings' temperature.

The total heat transfer rate through the root of the heater is:

$$q_b = -kA \cdot (\frac{dQ}{dx})_{x=0} \qquad \text{(Fourier's Law)} \tag{26}$$

The heat flow will be from heater to the substrate if $q_b < 0$, i.e.:

$$\frac{qA}{hPQ_b} > 1 \qquad (27)$$

For $g_{level} = 1.0$, $\Delta T = 300K$, $L_C = 10^{-5}$ and $q = 1.5 \cdot 10^{12}\,(W/m^3)$, $P = 42mW$:

$$\frac{qA}{hPQ_b} = 1.66 > 1$$

Thus a heat flow from heater to the substrate exist.

From the above analysis it can be concluded that for a heater length $L_{eff} = L - 2x_m$:

I. the heater temperature can be taken as that at the middle of it within $(1/6)\Delta T$ error

II. the heater temperature is independent of the position along its axis, all along L_{eff}

III. x_m is in the order of $125\mu m$ for $L_C = 1\mu m$, $1200\mu m$ for $L_C = 10\mu m$ and $10mm$ for $L_C = 100\mu m$ with $g_{level} \leq 10g$, $\Delta T \leq 1000K$.

IV a heat flow from heater to the substrate exist. The support's temperature is (from eq.27):

$$\Theta_{wall} \sim \frac{\Theta_{middle}}{const} \quad \text{, where} \quad const = \frac{qA}{hP} = \frac{qr_h}{2h}$$

2.2.2. Sensing Elements

The sensing elements are regarded as suspended electric wires with no heat generation. The ends of the wire are clamped at two widely separated walls (substrate). The walls are at room temperature, T_w. The wires are in steady-state, at a constant temperature, T, $T > T_w$. The heat transfer takes place by conduction along the wire's axis and by convection at wire's surface. At equilibrium, the wires exchange heat with surroundings by convection. The length of the wires is heated by a heat transfer coefficient, h. The sensing elements may be treated as long fins without internal heat generation.

The length of the sensing elements is $2L$, their cross-section area is A, circumferential perimeter P and thermal conductivity k. The fin length is L. The sensor's schematic representation is given in Fig.8. The characteristic dimension of the fin in the transverse direction is A/P.

A $Bi_{\perp}$ number for the conduction in the transverse direction is defined as:

$$Bi_{\perp} = \frac{\bar{h}(A/P)}{k} \tag{28}$$

If $Bi \ll 1$ then the transverse variation of the temperature at any axial point is negligible. Thus $T = T(x)$ only and the heat flow can be considered one-dimensional. This condition is met for the parameters' range specified in this analysis ($L_C \leq 100\mu m$, $\Delta T \leq 1000K$, $g \leq 10$).

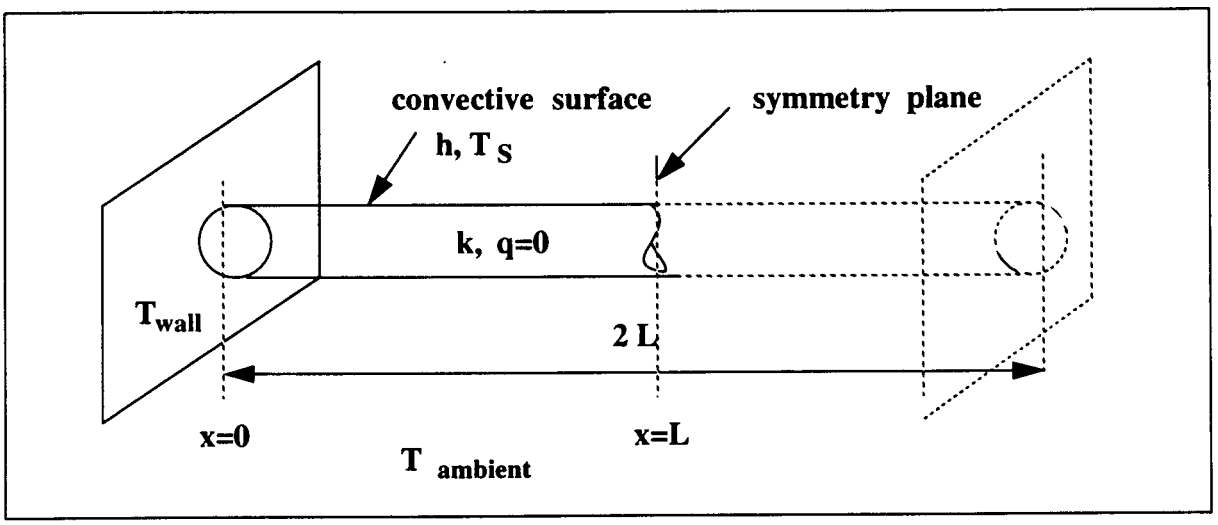

Fig.8 Representation of sensing elements as long fins without internal heat generation

The energy balance equation for the fin represented in Fig.8 is:

$$kA\left(\frac{dT}{dx}\right)_{x+dx} - kA\left(\frac{dT}{dx}\right)_{x} + \bar{h}(P\delta x)\cdot(T_{\infty} - T)_{x} = 0 \tag{29}$$

Since:

$$\frac{\left(\frac{dT}{dx}\right)_{x+dx} - \left(\frac{dT}{dx}\right)_{x}}{dx} \rightarrow \frac{d^2T}{dx^2}$$

which can be written:

$$\frac{1}{T_\infty - T_w} \cdot \frac{d^2T}{dx^2} = ,\frac{d^2}{dx^2}\left[\frac{T_\infty - T}{T_\infty - T_w}\right]$$

the following equation results from eqn.29:

$$\frac{d^2}{dx^2}\left[\frac{T_\infty - T}{T_\infty - T_w}\right] = \frac{hP\,(T_\infty - T)}{kA\,(T_\infty - T_w)} \qquad (29a)$$

The boundary conditions for this problem are:

i) $T_\infty - T = T_\infty - T_w$ at $x = 0$ i.e. the temperature at the fin's base is the wall temperature

ii) $\frac{d}{dx}(T_\infty - T) = 0$ at $x = L$ i.e. the fin's tip is insulated as it represents a symmetry point.

By multiplying eq.(29a) with L^2, I get:

$$\frac{1}{\left(\frac{1}{L^2}\right)}\frac{d^2}{dx^2}(T_\infty - T) = \frac{hPL^2}{kA}\frac{(T_\infty - T)}{(T_\infty - T_w)}$$

and identifying parameters:

$$\zeta = \frac{x}{L} \quad ; \quad \Theta = \frac{T_\infty - T}{T_\infty - T_w} \quad ; \quad (mL)^2 = \frac{hPL^2}{kA}$$

results

$$\frac{d^2\Theta}{d\zeta^2} = (mL)^2 \cdot \Theta \qquad (30)$$

Using the dimensionless parameters, the boundary conditions are:

ii) $\dfrac{T_\infty - T}{T_\infty - T_w} = 1$ at $\dfrac{x}{L} = 0$ i.e. $\Theta = 1$ at $\zeta = 0$ (31*a*)

ii) $\dfrac{L}{T_\infty - T} \cdot \dfrac{d}{dx}(T_\infty - T) = 0$ at $\dfrac{x}{L} = 1$ i.e. $\dfrac{d\Theta}{d\zeta} = 0$ at $\zeta = 1$ (31*b*)

The general solution of eq.(30) is:

$$\Theta(x) = C_1 exp(mL\varsigma) + C_2 exp(-mL\varsigma) \tag{32}$$

The constants C_1, C_2 are determined using eqns.(31):

i) $C_1 + C_2 = 1$ (33*a*)

ii) $C_1 exp(mL) - C_2 exp(-mL) = 0$ (33*b*)

From eq.(33a) and eq.(33b):

$$C_1 exp(mL) - (1 - C_1) exp(-mL) = 0$$

$$C_1 [exp(mL) + exp(-mL)] - exp(-mL) = 0$$

$$C_1 (2\cosh mL) = exp(-mL)$$

Hence

$$C_1 = \frac{exp(-mL)}{2\cosh mL}, \quad C_2 = 1 - C_1 = 1 - \frac{exp(-mL)}{2\cosh mL}$$

Thus the solution is:

$$\Theta = \frac{\cosh mL\,(1 - \zeta)}{\cosh mL} \tag{34}$$

The dimensionless temperature at the tip is:

$$\Theta_{tip} = \frac{1}{\cosh mL} \quad , \ \zeta = 1 \ , \ \Theta = T_\infty - T \tag{35}$$

For $T_{tip} = T_\infty$

$$\Theta_{tip} = \frac{T_\infty - T_\infty}{T_\infty - T_w} = 0$$

So that from eq.(35):

$$\frac{1}{\cosh mL} \to 0 \tag{35a}$$

If $mL = 5$ then:

$$\Theta_{tip} = \frac{1}{\cosh 5} = 0.014$$

and

$$T_\infty - T_{tip} = 0.014\,(T_\infty - T_w)$$

Hence, the fin is $0.014\,(T_\infty - T_w)\,^oK$ below T_∞ at its end. Thus, if the fin is intended to function as a "thermometer" to read T_∞ , the reading will be in error of 1.4% for $mL = 5$. The sensing elements have to register the ambient temperature. Hence their minimum length, l, should be:

$$l = 2 \cdot \frac{5}{m} = \frac{10}{m} = 10x_m \quad \text{, where} \qquad m = \sqrt{(hP)/(kA)} \tag{36}$$

The results of this section can be summarized as follows:

1) the Biot number characteristic to the wires is <0.1, so that the wires approach an uniform temperature. The heat flow by conduction through the wire may have no resistance so that the entire length of the wire would become isothermal

2) the wire's interaction by longitudinal conduction to the walls is sensed over the length scale

$x_m = 1/m, \quad m = \sqrt{(hP)/(kA)}$

3) the wire's temperature is uniform over its effective length, $L_{eff} = L - 2x_m$

4) in order to read the ambient temperature within an error of 1.4%, the sensor's minimum length should be:

$$L = 10x_m \quad , \quad m = \sqrt{(hP)/(kA)} \quad , \quad x_m = 1/m$$

where: k=sensor thermal conductivity

A=sensor cross section area

h=convective heat transfer coefficient between the sensor and its surroundings

P=sensor wetted perimeter.

2.2.3 *Permissible Heater's Current Densities for Avoidance of Thermal Runaway Instability*

For a constant current source operated heater, there is no self-limiting mechanism for its temperature increase. This can result in heater's thermal runaway instability if its current density is greater than a certain value given by heater's material properties and size.

Let $q = (UI)/V$ be the heater volumetric heating rate. If ρ_e is its electrical resistivity, then:

$$q = \frac{UI}{V} = \frac{\rho_e \frac{L}{A} I^2}{AL} = \rho_e \cdot \left(\frac{I}{A}\right)^2 = \rho_e \cdot J^2 \qquad (37)$$

where

I= electric current U = voltage across heating resistance

L= heater's length V = heater's volume

J= current density.

Due to volumetric heating, there will be a change with the temperature of the local resistivity, ρ_e. If the resistor's thermal conductivity is nearly independent of temperature, then ρ_e changes almost linearly with T, i.e.

$$\rho_e \approx \rho_{e,0} + \dot{\rho}_e (T - T_0) \tag{38}$$

where

$T_0 = T(r_S)$ =heater temperature (assumed constant)

$$\rho_{e,0} = \rho_e (T_0) \tag{39a}$$

$$\dot{\rho}_e = \left(\frac{d\rho_e}{dT}\right)_{T=T_0}. \tag{39b}$$

For $\rho_e = \rho_e(T)$, $q = q(T)$, the heater's thermal conduction equation becomes:

$$\frac{1}{r} \cdot \frac{d}{dr}\left(r\frac{dT}{dr}\right) + C_1 T + C_2 = 0 \tag{40}$$

where C_1, C_2 = empirical constants of the electrical conductor:

$$C_1 = (J^2/k) \cdot \left(\frac{d\rho_e}{dT}\right)_{T=T_0} \tag{41a}$$

$$C_2 = \frac{\rho_{e,0}}{k} - \left(\frac{\dot{\rho}_e}{k} T_0\right) J^2 \tag{41b}$$

For known heater's surface temperature, T_0, the solution of eq.(39) is [38]:

$$T(0) - T_0 = \frac{2(C_2 + C_1 T_0)}{(8/r_S^2) - C_1} \tag{42}$$

where r_S=heater's radius

It is apparent that the following restriction applies to eq.(42) as a condition for thermal stability:

$$C_1 < (8/r_S^2) \tag{43}$$

By combining eqs.(43) and (41a), the following condition must be met if a steady-state tempera-

ture distribution, $T(r)$ is to exist for a constant current driven heater:

$$J < \frac{2^{3/2}}{r_S} \left(\frac{k}{\rho_e}\right)^{1/2} \tag{44}$$

If the exact solution of eq.(39), the Bessel functions had been used, the factor $2^{3/2} = 2.828$ would have been replaced by 2.405. In order to use eq.(44), a relationship for $\dot{\rho}_e$ is needed. From

$$R = \frac{L}{A}\rho_e \quad ; \quad R(T) = \frac{L}{A}\rho_e(T) \tag{45}$$

and

$$R(T) = R_0 + R_0 \cdot \alpha \cdot \Delta T \quad , \quad \alpha = \text{temp. coeff. of the resistor, TCR} \tag{46}$$

I get:

$$\left[\rho_e(T)\frac{L}{A}\right]\frac{A}{L} = \left[\rho_{e,0}\frac{L}{A}\right]\frac{A}{L} + \left[\rho_{e,0}\frac{L}{A}\right]\left(\frac{A}{L} \cdot \alpha \cdot \Delta T\right) \tag{47}$$

$$\rho_e(T) = \rho_{e,0} + \rho_{e,0}(\alpha \cdot \Delta T) \tag{48}$$

Hence, from eqs.(48) and (38):

$$\dot{\rho}_e = \rho_{e,0} \cdot \alpha \tag{49}$$

and

$$J < \frac{2^{3/2}}{r_h} \left(\frac{k}{\rho_{e,0} \cdot \alpha}\right)^{1/2} \tag{50}$$

For convective wire surface eq.(50) is corrected to [38]:

$$J < \frac{2^{3/2}}{r_h} \left(\frac{k}{\rho_{e,0} \cdot \alpha}\right)^{1/2} \left(\frac{Bi}{Bi+4}\right)^{1/2} \tag{51}$$

where $Bi = \frac{hr_h}{k}$ is the Biot number.

According to eq.(51), the maximum current density of a heater is $J \leq 602\,(\mu A)/\mu m^2$ for $r_h = 1\mu m$. The condition given by eq.(51) is very restrictive. For the same conditions, the maximum current densities as given by eq.(50) are:

Permissible heater current densities for $r_h = 1\mu m$, $\alpha = 0.003\ ^oC^{-1}$, $\rho_{e,0} = 0.007\,(\Omega \cdot cm)$

$\Delta T\,[^oK]$	100	200	300	500
$J\,[(mA)/\mu^2]$	8.23	9.239	9.703	10.976

The table above gives the maximum admissible current densities for

$\alpha = 0.003^oC^{-1}$, $\Delta T = 100;200;300;500K$, $r_h = 1\mu m$ and $\rho_{e,0} = 0.007\,(\Omega \cdot cm)$.

The corresponding maximum power densities are:

$\Delta T\,[K]$	100	200	300	500
$q\,[W/m^3] \times 10^{12}$	1.925	2.2088	2.493	2.9191
$q\,[(mW)/(\mu m)^3]$	0.0019	0.0022	0.0024	0.0029

If the heater volume is $V = 14 \times 10^3 \mu m^3$, then the corresponding maximum electric power to the heater is 26.6mW, 30.8mw, 33.6mW and 40.6mW, respectively.

Considering all the above, it can be concluded that:

1) the maximum allowable current density through the heater decreases as the equivalent radius of the heater wire increases (eq.44)

2) at $r_h = 1\mu m$, the following current densities should be considered:

$J = 8.23;9.24;9.7;10.98$ $mA/\mu m^2$ for $\Delta T = 100;200;300;500^oK$, respectively.

3) by considering conduction/convection mode of heat transport at wire surface and its characteristic Biot number, the maximum allowable current densities are severely reduced to

$J = 517;546;572;602\mu A/\mu m^2$, for the same temperature differences. These values should be considered if an energy balance equation is used to determine the heater's temperature distribution.

2.3. Steady-State

A heat transfer problem is classified as a steady-state problem if the temperature distribution is not a function of time. The system is at equilibrium.

2.3.1. Heater

The temperature field generated by the heater can be separated into internal temperature field and external temperature field. The internal temperature field is the temperature distribution inside the heater. The external temperature field is the temperature distribution outside the heater, into the surrounding fluid. An expression for heater's surface temperature will allow us to evaluate heater temperature vs. its power supply. An expression for temperature distribution outside the heater will allow us to estimate air temperature at sensor's location. The results of the previous sections:

- $Bi < 0.1$
- $L_{eff} \geq L - 2x_m$
- $T(x)$ =constant over L_{eff}

- the substrate influence is not sensed at a distance range x_m away from it

let us to consider the heater as an isothermal infinitely long cylinder of radius $r = 4\frac{V}{A} = 2t_k$, with internal heat generation q and convective heat transfer coefficient h (Fig.9). Here:

T_S = constant surface temperature.

q = volumetric heat generation rate.

h = convective heat transport coefficient.

V = volume.

A = cross section area.

t_k = thickness.

r_S = heater equivalent radius, the cylinder characteristic dimension.

The conduction equation for radial temperature distribution inside the heater is [7-11]:

$$\frac{1}{r} \cdot \frac{d}{dr}(r\frac{dT}{dr}) + \frac{q}{k} = 0 \qquad (52)$$

with the boundary conditions

$$h\,[T_S - T_\infty] = -k\,(\frac{dT}{dr})_{r=r_S} \qquad \text{(convective surface)} \quad (53a)$$

$$(\frac{dT}{dr})_{r=0} = 0 \qquad \text{(axis = symmetry line)} \quad (53b)$$

The solution of this problem is [7-11]:

$$\frac{T(r) - T_\infty}{T_\infty} = \frac{q \cdot r_S}{h \cdot T_\infty}\left(1 + \frac{h \cdot r_S}{2k} - \frac{h \cdot r^2}{2r_S \cdot k}\right) \qquad (54)$$

Here it is assumed that air's thermal conductivity is constant, i.e. equal to $k_{average}$. The effect of

Bi number value was not considered, so that eq.(54) represents the general solution for a suspended electric wire.

The temperature inside the heater has a parabolic distribution (Fig.10). The temperature has a maximum at the heater's axis:

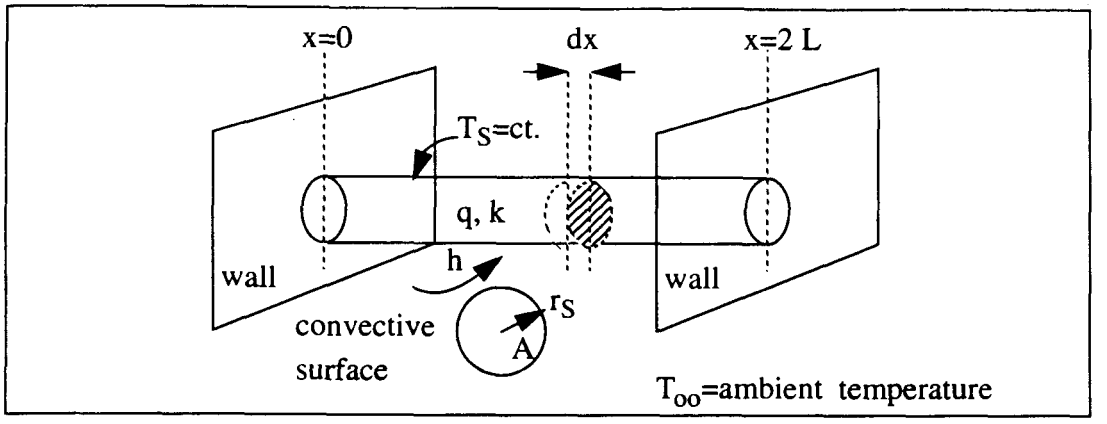

Fig.9- Heater as an isothermal infinite cylinder with internal heat generation

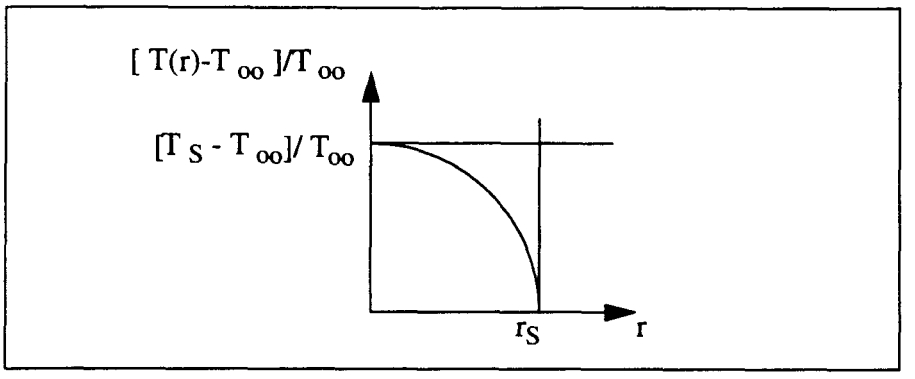

Fig.10- Temperature distribution inside the heater. $T(r) \sim \frac{1}{r^2}$

$$T(0) = T_{max} = T_{\infty} + \frac{q \cdot r_S}{2h}\left(1 + \frac{h \cdot r_S}{2k}\right) \qquad (55)$$

:The heater's surface temperature is:

$$T(r_S) = T_\infty + \frac{q \cdot r_S}{2h} \qquad (56)$$

Eq.(56) can be used to evaluate q for a prescribed heater's surface temperature. For a given r_S and prescribed T_S, h is calculated from:

$$h = Nu\frac{k}{r_S} \qquad (57)$$

The required volumetric heat generation rate is (from eq.(56)):

$$q = \frac{h(T_S - T_\infty)}{2r_S} \quad , \quad [q] = W/m^3 \qquad (58)$$

The heater's power densities at two different radii $r_S = 1\mu m; 10\mu m$ are listed in Table 7 for various ΔT . The convective heat transfer coefficients are taken from Table 4, which lists h values for given r_s, T_s.

Table 7: Volumetric heat generation

	$r_S\,[\mu m]$	$\Delta T = 100k$	$300k$	$500k$	$800k$	$1000k$
$10^{-3} \times q\,[mW/(\mu m)^3]$	1	1.1	2.43	4.06	7.95	21.2
	10	0.121	0.266	0.544	0.861	2.24

Temperature distribution outside the heater is that of an infinitely long hollow cylinder, where hollow inside the cylinder of radius r_S is the heater and the cylinder itself is made of air [5]. For a steady-state heater's surface temperature, the heat rate generated per unit length:

$$q_l(r_S) = \frac{i^2 \cdot R}{2\pi(r_S \cdot L)} = \frac{i^2}{2\pi r_S} R_l \qquad (59)$$

must be removed by convection at heater's surface. A prescribed heat flux is flowing through the inner surface. It can be assumed that the outer temperature is T_0, which is the ambient tempera-

ture, if the enclosure is far away from the heater. A schematic representation of this configuration is given in Fig. 11.

The boundary conditions for eq.(50) in this conduction problem are:

$$\text{(i)} \quad h\,[T(r_S) - T] = -k\left(\frac{dT}{dr}\right)_{r=r_S} \tag{60a}$$

$$\frac{i^2 \cdot R}{2\pi\,(r_S \cdot L)} = -k\left(\frac{dT}{dr}\right)_{r=r_S}$$

$$\text{(ii)} \quad T(r) = T_0 \text{ at } \quad r = r_0 \tag{60b}$$

The solution is [7,9-11]:

$$T(r) = C_1 \cdot ln\,(r) + C_2 \tag{61}$$

$$T(r) = T_0 + \frac{i^2}{2\pi k_{air}} R_l \cdot ln\left(\frac{r_0}{r}\right) \tag{62}$$

It is assumed that $k_{average}$ for air is constant with temperature and that the heater's electrical resistivity does not vary significant with temperature.

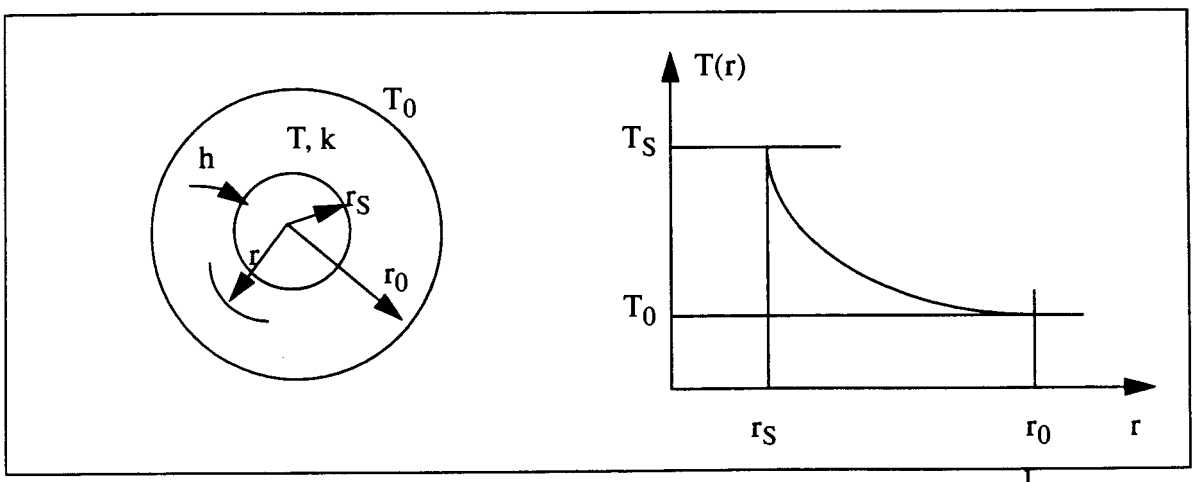

Fig.11 Temperature distribution outside the heater. $T(r) \sim ln\left(\frac{1}{r}\right)$

The temperature profile is logarithmic. The radial heat flux is:

$$q = -k\frac{d}{dr}T(r) = \frac{i^2}{2\pi r}R_l \qquad , \ [q] = W/m^3 \tag{63}$$

The radial heat flux falls off inversely with radius.The simulation results (Fig12) confirm this model behavior. The same heat flow, Q, must pass each radial surface. The radial heat flow through the cylinder is:

$$Q = -kA(r) \cdot \frac{dT}{dr} = -k(2\pi rL)\frac{dT}{dr} \tag{64}$$

and

$$Q = i^2 \cdot R \neq f(r) \qquad \text{(energy conservation)} \tag{65}$$

The radial heat flow through a hollow cylinder is the same at any radius, r, $r_S < r < r_0$, model behavior confirmed by numerical results (Fig.13). For a given electric power, the inner surface temperature, T_S, depends on cylinder's length, thermal conductivity and radii ratio, r_{outer}/r_{inner} . The heat flow across any cylindrical surface is constant for steady conditions.

The limitations of this analysis on the temperature distribution outside the heater are:

i) surrounding air considered an ideal fluid

ii) no convection. There is no fluid relative motion, i.e. buoyant heat transfer

iii) the air thermal conductivity is assumed constant and equal with its average value

iv) the enclosure is an infinitely conductive medium, far away, so that its temperature is $T_{amb} = const.$

The second assumption limits the analysis if the buoyant heat transfer takes place. The natural convection is negligible at (buoyant force ~ drag force):

- low gravity
- small heat source diameter / characteristic dimension

- high fluid viscosity

when the heated fluid is no longer buoyed away by convection. The conduction only will serve to remove the heat. This is the case for $Nu \rightarrow 0.36$ as $Ra \rightarrow 0$. Published experimental data for natural convection from horizontal, isothermal cylinders in air are given in Ref.7 p.260. For a heater with characteristic dimension $L_c = 1\mu m$ ($r_{eq} = 1\mu m$), the corresponding Nu values at various ΔT are listed in Table8 :

Table 8: Heater's Nusselt number values for $g_{level} = 1$

$L_c\,[\mu m]$	$\Delta T\,(k)$	100	200	300	500	1000
1.0		0.3763	0.3783	0.3796	0.3813	0.3843
2.0	Nu	0.3834	0.3864	0.3878	0.3904	0.3984
10.0		0.4128	0.4149	0.4149	0.4133	0.4068

Thus the heating element loses heat mainly by conduction for $dT_H < 300^o$ C. This is confirmed by the simulation results which show no buoyant effects for dT <= 300^o C (Figs.14). At $dT_H = 500^o$ K the mixed conduction / convection heat transfer takes place.

The temperature distribution outside the heater is logarithmic. The calculated (eq.59b) air temperature distribution is shown in Fig.15. The temperature gradient outside the heater is [cf. eq.(59b)]:

$$\frac{dT}{dr} = \frac{i^2}{2\pi r k} R_l \qquad (66)$$

Thus the steepest temperature gradient is close to the heater. Also, the temperature gradient increases as the power into the heater increases. These features are in good agreement with the simulation results shown in Fig16.

The maximum power to the heater is limited by two factors:

i) heater thermal runaway for constant current driven heater; heater melting

ii) radiative heat loses.

If the condition i) and/or ii) apply, then the following consequences exist:

i) the sensing elements placed symmetrically besides the heater will mark a continuously increa-

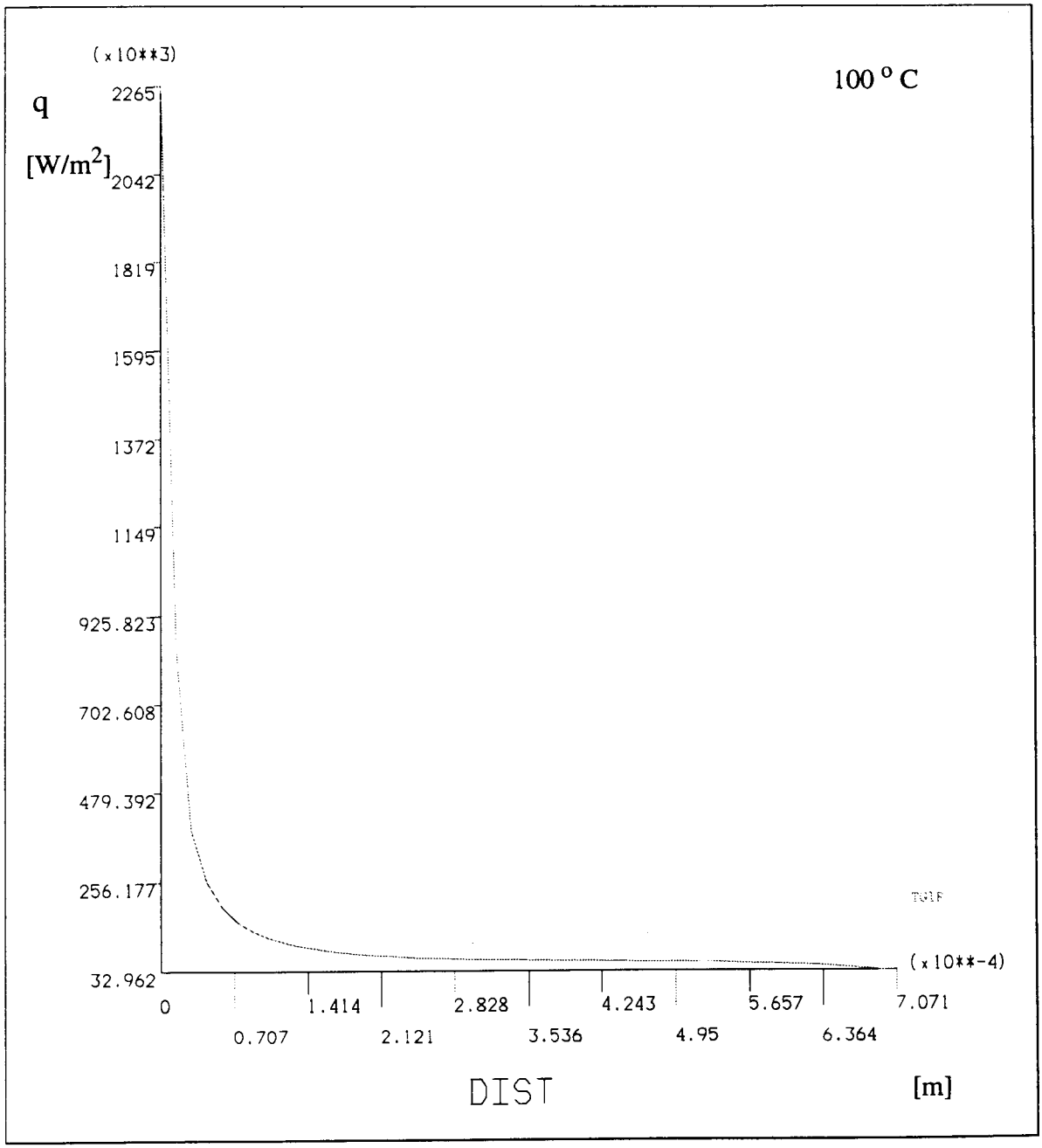

Fig.12a Radial heat flux distribution for 1mm enclosure and dT_H = 100 °C

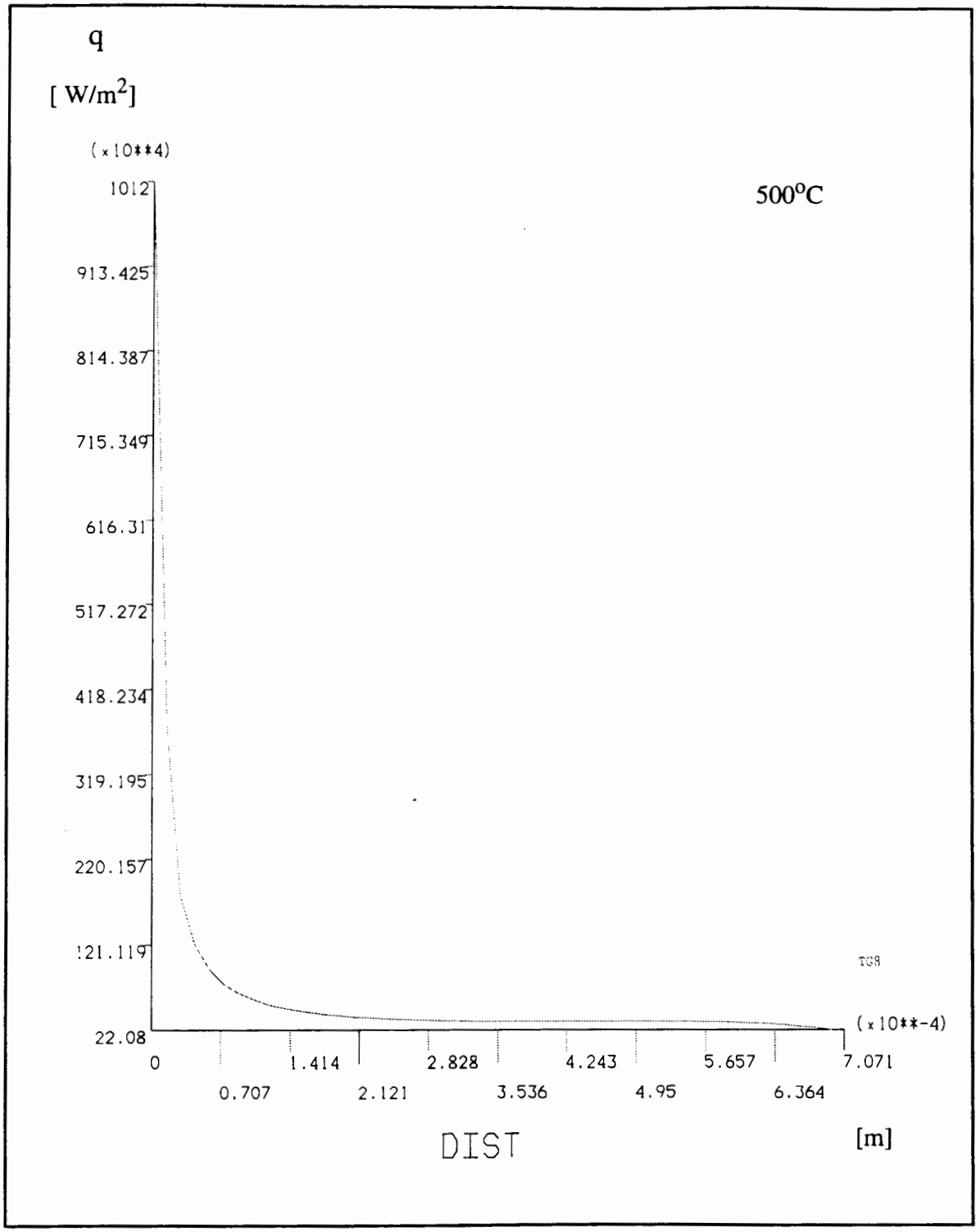

Fig.12b Radial heat flux distribution for 1mm enclosure and dT_H = 500 °C

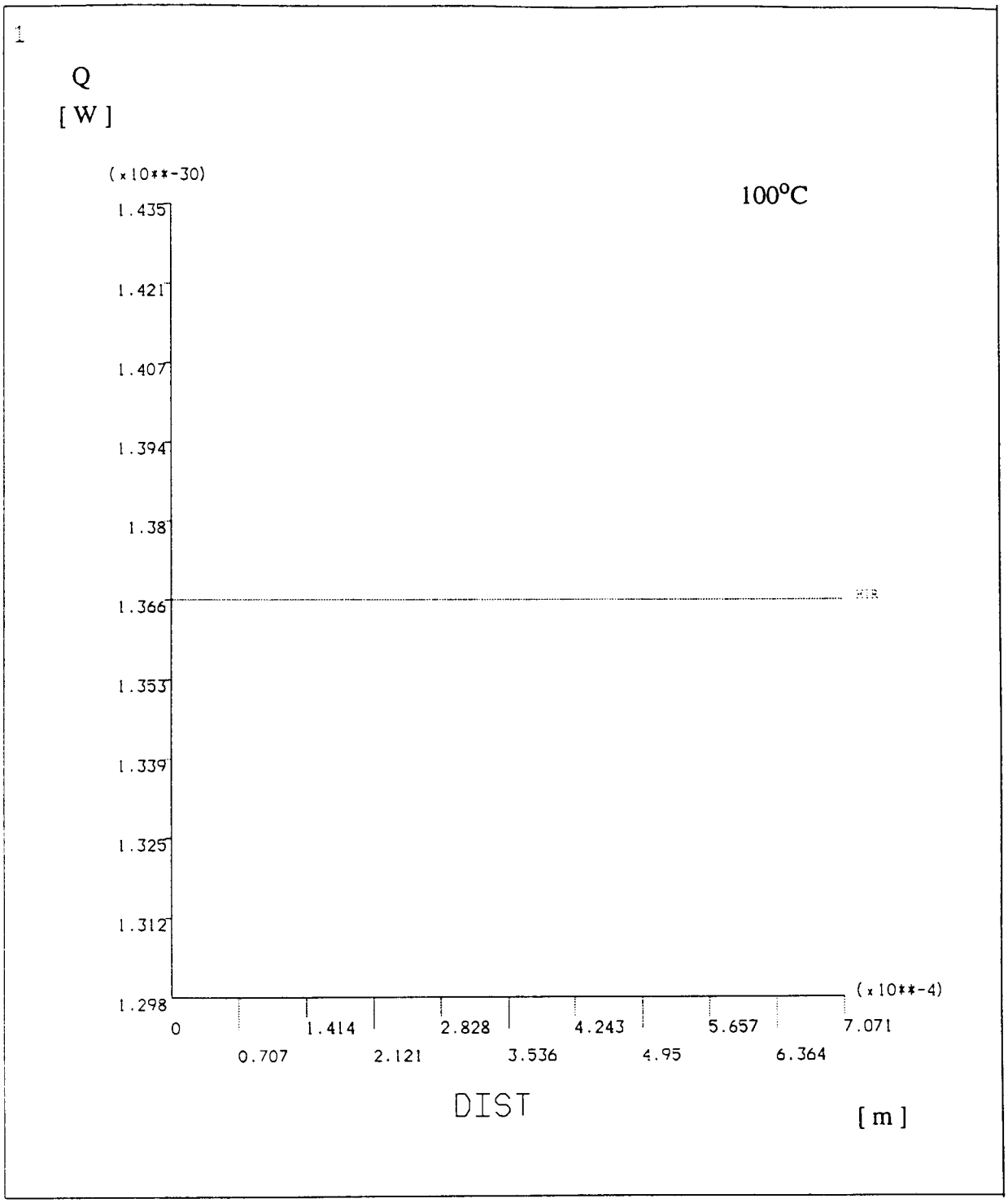

Fig.13a. Radial heat flow distribution at $dT_H = 100^oK$

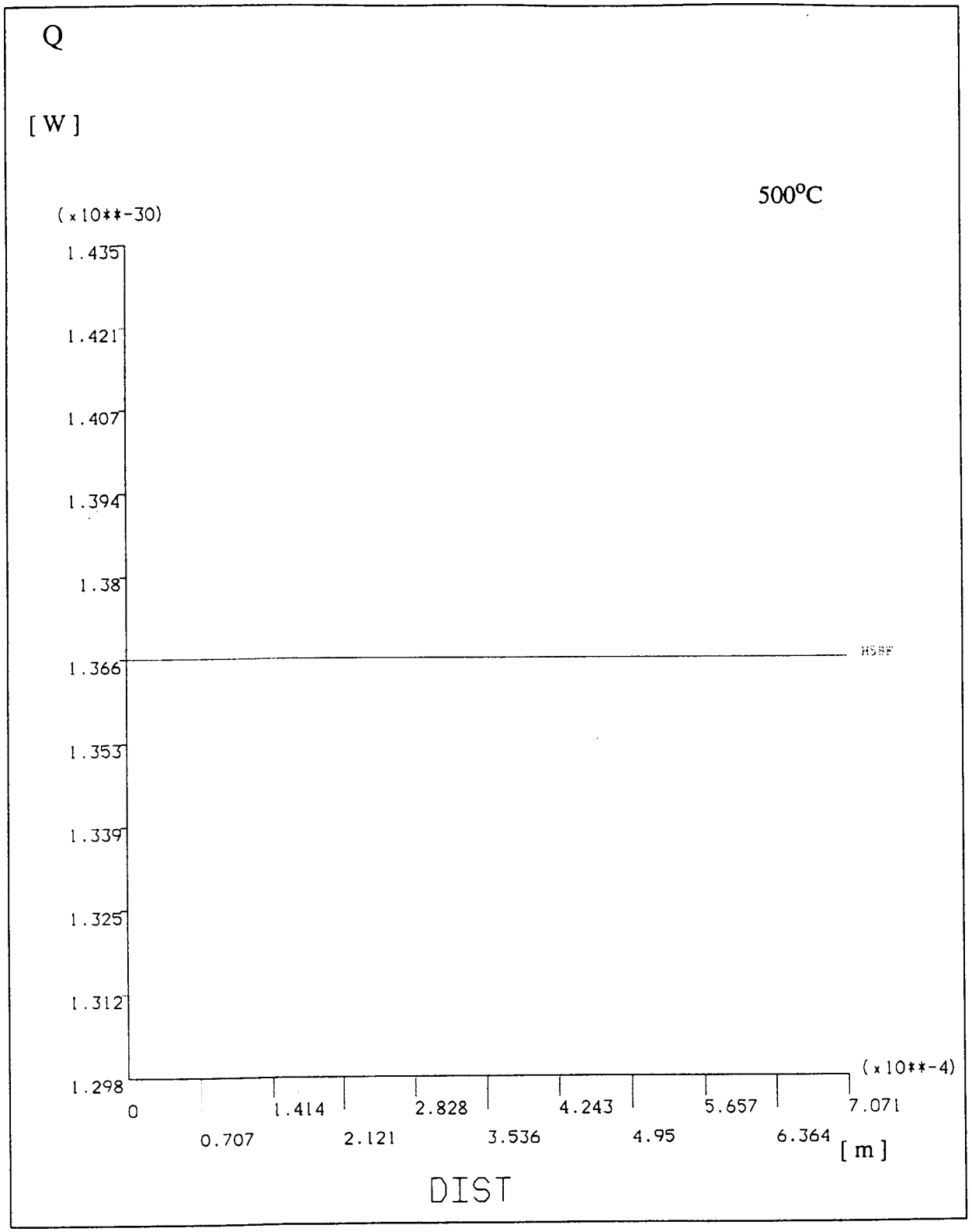

Fig.13b. Radial heat flow distribution at $dT_H = 500^oK$

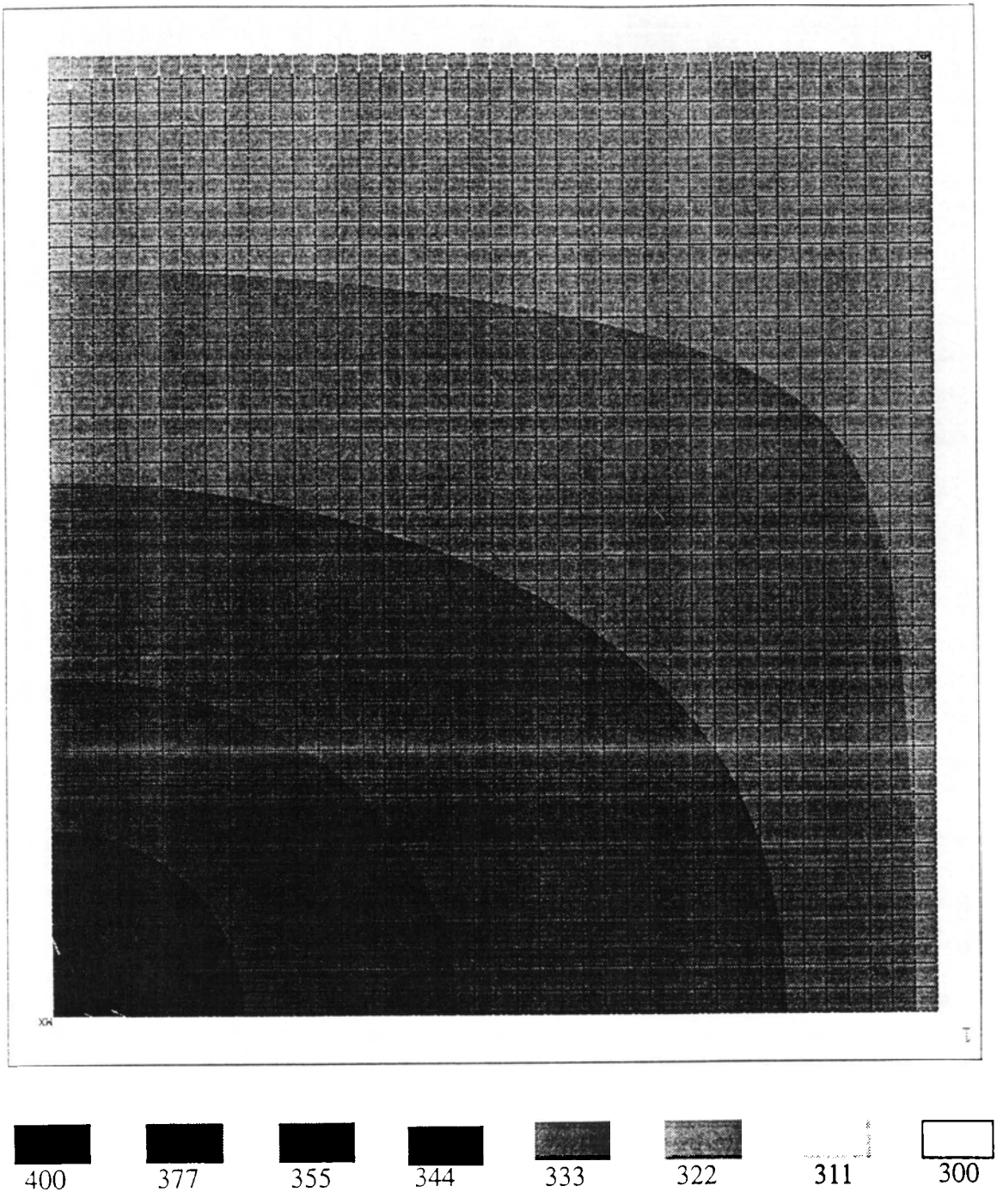

Fig.14a. Temperature distribution for 1mm enclosure and $dT_H = 100^0k$

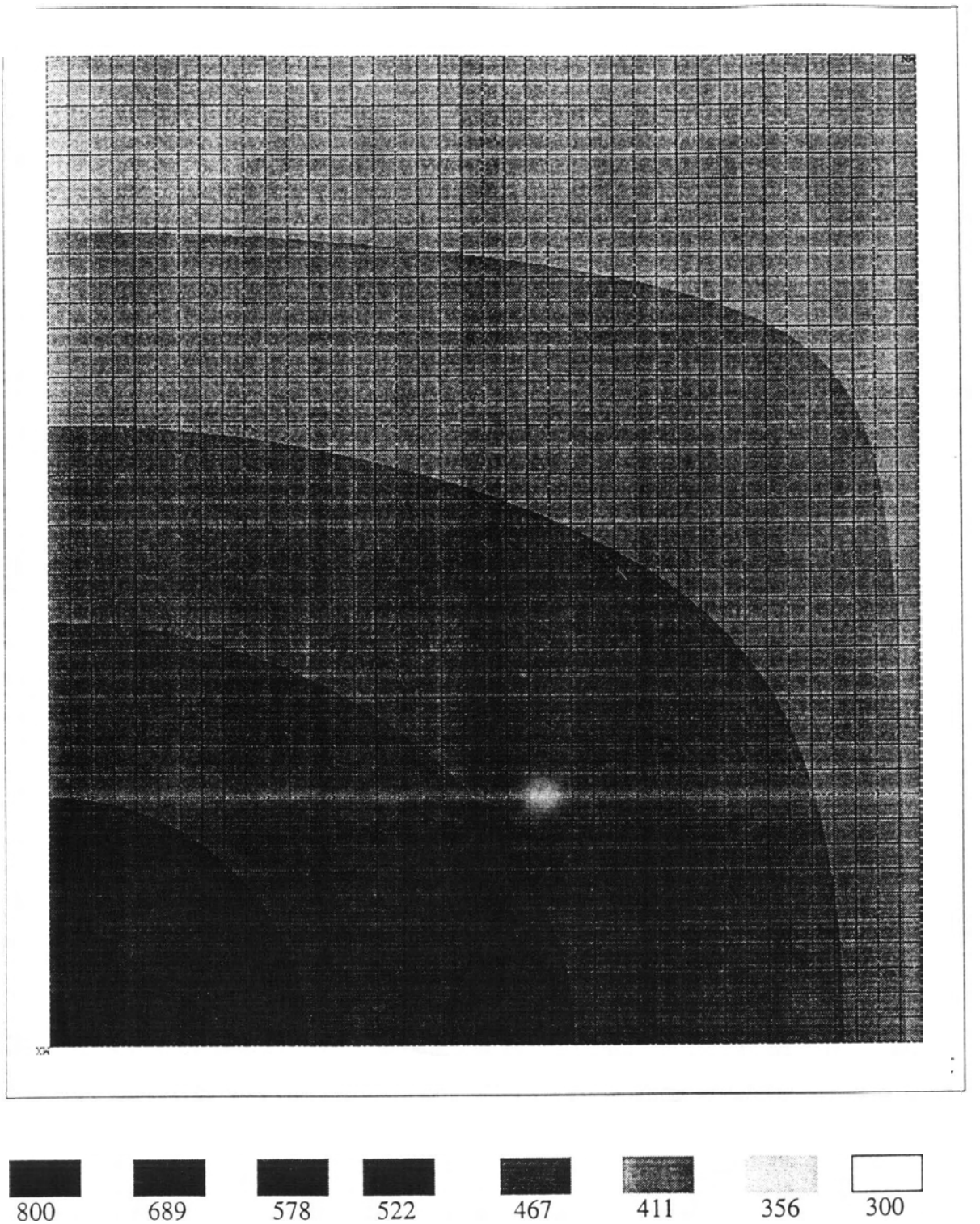

Fig.14 b. Temperature distribution for 1mm enclosure and $dT_H = 500^oK$

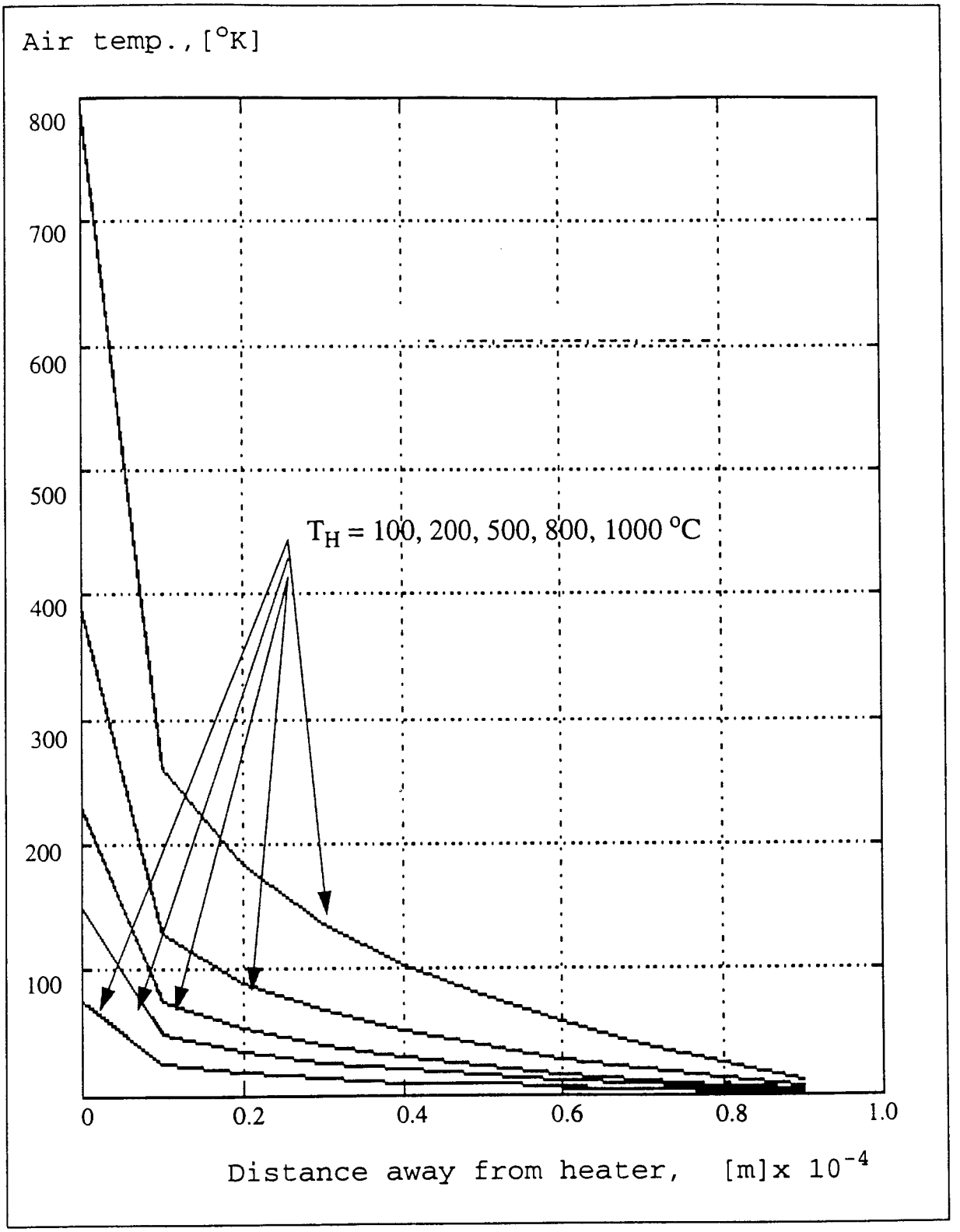

Fig.15. Calculated air temperature values vs. distance away from heater, with dT_H as parameter

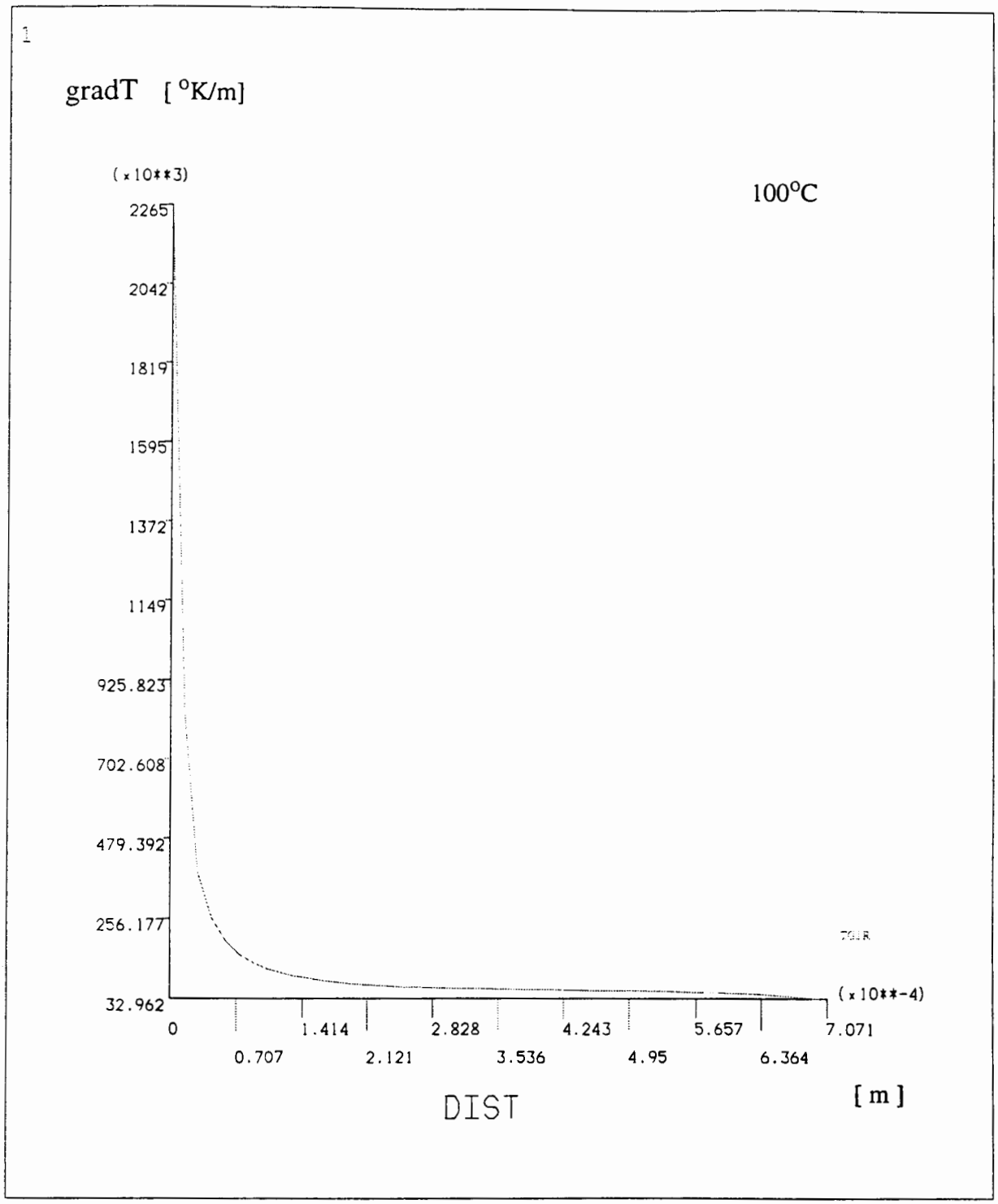

Fig.16a. Temperature gradient radial distribution for 1mm enclosure and $dT_H = 100\ ^{o}$ K.

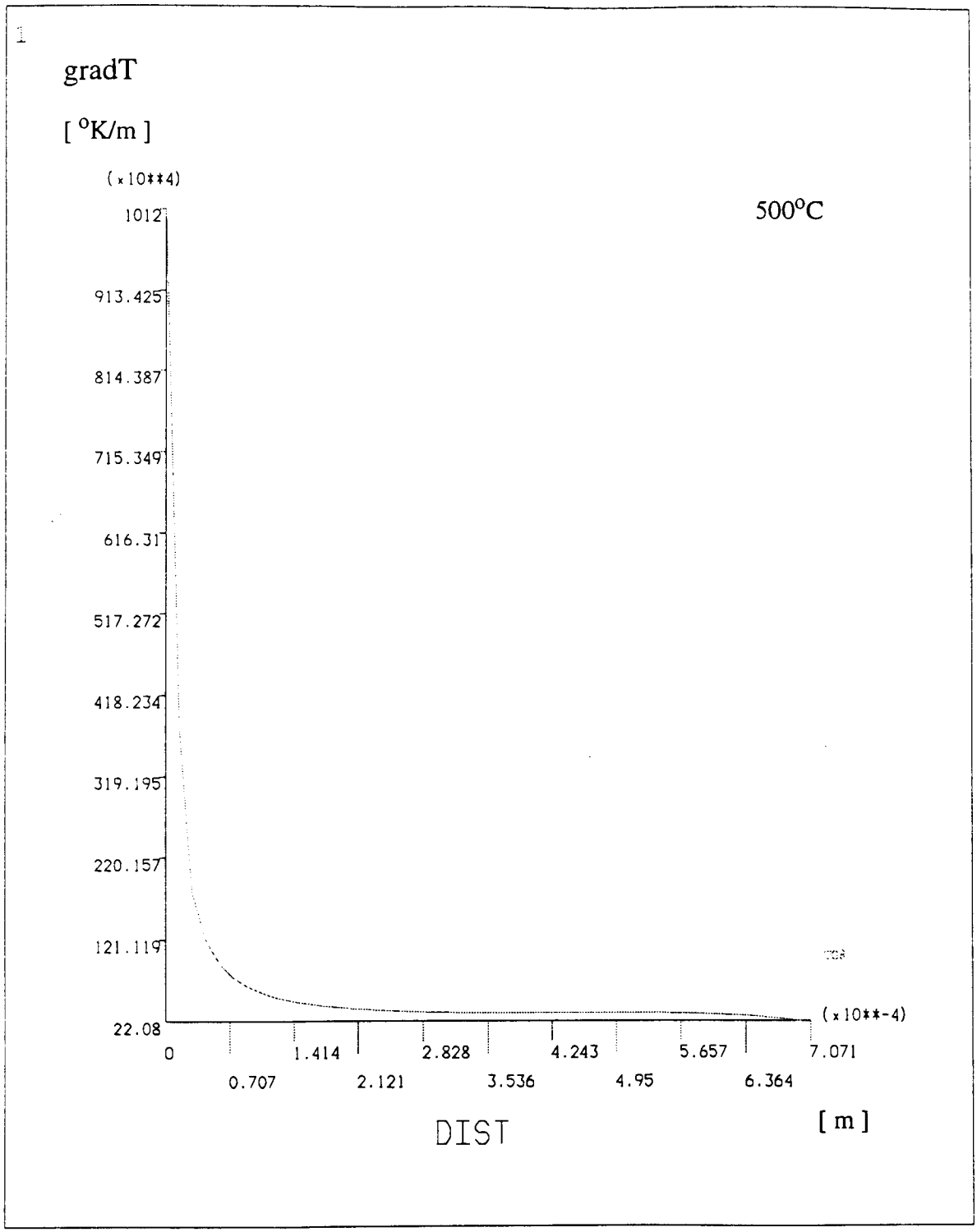

Fig.16b. Temperature gradient radial distribution for 1mm enclosure and $dT_H = 500\ ^{o}$ K.

sing temperature. Thus the DC level of the device O/P (Wheatstone bridge) will constantly increase.

ii) in radiative heat transfer, the temperature distribution is independent of position, The device will not work.

2.3.2. Sensing Elements.

The sensing elements are placed symmetrically in the heater temperature field. A combined convection/conduction heat transfer takes place at the sensor surface. They may or may not act as heat sinks. It depends on the conduction path from the sensor to the walls. The sensor will reach a steady-state temperature close to that of the surroundings if the conduction path's thermal resistance from sensor to walls is less than the convective resistance of the fluid surrounding the sensor. The relative magnitude of the two heat transfer modes is given by the Biot number. Its values for $L = 1\mu m; 10\mu m; 100\mu m$, $\Delta T \leq 1000K$, $g_{lev} \leq 10g$ were calculated in Section 2.1. The Biot number is less than 0.1 in the specified conditions. Thus the sensor will reach a steady-state temperature close to that of the surroundings. The time required for the sensor to reach steady-state will depend on its thermal mass.

2.4. Transient.

A heat transfer problem is transient whenever the temperature within the system being considered changes with respect to time.

2.4.1. Device Warm-Up Time.

After the power supply to the heater is turned on, a time will elapse until it and its surroundings reach a steady-state temperature. This is the device warm-up time. In the gaseous boundary layer

surrounding the heater, temperature rises at any point until it approaches the steady-state value given by eq.(62). The temperature rise in the gaseous layer surrounding the heater is [5, 10]:

$$T(r,t) = \frac{q \cdot r_s}{2k} \cdot ln\left[\frac{2.246\alpha t}{r^2}\right] + Q\left(\frac{r_s^2}{\alpha t}\right), \ (r > r_s) \qquad (67)$$

where α = air thermal diffusibility, r = distance away from heater, t = time.

Here, the gaseous layer surrounding the heater is modeled as a hollow cylinder made of air with inner radius r_S and outer radius $r_o \to \infty$. It is assumed that the air thermal diffusivity is constant in respect with temperature.The temperature as given by eq.(67) will increase at any point without limit. This is because the model contains a heat source, the prescribed heat flux q through the inner surface, but does not contain a heat sink. This is corrected by allowing the temperature as given by eq.(67) to rise at any point until it approaches the steady-state value given by eq.(62). The time required for this to happen is the device warm-up time.

First, the air steady-state temperature at various locations is estimated using eq.(62). Then, the transient temperature distribution, T(r,t) as given by eq.(67), is rewritten as a function of time only, T(t). The temperature evolution in time is then plotted for every heater surface temperature T_H with r, the distance away from the heater, as parameters. Thus for ΔT_H = 100,200,300,500,1000K five sets of plots will exist. For each set the intersection points between the steady-state temperature at different locations and T(t) will generate a curve. The extrapolation of this curve to T ambient will give the warm-up time of the device for the specified heater temperature.For a heater with L = 2000μm, r_S = 1μm the required electric power for different ΔT as given by:

$$Q[W] = i^2 \cdot R = q[W/m^2] \times 2\pi(r_S \cdot L) \qquad (68)$$

is listed in Table 9.

Table 9: Heater electric power, P_H, vs. dT_H

dT_H [°C]	100	200	300	500
P_H [mW]	26.6	30.8	33.6	40.6

The steady-state air temperatures at various locations vs. heater surface temperature are listed in Table 10. for $r_o = 1mm$. The temperature values are calculated using eq.(62).

Table 10: Air temp. vs. distance. Heater - enclosure separation is 1mm.

$\Delta T_H[k]$	$(T)_{r=2}$	$(T)_{r=10}$	$(T)_{r=20}$	$(T)_{r=40}$	$(T)_{r=80}$	$(T)_{r=160}$	$(T)_{r=200}$
100	78.25	63.15	56.7	50.2	43.7	37.16	35.4
200	137.43	106.98	93.97	80.9	67.76	54.6	50.45
500	315.9	239.2	206.4	173.43	140.36	107.2	96.7
1000	616.72	462.01	395.9	329.41	262.72	195.84	174.7

The calculated values are in relatively good agreement with the simulated results. A comparison of simulated and calculated results is given in Table 11. The differences are due to the air properties' dependence with temperature

Table 11: Comparison of simulated and calculated air temp. values for $L = 2000\mu m$, $r_S = 1\mu m$, $s = 1mm$.

$\Delta T_H[K]$		$T(r)$				
	obs.	$r = 20\mu m$	$40\mu m$	$100\mu m$	$150\mu m$	$200\mu m$
100	sim.	78.5	55.5	40	35	30
	calc.	56.7	50.2	43.7	37.16	35.4
200	sim.	142	110	89	78	62
	calc.	93.97	80.9	67.76	54.6	50.45

Table 11: Comparison of simulated and calculated air temp. values for $L = 2000\mu m$, $r_S = 1\mu m$, $s = 1mm$.

$\Delta T_H\,[K]$		$T(r)$				
500	sim.	-	-	-	-	-
	calc.	206.4	173.43	140.36	107.2	96.7

From the intersection points between the steady-state temperature at different locations and $T(t)$ for a given ΔT_H, a time history curve is generated. Its extrapolation to T_{amb} gives the device warm-up time. The time history curves are given in Figs.17 to 19. From these curves it can be seen that the device warm-up time is in the range of half of millisecond.

The above estimations do not include the heater's warm-up time. All estimations are made for a given constant heat flux released at heater surface. This corresponds to a steady-state heater temperature distribution.

2.4.2. Sensors' Speed of Response

The desired operation of the sensor requires that upon an applied acceleration a shift in temperature distribution should occur. This change in temperature distribution is caused by the buoyant force. The air temperature at each sensor will therefore change. The sensor reading will change correspondingly. Sensor reading's changing rate is a function of temperature's change rate at sensors and of their response time. The temperature change rate at the sensor is a function of the air motion rate. The sensor response to a temperature change at its location is a function of its thermal mass. Hence, if t_{sns} is the time needed for the sensor reading to change, then:

$$t_{sns} = t_r + t_T \tag{69}$$

where:

t_T=time needed for the air movement to induce a temp. change at sensor.

t_r=sensor response time to a temp. change at its surface.

In this scenario the following assumptions are made:

i) the fluid is moved along "en mass" by the walls' pressure. This means that there is no compression/expansion of the fluid due to the applied acceleration. The fluid is incompressible. Thus, it is considered that the external acceleration is uniformly applied throughout the fluid. Correspondingly, the only force tending to move any part of the air relative to the apparatus is the buoyancy force, B. If $\bar{a}$ is the acceleration acting on the apparatus, then:

$$\bar{B} = (\bar{a} + \bar{g})\,\Delta\rho \qquad (70)$$

is the buoyancy force per unit volume of heated air.

ii) the time needed for the shift in temperature distribution to occur is less than the time needed for the temperature distribution to get re-established, which is the device warm-up time.

iii) there might be also some air mixing which is neglected. The mixing effect would be to make the temperature distribution smooth, thus lowering the temperature gradient.

2.4.2a. Evaluation of t_T.

To estimate how fast the air moves, the hot air surrounding the heater is modeled as a solid cylinder with radius r_d, where r_d is the separation between heater and sensor. This cylinder is considered to be at a temperature $T(r_d)$ above ambient, where $T(r_d)$ is the steady-state temperature at the sensor location. In steady-state, the sensor temperature equals that of its surroundings. The forces experienced by the cylinder are the buoyancy force, B and the drag force F_d. These forces are given by the following equations:

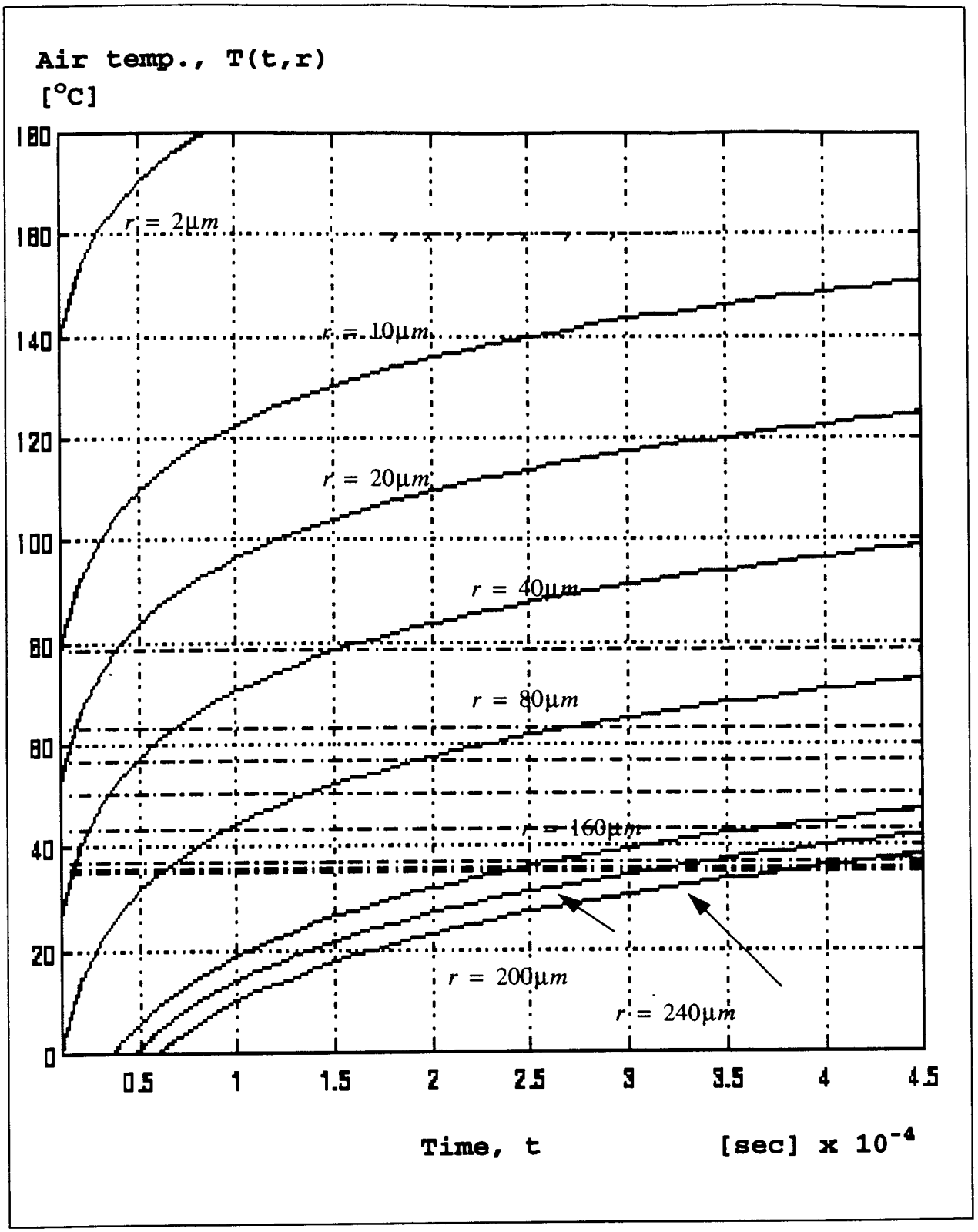

Fig.17. Time response curves, T(t,r), for $\Delta T_H = 100^o C$

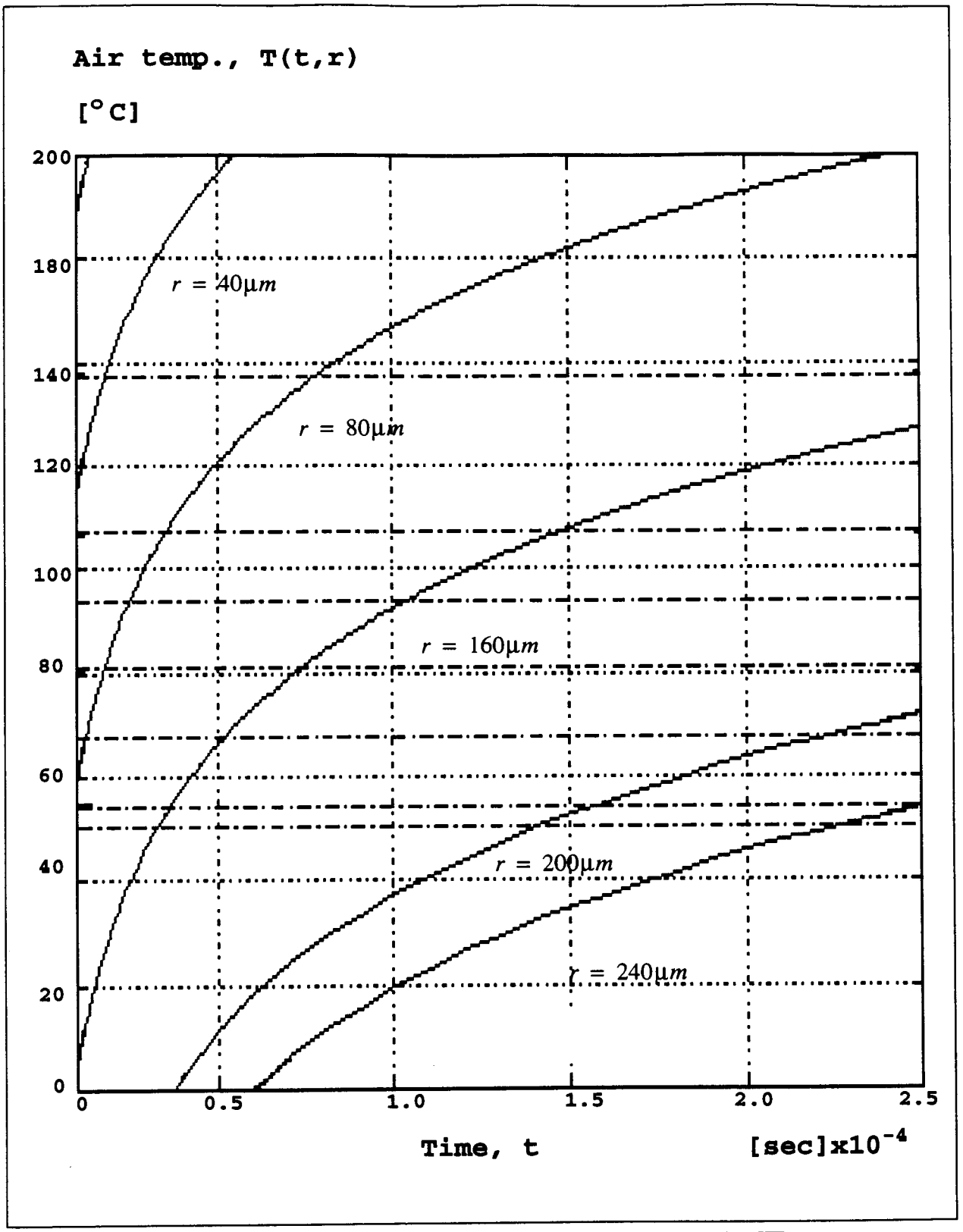

Fig.18. Time response curves, T(t,r), for $\Delta T_H = 200^\circ C$

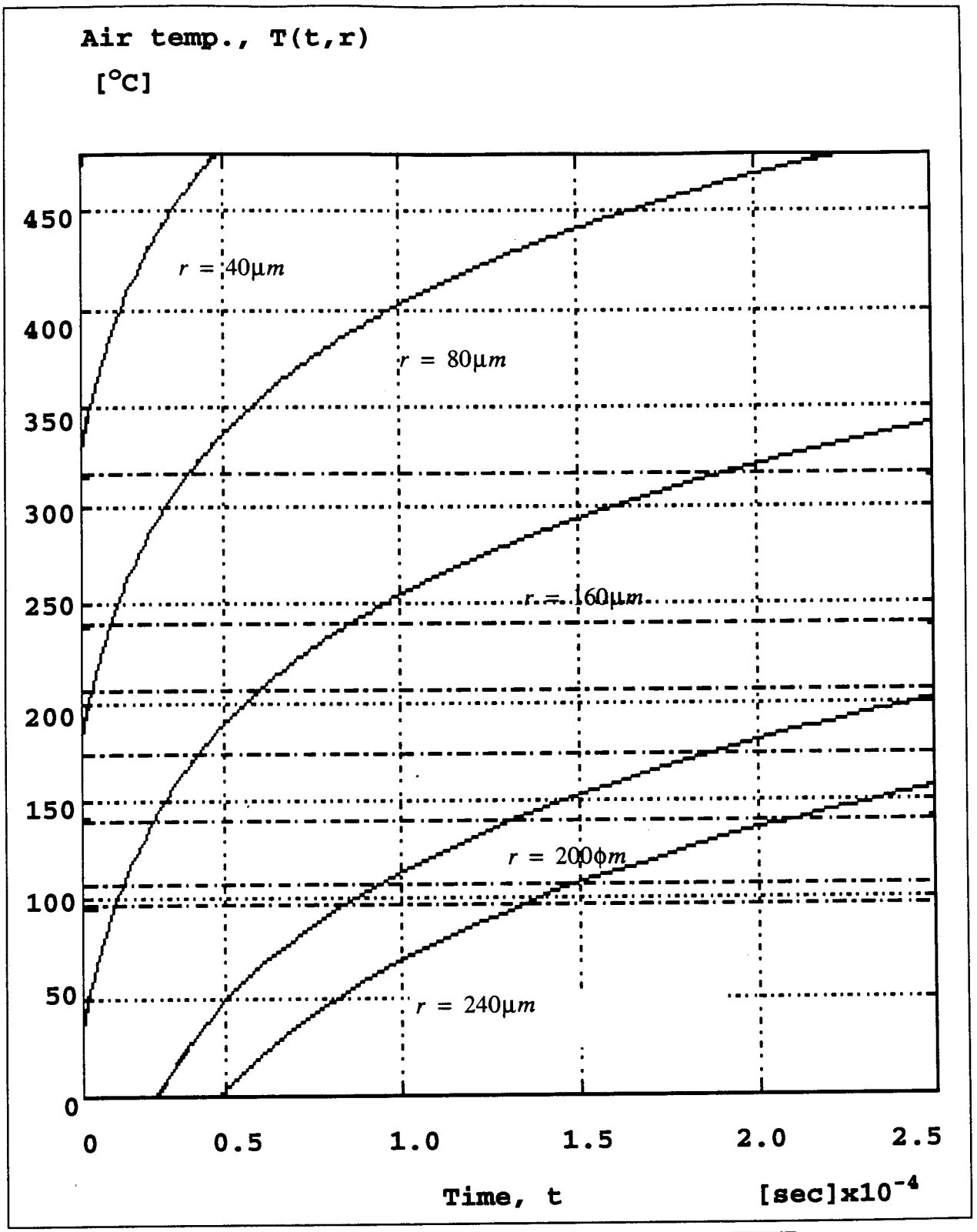

Fig.19. Time response curves, T(t,r), for $\Delta T_H = 500^\circ C$

$$B = \frac{aV\Delta\rho}{\rho}, \Delta\rho = \rho - \rho_\infty \tag{71}$$

$$F_d = 0.25\rho u^2 L r_d C_d (69) \tag{72}$$

where:

V =volume of the hot air cylinder.

a =imposed acceleration (to be detected).

ρ_∞ =cold air density.

ρ =hot air density.

u =velocity of the cylinder relative to the surrounding fluid.

L =cylinder length.

C_d =drag coefficient.

The drag coefficient is a function of the Reynold's number. The free-stream Reynold's number is given by the equation:

$$Re = \frac{2r_d u}{\gamma}, \gamma = \frac{\mu}{\rho} \tag{73}$$

where:

γ =fluid kinematic viscosity, $[m^2/s]$

μ =fluid absolute viscosity, $[N \cdot s/m^2]$

Thus Reynold's number and hence C_d is a function of u. C_d may be determined from an empirical correlation with the Reynold's number. For very small Reynold's numbers, $R_l < 4$, $C_d = 0.89$.

The cylinder reaches a terminal velocity u_t when:

$$B = F_d \tag{74}$$

By substituting eqns.(71) and (72) into (74), I get:

$$\frac{a\pi r_d^2 L \cdot \Delta\rho}{\rho} = \frac{1}{4} \cdot \rho u_t^2 (L \cdot r_d \cdot C_d)$$

so that:

$$u_t = \sqrt{\frac{4a\pi r_d}{\rho \cdot C_d}} \tag{75}$$

Since $C_d = C_d(\mu P)$, eq.(75) might be solved by iteration.

For:

$$g = 10\,(m/s)\,, r = 10\mu m, (\Delta\rho)/\rho = 1/100$$

I estimate:

$$u \sim 10^{-3}\,(m/s) = 1\,(\mu m)/(ms)$$

Thus u is in the order of microns per milliseconds. In this region, the relationship between velocity and drag effect can be approximated to:

$$F_d = 3L\mu u \tag{76}$$

The resulting force experienced by the cylinder is:

$$F = B - F_d \tag{77}$$

By substituting eq.(71) and (76) into (77), I get:

$$F = \frac{aV\Delta\rho}{\rho} - 3L\mu u \tag{78}$$

Hence the motion equation for the cylinder is:

$$\frac{du}{dt} = \frac{aV\Delta\rho}{\rho \cdot V\rho} - \frac{3L\mu u}{V\rho} \tag{79}$$

Eq.(79) is solved for the time-varying velocity of the cylinder as:

$$\frac{du}{dt} = C_1 - (C_2 \cdot u), \frac{1}{C_2}\frac{du}{dt} = \frac{C_1}{C_2} - u \tag{80}$$

where:

$$C_2 = \frac{3L\mu}{\rho L\pi (d^2/4)} = \frac{12\mu}{\rho\pi d^2} \tag{81a}$$

$$C_1 = \frac{a\Delta\rho}{\rho} \tag{81b}$$

In order to integrate eq.(80) I define:

$$v = C_1 - C_2 u$$

so that:

$$u = \frac{C_1}{C_2} - \frac{v}{C_2}$$

$$du = -(\frac{1}{C_2} \cdot dv)$$

Eq.(80) becomes:

$$-\frac{1}{C_2}\frac{dv}{dt} = v \tag{82}$$

By integrating this I get:

$$ln\gamma = (-C_2)\, t$$

and:

$$\gamma = exp\,(-C_2 t)$$

Hence:

$$C_1 - C_2 u = exp(-C_2 t)$$

and:

$$u = \frac{C_1}{C_2}[1 - exp(-C_2 t)] \tag{83}$$

By substituting C_1, C_2 constants as given by eqns.(81a), (81b), I get the cylinder's motion equation:

$$u(t) = u_t\left[1 - exp\left(\frac{12\mu t}{\rho \pi d^2}\right)\right] \tag{84}$$

The cylinder reaches its terminal velocity in about $0.04ms$. Thus $t_T \sim 0.04ms$. Hence $t_T \ll t_d$ since $t_d \sim 0.4ms$. Therefore, I can assume that the air temperature distribution remains fixed as it moves along upon an applied acceleration to the apparatus.

Once the air's motion equation is known, the travel distance required to reach terminal velocity, s_T can be estimated as:

$$s_T \sim u_t \cdot t_T \qquad , \qquad s_T = \int u(t)\, dt$$

Since $u_t \sim 1\ (\mu m)/(ms)$ and $t_T \sim 0.04ms$, the travel distance is in the order of half of micron for 1g applied acceleration. Based on this distance and on eq.(62) (steady-state air temp. distribution), the rate at which the temperature changes at each detector can be estimated. It depends on the temperature gradient at the sensor location:

$$\frac{d}{dr}T(r) \sim -\frac{1}{r} \tag{85}$$

From eq.(62), the air temperature above the ambient at the sensor location, r_d, is:

$$T(r_d) = \frac{Q}{2\pi kL} ln \frac{r_o}{r_d}$$

where r_0=separation heater-enclosure and

$$T(r_d+\Delta r) = \frac{Q}{2\pi kL} ln \frac{r_o}{r_d+\Delta r} = \frac{Q}{2\pi kL} [lnr_o - ln(r_d+\Delta r)] \qquad (86a)$$

Using the Taylor series I get:

$$T(r_d+\Delta r) = \frac{Q}{2\pi kL} ln \frac{r_o}{r_d} - \frac{Q}{2\pi kL} \frac{(\Delta r)}{r_d} \qquad (86b)$$

$$T(r_d+\Delta r) - T(r_d) = -\frac{Q}{2\pi kL} \frac{(\Delta r)}{r_d} = -C_1(Q_l) \frac{(\Delta r)}{r_d}$$

where $Q_l = Q/L$ =heating power per unit length.

For $\Delta r = 1\mu m$, $r_d = 200\mu m$ and $\frac{Q}{2\pi kL} = 20^o K$, the temperature change at the detector is:

$$\Delta T(\Delta r) = 0.1^o K$$

In order to see how fast the sensor responds to a change in the air temperature at its surface, the resistance of the layer of stagnant air must first be determined. The free-stream Reynold's number for air flowing at u_t past a cylinder of diameter $D = 2r_S$ is

$$Re = \frac{2r_S u_t}{\nu} \qquad (87)$$

For $r_S = 1\mu m$, $u_t = 10^{-3}$ m/s and $\gamma = 10^{-5}$ m^2/s, I get $Re = 0.0002$.

The average Nusselt number, hL/k, can be related to the free-stream Reynolds number,

$(uD)/\gamma$, and the Prandtl number, $(c_p \cdot \mu)/k$, by an empirical correlation equation:

$$Nu_D = \frac{hD}{k} = const\,(Re_D)^n Pr^{1/3} \tag{88}$$

where $const = 0.989$ (empirical correction factor), $n = 0.33$ for $Re < 4$ [7].

Eq.88 is similar to that for flow through a duct:

$$Nu_D = 1.86\left(\frac{\mu_b}{\mu_S}\right)^{0.14} (Re_D Pr)^{0.33} \left(\frac{D}{L}\right)^{0.33} = const\,(RePr)^{0.33} \left(\frac{D}{L}\right)^{0.33} \tag{89}$$

where the length dimension in Re and Nu numbers must be the appropriate outside dimension of the object, which for flow over cylinders is the diameter:

$$\left(\frac{D}{L}\right)^{0.33} = 1^{0.33}$$

The empirical correction factor $1.86\left[\frac{\mu_b}{\mu_S}\right]^{0.14}$ is introduced to account for the distortions of the velocity parabolic profile that appear at the solid-fluid interface due to the temperature variations effect on the fluid viscosity. This correction factor's values, C, are empirical related to the Re number values [7].

Table 12: C, n constants correlation to Re for use in eq.(88)

Re	C	n
<4	0.989	0.33
4 - 40	0.911	0.385
40 - 4000	0.683	0.466
4000 - 40000	0.193	0.618

For $Re = 0.0002, Pr = 0.7$ the corresponding Nu number is $Nu = 0.053$ and hence:

$$h = Nu \cdot \frac{k}{2r_S} = 530 W/(m^2 K) \tag{90}$$

The relative importance of the air thermal resistance and the silicon thermal resistance is given by the Biot number:

$$Bi = \frac{hr_S}{k} = 0.0006 \tag{91}$$

When the Biot number approaches zero, the solid is practically isothermal and the temperature varies mostly in the fluid. Thus the isothermal resistance of the sensor can be neglected. Hence it can be considered that, as a result of an acceleration, the air close to the detector suddenly goes from the detector temperature T_d to a new temperature T_f. In other words, the sensing body at T_d is suddenly immersed in a bath of fluid at a different temperature, T_f, at the time t=0. If:

T_d= body temp. just before immersing it into the fluid;

T_S= body surface temp. after immersing (it is dependent on time elapsed after immerging);

then:

$T_i = T_d - T_S$ = temperature variation across the body at t = 0.

It is negligible relative to $T_d - T_f$ because $Bi < 0.1$.

The time after which body surface temper5ature, T_S, equals core body temperature, T_d, is the time of thermal penetration, t_C. It is given by the equation [38]:

$$t_C \sim \frac{r^2}{\alpha} \tag{92}$$

where:

r = characteristic dimension of conducting body

α = thermal diffusivity of conducting body.

After the time of thermal penetration, the temperature all throughout the body is the same and as time elapses it tends towards the fluid temperature.

For $r_{sensor} = 1\mu m$ and $\alpha_{silicon} = 93.4 \cdot 10^{-4} (m^2/s)$, the transition time scale is $t_C \sim 10^{-8} s$. Thus it can be concluded that the instantaneous temperature, $T(x, t)$, has practically the same value throughout the body, $T(t)$ only, for the specified conditions ($Bi < 0.1$, $t > t_C$). Hence the lumped capacitance model alone is a good description for time-dependent conduction. (For $t < t_C$ a proper sequence of conduction regimes can adequately represent the transient conduction phenomenon, Fig.20).

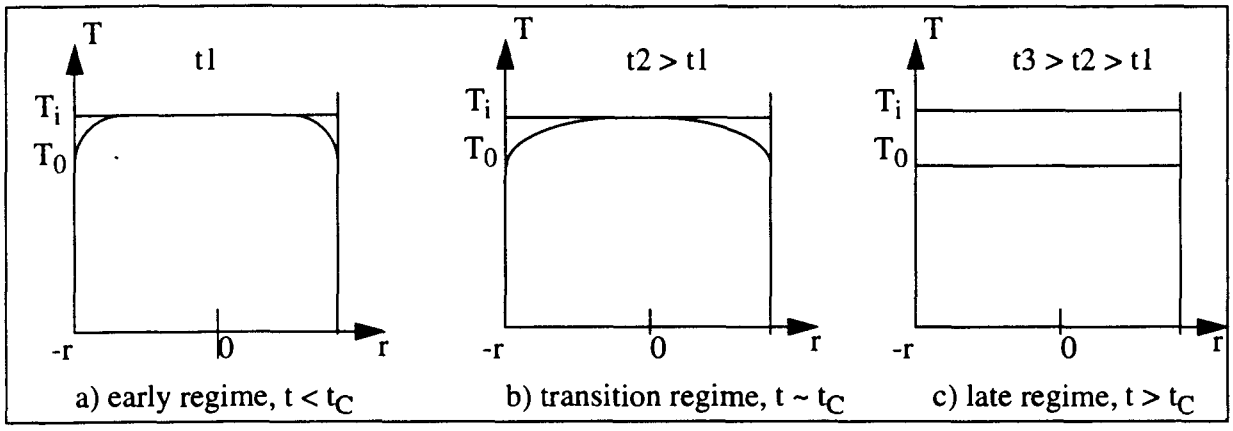

Fig.20 Time dependent conduction regimes. Here: T_i=initial body temperature; T_0=surface body temp. after immersing; δ=skin layer, $\delta \sim (\alpha t)^{1/2}$

The governing equation is obtained by applying an energy balance to the solid. It indicates that the increase in stored energy in the solid must equal the heat transfer rate into the surface in convective mode:

$$\rho V c_p \cdot \frac{d}{dt} T(t) = hA_S [T_f - T(t)] \qquad (93)$$

To solve eq.(93) an initial condition must be specified:

$$T(t) = T_i \qquad \text{at} \qquad t = 0 \tag{94}$$

The solution of eq.(93) will specify the temperature $T(t)$ for all points within the solid, including the surface. It is [11,38]:

$$\frac{T - T_f}{T_d - T_f} = exp\left[-\left(\frac{hA}{\rho V c_p}\right) t\right] \qquad \text{, assuming } h\text{=constant.} \tag{95}$$

The constant convective heat transfer coefficient is a good assumption if temperature changes at the detector are small. It has been shown that the temperature change at the detector is $0.1K$ for a detector with radius of $1\mu m$ located $200\mu m$ away from the heater.

The factor in the exponent can be expressed as:

$$\frac{hA_S t}{\rho V C_p} = \left(\frac{hr_S}{k}\right)\left(\frac{\alpha t}{r_S^2}\right) = (Bi)\ (Fo) \tag{96}$$

where Fo is the Fourier number. It expresses the rate of heat transfer by conduction to the rate of energy stored in a material. Eq.(95) can now be written as:

$$T - T_f = (T_d - T_f)\, exp\,[-(Bi)\ (F_o)\,] \tag{97}$$

The sensor temperature varies exponentially in time. A time constant τ can be defined as:

$$\tau = \frac{\rho C_p V}{hA_S} \tag{98}$$

Using this notation, the solution of the transient conduction equation, eq.(95), is:

$$T - T_f = (T_d - T_f)\, exp\left[-\frac{t}{\tau}\right] \tag{99}$$

The time constant values for two detector radius at different temperatures are given in Table 13 The corresponding convective heat-transfer coefficients are listed in Table 14.

Table 13: Transient conduction time constants vs. detector radius.

$r_S\,[\mu m]$	$\tau\,[ms]$							
	$T_f = 20°C$	$40°C$	$80°C$	$100°C$	$160°C$	$200°C$	$300°C$	$400°C$
$1\mu m$	1.23	1.166	1.05	1.00	0.89	0.83	0.72	0.64
$10\mu m$	39.96	37.8	34.2	32.67	29.07	27.1	23.38	20.68

The transition's time scale is $t_C = r_0^2/\alpha \approx 0.1\mu s$ for $r_S = 1\mu m$ and $t_C \approx 10\mu s$ for $r_S = 10\mu m$ at $T_f = 20°C$ above ambient.

Table 14: Convective heat transfer coefficients for transient conduction. Applied acceleration $a = 1g$.

L_C $[\mu m]$	h $[W/m^2\,K]$							
	$T_f = 20°C$	$40°C$	$80°C$	$100°C$	$160°C$	$200°C$	$300°C$	$400°C$
$1\mu m$	661.97	698.89	772.74	809.66	909.88	975.82	1131.4	1279.1
$10\mu m$	203.9	215.33	238.08	249.46	280.34	300.65	348.6	394.1

From Tables 13 and 14 it can be seen that:

1) if the radius of the detector is increased one order of magnitude then the detector's speed of response drops at least one order of magnitude. For an increase in r_S by n times, h would get smaller [eq.(90)] by n times too. Also, the ratio h/r_S in the τ expression [eq.(94)]:

$$\frac{\rho C_p V}{h A_S} = \frac{\rho C_p r_S}{2h} = \frac{\rho C_p}{2} \cdot \frac{r_S}{h}$$

would decrease as $1/n^2$:

$$\frac{h}{r_d} = \frac{h}{n} \frac{1}{n r_s} = \frac{1}{n^2} \cdot \frac{h}{r_s}$$

So if the response time is to be short, then the detectors must be thin.

The calculated detector response time for $T_f = 20°C$ above ambient and applied acceleration 1g is 1.2ms for a detector radius $r_S = 1\mu m$ and 37.8ms for a detector radius $r_S = 10\mu m$.

2) the detector's time constant is decreasing with increasing fluid temperature. This behavior is due to the convective heat transfer coefficient's change with temperature. From eqns.(87) and (75):

$$Re \sim \sqrt{\frac{a}{\mu(T)}} \sim \frac{\sqrt{a}}{\sqrt{T}}$$

where: a = applied acceleration

$\mu(T)$ = absolute viscosity

T = air temperature.

So that from eqns.(88) and (90) for a given r_S:

$$h \sim Nu(Re) \cdot k(T) \sim (k(T)) / (\sqrt{T})$$

The convective heat transfer coefficient is increasing with temperature as the air thermal conductivity does. It can be concluded that the detector constant time would be shorter if:

- the detector is made smaller;
- the air temperature at detector is larger;

- the detector material property values ρ, C_p are smaller;

- the applied acceleration is larger.

For $t = \tau$ the detector temperature is 63% of that of the air temperature:

$$T - T_d = 0.63 T_f \qquad \text{(from eq.(95))}$$

Thus a detector with $r_S = 1\mu m$ will reach 63 per cent of the (suddenly changed) air temperature in 1.2ms, if the air temperature is $20°C$ above ambient and the applied acceleration is 1g. It will take longer if the air temperature above ambient is lower.

In all the above calculations it was assumed that the convective heat transfer coefficient is constant for a given air temperature at detector location. Thus it is assumed that the temperature change at detectors is small, which is the case. The time needed for the sensor reading to change is in the order of a few milliseconds for $r_S = 1\mu m$.

Chapter 3. Device Design.

3.1. Structural Design.

The intended device structure consists of suspended bridges, each bridge being an electrical resistance supported on an oxide substrate. The bridge mechanical robustness and its natural resonant frequency will be discussed.

3.1.1. Natural Resonant Frequency.

The bridge dimensions are length L, width W and thickness t. It is a solid beam clamped at both ends. Its natural resonant frequency is given by its mass and structure. By structure is meant geometry and material properties. It is important to evaluate the beam resonant frequency because the normal operation of the device assumes that the device experiences a constant acceleration.

If the applied acceleration is given by a harmonic disturbing force:

$$F = F_0 \sin \omega t \tag{100}$$

where $\omega = 2\pi f$ and f the frequency of forced vibration, then the beam acts as a forced elastic vibrator. When a body is vibrating in air or in liquid with small velocities, then there will exist a resisting force proportional to the body's velocity:

$$R = const \cdot \dot{x} = c \cdot \dot{x} \tag{101}$$

If the forced elastic vibrator is modeled as a spring-mass system, the resulting vibration due to F and R will be described by the differential equation (for free damped vibration):

$$m \cdot \ddot{x} + c \cdot \dot{x} + k_e \cdot x = 0 \tag{102}$$

where: x = displacement; k = equivalent spring constant.

The motion equation for forced vibration is:

$$m \cdot \ddot{x} + c \cdot \dot{x} + k_e \cdot x = F_0 \sin \omega t \tag{103}$$

The free vibration component will be damped out in a short time, after which only the forced vibration will exist. The displacement in forced vibration is:

$$x = X(\omega) \sin(\omega t - \phi) \tag{104}$$

where $X(\omega)$ = displacement amplitude. The displacement amplitude is given by:

$$X(\omega) = \frac{F_0}{\sqrt{(\omega_n^2 - \omega^2)^2 + (c\omega)^2}}$$

$$X = \frac{F_0}{k_e} \times \frac{1}{\sqrt{\left[1 - \left(\frac{\omega}{\omega_n}\right)^2\right]^2 + 4\zeta^2 \left(\frac{\omega}{\omega_n}\right)^2}} \tag{105}$$

If ϕ is the phase of displacement (the amount by which the phase lags behind the disturbing force), then:

$$\phi = \operatorname{atan} \frac{2\zeta \left(\frac{\omega}{\omega_n}\right)}{1 - \left(\frac{\omega}{\omega_n}\right)} \tag{106}$$

where: ω_n = undamped natural frequency of spring mass system; ζ = damping factor and $\frac{F_0}{k}$ = zero frequency deflection. The zero frequency deflection is the statical deflection which would result if a steady force of magnitude F_0 is applied to the spring with stiffness k_e. The damping factor is given by:

$$\zeta = \frac{c}{c_c} \tag{107}$$

where: $$c_c = 2\sqrt{\frac{k_e W}{g}} \quad = \text{critical damping} \tag{108}$$

and $$c = \frac{R}{\dot{x}} \tag{109}$$

The undamped natural frequency of the spring is given by:

$$\omega_n = \sqrt{\frac{k_e}{w}} = \frac{2\pi}{\tau} \quad . \tag{110}$$

When $\zeta \neq 0$, the natural frequency ω_d is:

$$\omega_d = \omega_n \cdot \sqrt{1-\zeta^2} = \frac{2\pi}{\tau_d} \tag{111}$$

where τ_d = period of viscous undamped vibration.

For $\zeta = 0$, we have:

$$\tau = \tau_d = 2\pi\sqrt{\frac{w}{k_e}} = 2\pi\sqrt{\frac{\delta_{st}}{g}} \tag{112}$$

where δ_{st}=s tatical deflection of spring under the action of the weight w.

The vibration's amplitude and phase undergoes a sharp change at ω/ω_n. A magnification factor is defined, $M = \frac{Xk_e}{F}$. There are two distinct regions [39]:

1) when the disturbing force F has a very low frequency, $\omega \ll \omega_n$, the ratio ω/ω_n is small and the magnification factor is maximum with the phase approaching zero:

$$M \to 1, \ \phi \to 0.$$

2) the disturbing force frequency is high compared to the natural frequency of the system so that

the ratio ω/ω_n is large and the magnification factor approaches zero:

$$M \to 0 \ , \ \phi \to 180°.$$

The effect of damping is small in either of these extreme cases. It is important in the resonance neighborhood (frequencies on each side of resonance for which the amplitude is $\sqrt{2}$ of the amplitude at resonance). The magnification factor value at resonance increases as the damping factor decreases.

The structural damping is usually encountered as proportional to displacement, but out of phase with the velocity of the harmonic oscillation. The governing equation (103) becomes:

$$m\ddot{x} + (1 + i\gamma)\, k_e x = F\sin\omega t \tag{113}$$

where: γ = structural damping coefficient; its values range from 0 to 0.5. The magnification factor and its resonance value are:

$$M = \frac{1}{\sqrt{\left[1 - \left(\frac{\omega}{\omega_n}\right)^2\right]^2 + \gamma^2}} \tag{114}$$

$$M_r = \frac{1}{\gamma} \quad ; \ M_r \in [20, \infty] \tag{115}$$

Thus in the neighborhood of resonance the structural damping behaves like viscous damping of value 2ζ.

From a structural point of view, the device's suspended bridges are single-span beams clamped at both ends. The fundamental frequency for a single-span beam clamped at both ends is:

$$f_n = \sqrt{\frac{k_{eq}}{M_{eq}}} = \frac{\alpha}{2\pi}\sqrt{\frac{192 I_e E}{0.37 m_b L^3}} \tag{116}$$

where:

m_b = beam mass;

L = beam length;

E = modulus of elasticity;

I = moment of inertia of cross-sectional area about neutral axis;

a = dimensionless coefficient depending on fixing.

For silicon made bridges $E = 160 \cdot 10^9 (N/m^2)$. The moment of inertia about the neutral axis (Fig.21) is:

$$I_e = \frac{wt^3}{12} \qquad (117).$$

$$I_e = \frac{wt^3}{12} = 1.16 \cdot 10^{-24} m^4$$

The beam mass is ($w = 14\mu m, t = 1\mu m, L = 2000\mu m$):

$$m_b = \rho V = 2330\,(Kg)/m^3 \times 14 \times 1 \times 2000 \times 10^{-18} m^3 = 65.24 \times 10^{-12} Kg$$

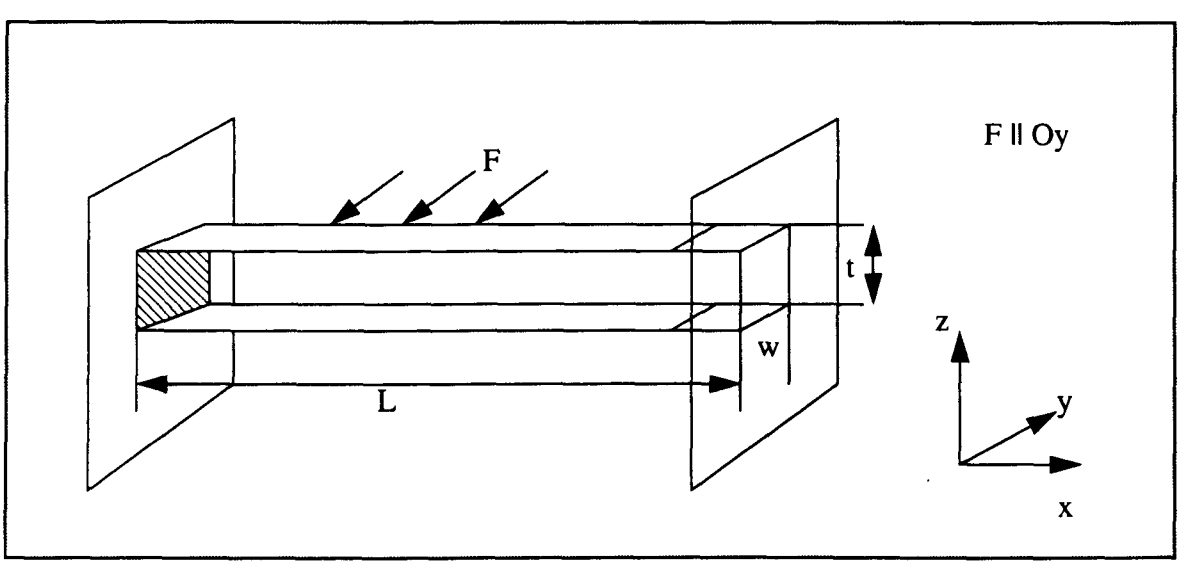

Fig.21. Moment of inertia about the neutral axis for a single-span beam clamped at both ends.

By substituting E,I,L,a and m_b values into eq.(116), I get:

$$f_n = 2.16kHz$$

The natural resonant frequency of a silicon bridge with $L = 2mm, w = 14\mu m, t = 1\mu m$ is $f_n = 1.3kHz$. In the resonance neighborhood the bridge itself will have a displacement approaching its maximum. This displacement may cause the temperature reading of the sensors not to correspond to the hot air displacement as intended. If the operating frequency is $\omega \ll \omega_n$ then $M \rightarrow 1$ and $\phi \rightarrow 0$, so that the bridge displacement's amplitude is constant in respect to the operating frequency ω. If the operating frequency is $\omega \gg \omega_n$ then $M \rightarrow 0$ and $\phi \rightarrow 180°$, so that the bridge displacement is zero and the phase angle is maximum. The natural frequency of the single-span beam clamped at both ends is proportional to t/L^2 for a given material (E,ρ).

3.1.2. Mechanical Robustness.

The published working principles for various accelerometers are based on the movement of a solid suspended part of the device. This makes them susceptible to fracture and thus very fragile. The proposed device structure is based on air movement. The solid parts of the device are clamped suspended bridges. Thus the proposed structure is more robust than the published ones.

The mechanical strength of the suspended bridges depend on the bridge structure. For bridges made out of silicon, the <110> crystallographic orientation would be the best since the Si mechanical strength is maximum along <110> direction. However, it is not possible to get a straight, suspended bridge along <110> direction because of the Si anisotropic etching properties. Any deviation of the bridge direction from the <110> orientation would determine the bridge undercutting.

Diffused etch-stop layers usually have substantial tensile stress. The tensile stress tends to shrink the bridge and this can lead to the fracture of the bridge at its ends. Hence, it might be useful to have the bridge along the <110> direction and the bridge body misaligned in respect to it. (Fig.22).

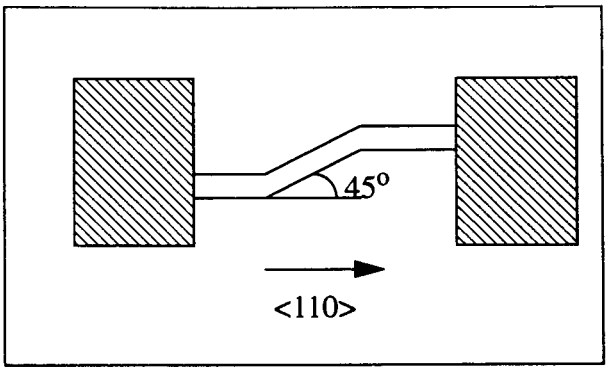

Fig.22. Si bridge alignment.

For bridges made out of SiO_2, the thermal stress adds to the residual stresses. Thermal stresses are a result of the mismatch between thermal expansion coefficients of bridge's materials. The linear coefficients of thermal expansion, $(\Delta L)/(L\Delta T)$, for Si and SiO_2 are $4.2 \cdot 10^{-6}$ and $3.2 \cdot 10^{-6}$, respectively (thin films). Thus residual compressive stresses would exist. The SiO_2 bridges will bend. While a high temperature annealing, $T > 700°C$, of the deposited film would release the residual stresses, the SiO_2 thermal stresses are released only by using stress relaxation structures.

A compressive residual stress in excess of:

$$\sigma = \frac{\pi^2 t^2 E}{12L^2} \tag{118}$$

will bend the structure. For long and thin bridges σ values are small, in the mP_a range. Thin, long bridges will bend easier.

Stray stresses' influence mostly affect the structural integrity of the micromechanical sensors. Unlike them, stain stresses influence the sensor behavior if the structural material of the electric resistance is a piezoresistive material. Mechanical stresses applied to the material change its bulk resistivity if volume changes exist (bending or torsion). Monocrystalline silicon has a high piezoresistivity. The semiconductor's gage factor:

$$G = \frac{\Delta R}{R}\frac{1}{\varepsilon} \tag{119}$$

where ε = applied strain and $(\Delta R)/R$ = fractional change in resistance, is more than an order of magnitude higher than that of metals.

The two sources of stray stresses, thermal and residual stresses, and their effects on micromachined sensors were considered. The influence of the applied strain stresses on device behavior was also outlined. It can be concluded that it is desirable to control/reduce the stray stresses by using an adequate processing scheme and also that possible induced vibrations of the suspended bridges may influence the sensor output.

3.2. Process Design.

The suspended bridges were made of silicon and polysilicon, respectively. The main frame for device fabrication was:

- use a minimum number of masks;
- get a good electrical and thermal isolation;
- use of anisotropic etching for bridge release;
- use of local facilities;
- use of Si/SiO_2/polySi layered wafers for fabrication of polySi bridges with oxide substrate.

3.2.1. Silicon Bridges

Heavily boron doped diffused layers in n-type <100> Si substrate were chosen to build tiny suspended silicon bridges. The diffusion depth was set to approx. $2.5\mu m$ so that a final bridge thickness of approx. $2\mu m$ was obtained. The diffused resistance values are given in Table 15.

Table 15: Diffused resistance values vs. geometry.

$L\,[\mu m]$	R [kΩ]							
	w = 3μm	5μm	μm9	16μm	25μm	50μm	100μm	200μm
300	2.7 - 3.5	1.5 - 1.8	0.8- 1.1	0.5 - 0.65	0.8	0.5	0.25	0.12- 0.13

The average boron concentration was $C = 7 \cdot 10^{20} cm^{-3}$. The diffused bridges were then enclosed in rectangular openings to silicon (Fig.23a). The open areas were subsequently exposed to anisotropic etching. An illustration of etching apparatus is given in Fig.24 for EDP and in Fig.25 for hydrazine.

Heavily boron-doped layers act as an etch stop for $C > 7 \cdot 10^{19} cm^{-3}$ in EDP and $C > 7 \cdot 10^{20} cm^{-3}$ in hydrazine, respectively. As a result, the undoped silicon is etched away leaving suspended bridges made out of heavily boron doped layers (Fig.23b). Typical etch rates of Si <100> in EDP with no pyrazine added are $0.8\mu m/min$ at $95°C$ and $1\mu m/min$ in hydrazine at $95°C$. The etch rates are temperature dependent, following an Arrhenius law with the etching activation energy, E_a, as the exponential factor:

$$R = R_o exp(-\frac{E_a}{kT}) \qquad (120)$$

The etch rate increases as temperature increases. In EDP at $115°C$, the etch rate increases to

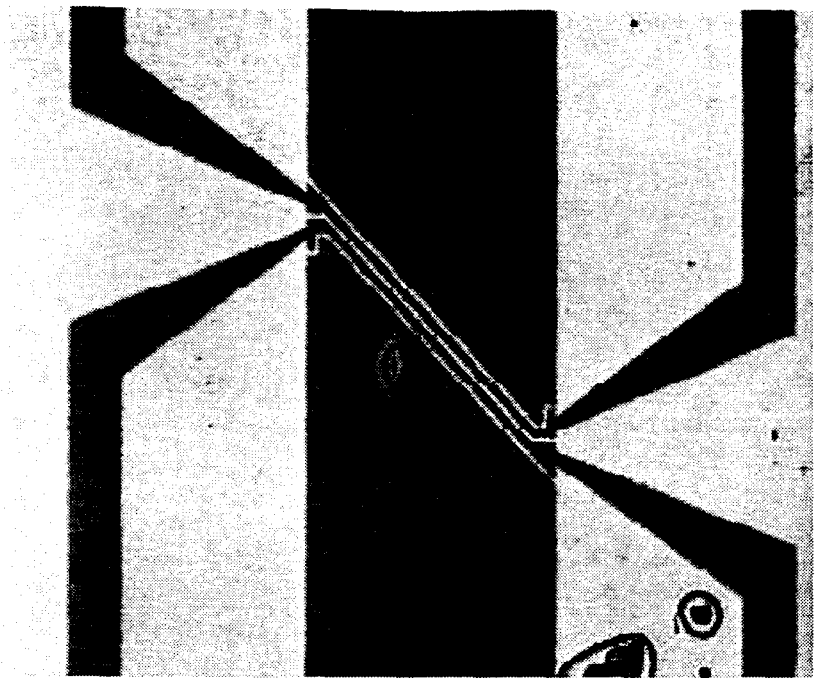

Fig.23a. Si bridge device before anisotropic etching

$1.25 \mu m/min$. The anisotropy ratio changes with temperature too.

For hydrazine, the etch rate at $100°C$ is $1.5 \mu m/min$. The hydrazine anisotropy ratio, Si(100)/ Si(111), is 10:1. An illustration of etching apparatus is given in Fig.24 for EDP and in Fig.25 for hydrazine.

During the EDP etching the contact areas are covered with metals resistant to EDP. Among the metals resistant to EDP there are Au, Cu, Ag and Cr. A sandwich of Al/Ni was deposited using sputtering deposition. The metals were patterned by using lift-off technique. Ni proved to be resistant to EDP attack. It seems that its resistance to EDP is due to the Ni surface oxidation.

Once the bridges are released, the chip is wire bonded, packaged and then is ready for characterization. A process flow chart for Si bridges fabrication is given in Fig.27. The process flow is:

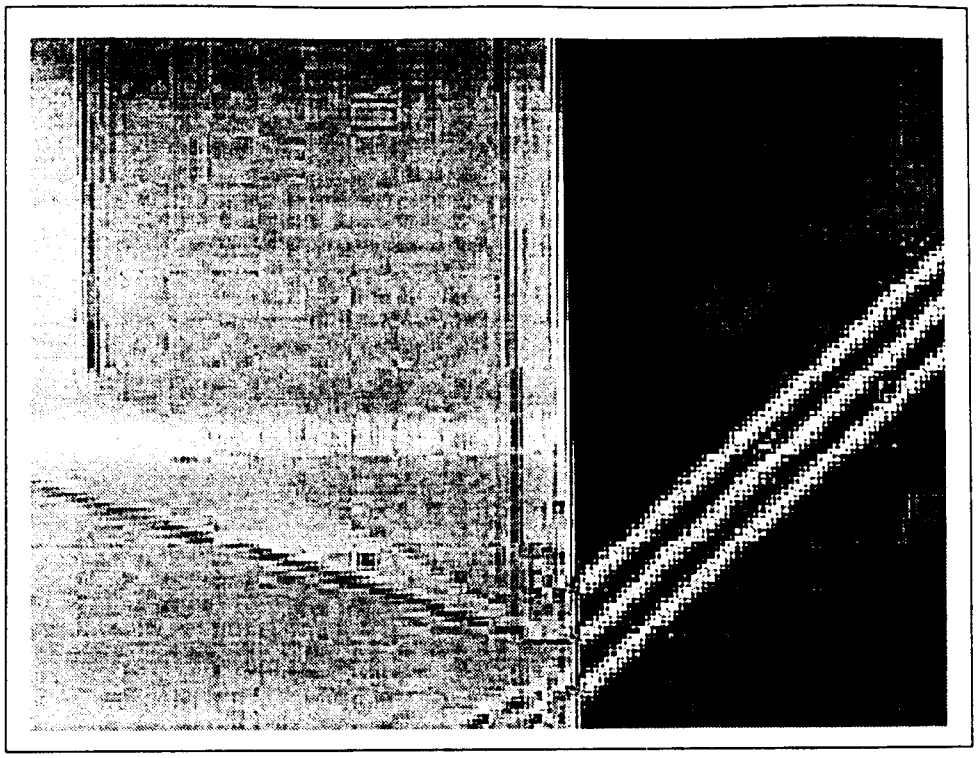

Fig.23b. Si bridge device after anisotropic etching

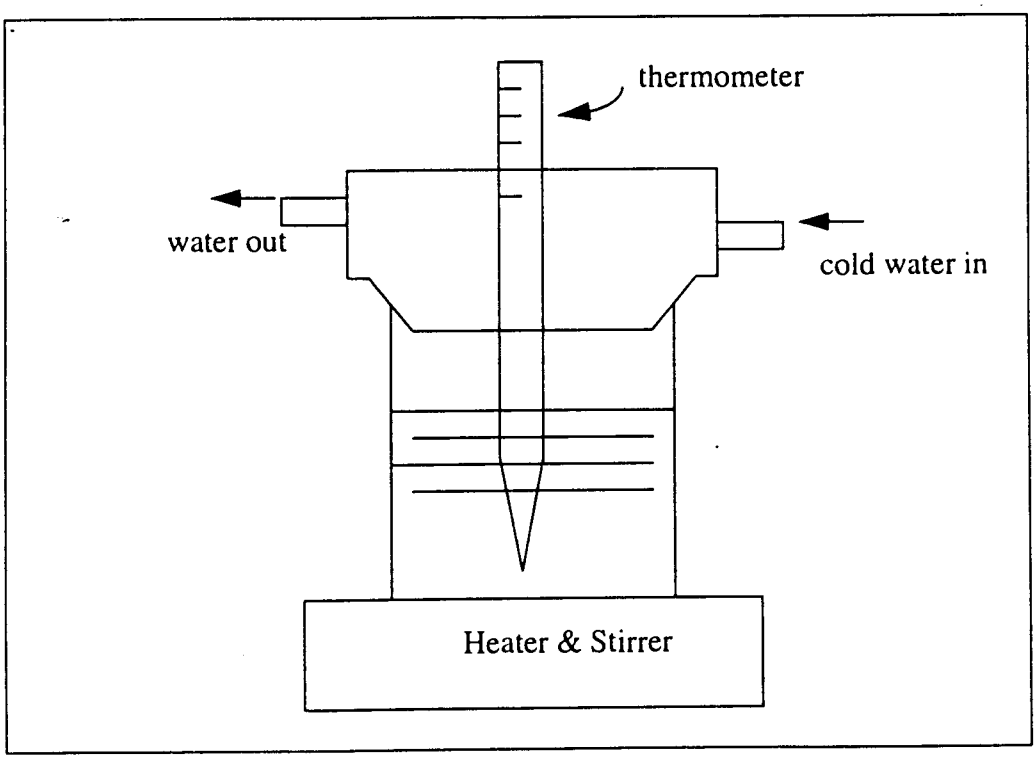

Fig.24. Illustration of EDP etching apparatus.

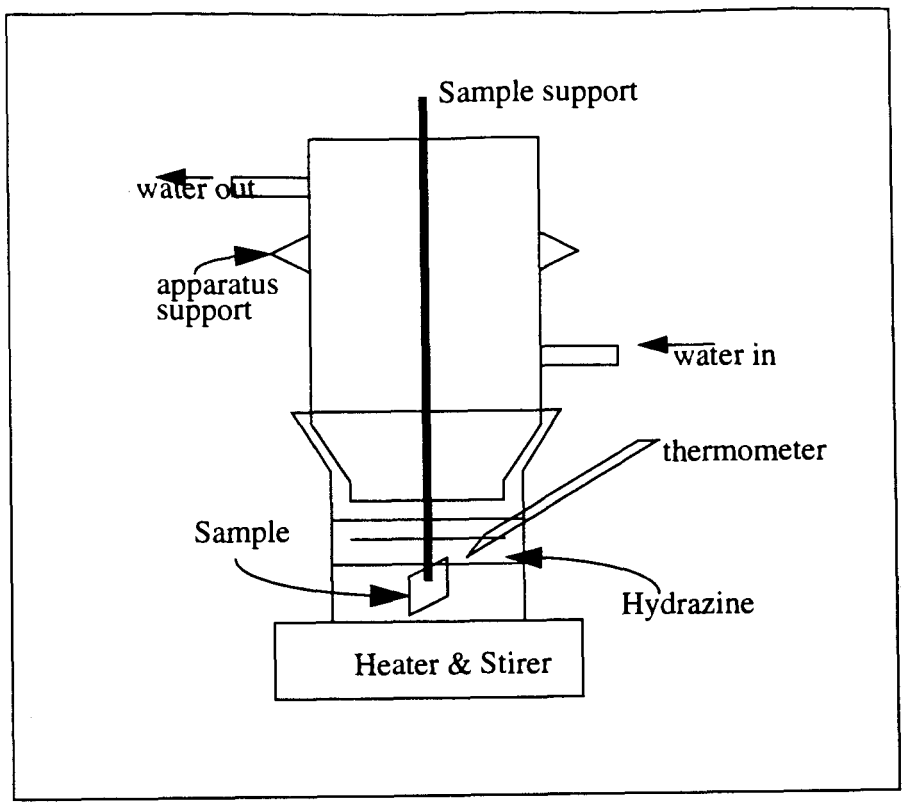

Fig.25 Illustration of hydrazine etching apparatus.

1. RCA cleaning.
2. thermal oxidation.

   process: 1100°C, 10min O_2+120min wet O_2+20min N_2;

   ramping rate: $15°C/(min)$; $T_{ramp} = 750°C$.
3. mask 1 patterning: bridges definition.

   a. PR spin-on: RPM=4000; t=40sec.

   b. soft-bake: 30sec./100°C.

   c. exposure: P=30mW; λ=314nm; t=18sec.; UV.

   d. developing: 8-10sec.; MF319 developer.

   e. hard-bake: 45min/110°C.

f. SiO_2 etching: 6-7min., B.O.E. etchant at room temp.

g. PR removal: rinse in acetone.

4. RCA cleaning.

5. B deposition from BN source.

process: $1100°C$: 40min/N_2

ramping rate: Fig.2t

6. B drive in.

process: $1100°C$: 5min. O_2+30min. wet;

ramping rate: $13°C$/min.; $T_{ramp} = 750°C$.

7. mask 2 patterning: open contact area.

process: same as in 2 except that the PR layer is not removed after SiO_2 etching;

SiO_2 etch time=4min.

8. With PR, wafer cleaning for metal sputtering deposition.

etchant: HF/Di (1:10) volumetric ratio; room temp.; time=10-15sec.

9. Al/Ni sputtering deposition.

10. Al/Ni patterning by lift-off technique.

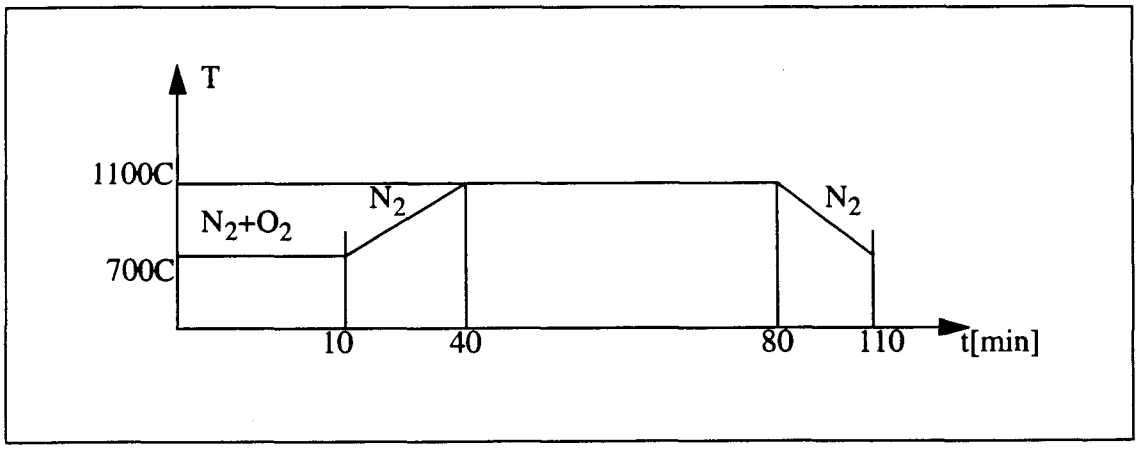

Fig.26. Temperature profile during B deposition process.

1) Oxidation

T=1100 C;
10min O_2/ 120min wet O_2/ 20min N_2

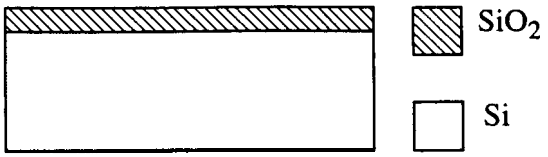

2) Opening of windows for B deposition

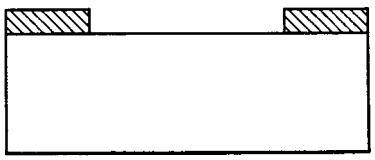

3) B deposition and drive-in

Deposition:
T=1100 C; t=45min

Drive-in:
T=1100 C; 5min O_2/ 25min wet O_2

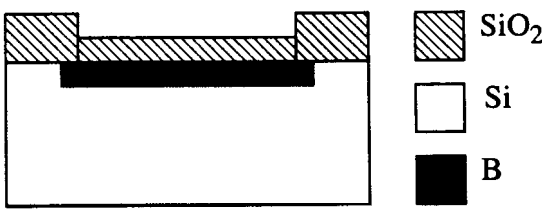

4) Contact windows opening

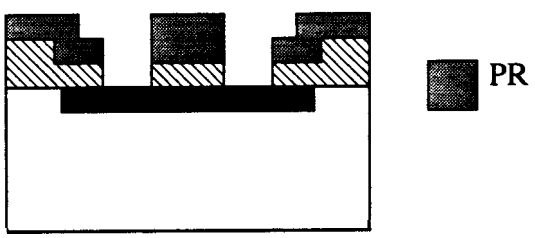

5) Al / Ni deposition

Metal deposition by sputtering

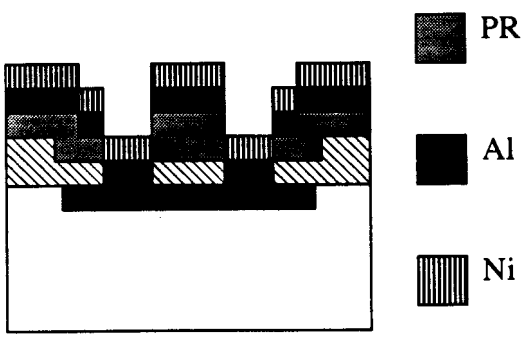

6) Metal patterning by lift-off technique

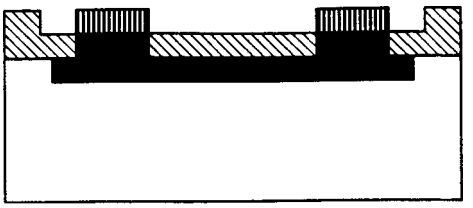

7) Window opening to Si

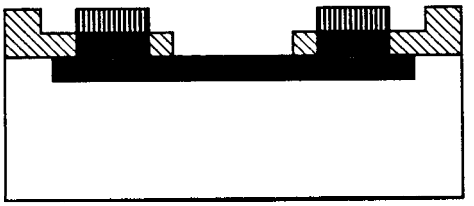

8) Si anisotropic etching in EOP

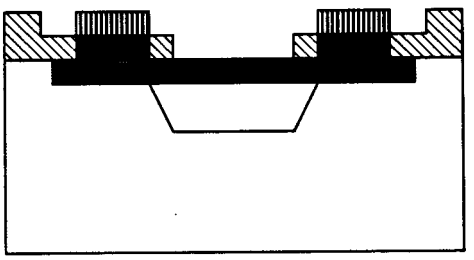

Fig.27. Process flow chart for Si bridge device

11. mask3 patterning: opening to Si substrate.

    process: same as in 2

    SiO_2 etch time = 7min.

12. Si anisotropic etching in EDP

    temp.: 95°C

    time: function of bridge geometry

3.2.2. PolySi Bridges

The starting wafers are 100mm, n-type Si(100) having a thermally grown SiO_2 layer of 0.8μm thickness and a LPCVD undoped polySi layer of 0.8μm thickness on top. PolySi layer is uniformly doped using BN diffusion source. Thermal oxidation of the poly layer is carried out in order to facilitate the polySi patterning by wet chemical etching. Thermally grown SiO_2 layer provides also a very good adhesion PR/polySi.

A second thermal oxidation is carried out in order to encapsulate the polySi resistor in SiO_2. The second photolithographic step defines the contact windows to polySi resistors. An Al layer thicker than 0.5μm is sputtered onto the wafer if hydrazine is used in the last step. For EDP etching, after contact areas opening, a seed layer Al(0.15μ)/Ni(0.3μ) is deposited by sputtering all over the wafer surface. The next step is to cover the wafer with a PR layer and to pattern it (again) with the contact window mask of the device. The seed layer is now exposed only in the contact areas, whereas in all the other regions is protected/covered with/by photoresist.

A gold layer of thickness 1.2μm is built up in the contact area by electrochemical deposition. Once the gold electroplating is done, the PR layer and the seed layer in the exposed areas are removed. The structure at this point consists of a polySi resistor embedded in SiO_2, having its contact areas covered by a thick layer of gold. Then the openings to the Si substrate are patterned. The final step toward getting suspended bridges is the substrate anisotropic etching in EDP or hydrazine. The chips are packaged and wire bonded before EDP/hydrazine etching. This prevents bridge fracture by reducing the handling of the chip. A picture of the final device is given in Fig.29.

A process flow chart is given in Fig.28. The process flow is:

1. RCA cleaning.
2. thermal oxidation: $1100°C$.

   process: 10min. O_2+120min. wet+20min. N_2;

   ramping rate: $13°C$/min.; $T_{ramp} = 750°C$.
3. mask 1 patterning: polySi bridges definition.

   RPM=4000;

   exposure time=30sesc.;

   soft-bake: $100°C$, 30sec.;

   exposure time: 18sec.;

   developing time: 8-10sec.;

   hard-bake: $120°C$, 45min.;

   etching time: 6-7min.;

   PR removal.
4. polySi thermal oxidation: $1100°C$.

   process: 10min. O_2+20min. wet;

   ramping rate: $15°C$/min.; $T_{ramp} = 750°C$;
5. RCA cleaning.
6. mask 2 patterning: contact windows opening.

   same process as for step 3. except that there is no PR removal after SiO_2 etching from contact area.
7. Al sputtering deposition.

   DC sputtering deposition
8. Al patterning by lift-off technique.
9. Si anisotropic etching in hydrazine

   temp.: 110^oC

   time: function of bridge geometry.

1) Starting wafer

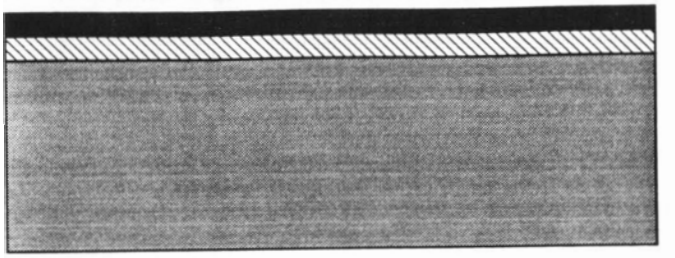

Si

SiO_2

PolySi

2) PolySi uniform doping and oxidation

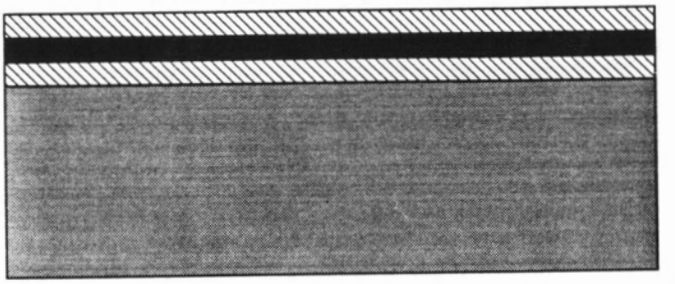

3) PolySi patterning

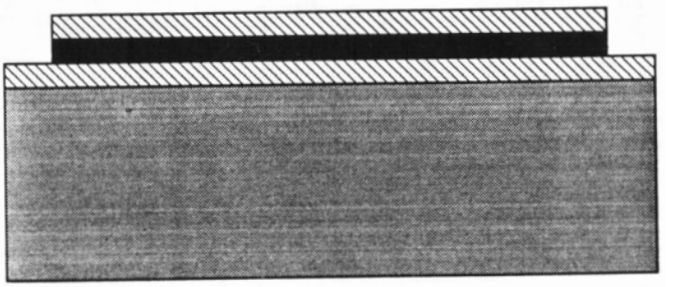

4) PolySi oxidation

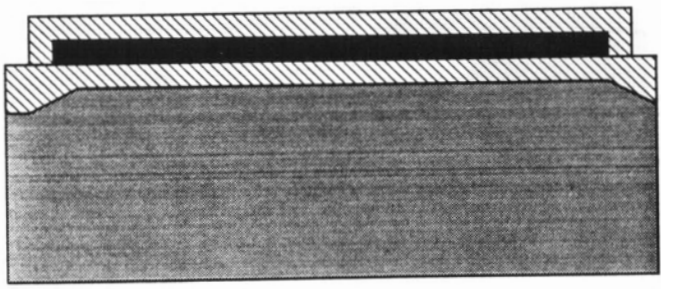

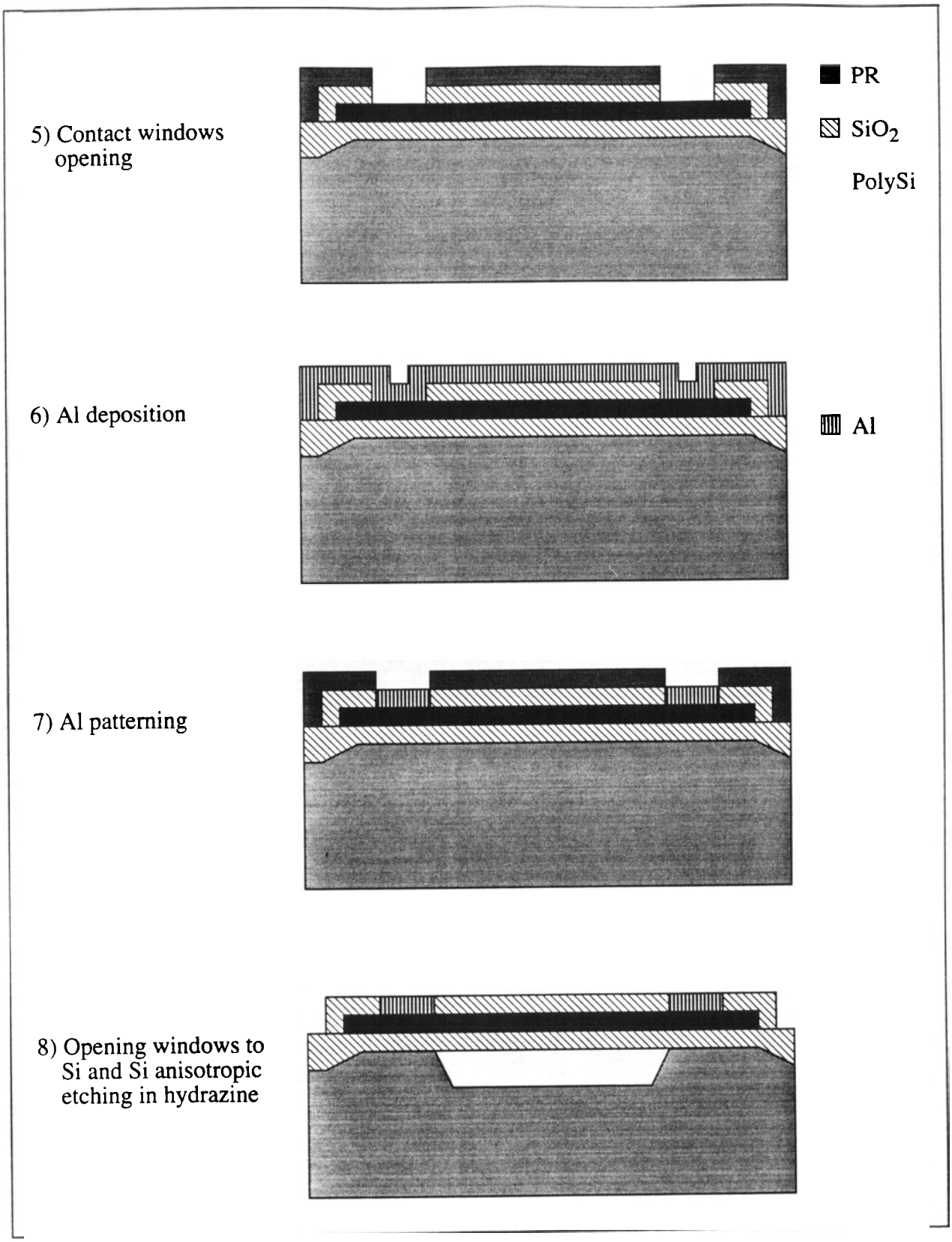

Fig28. Process flow chart for polySi bridges device

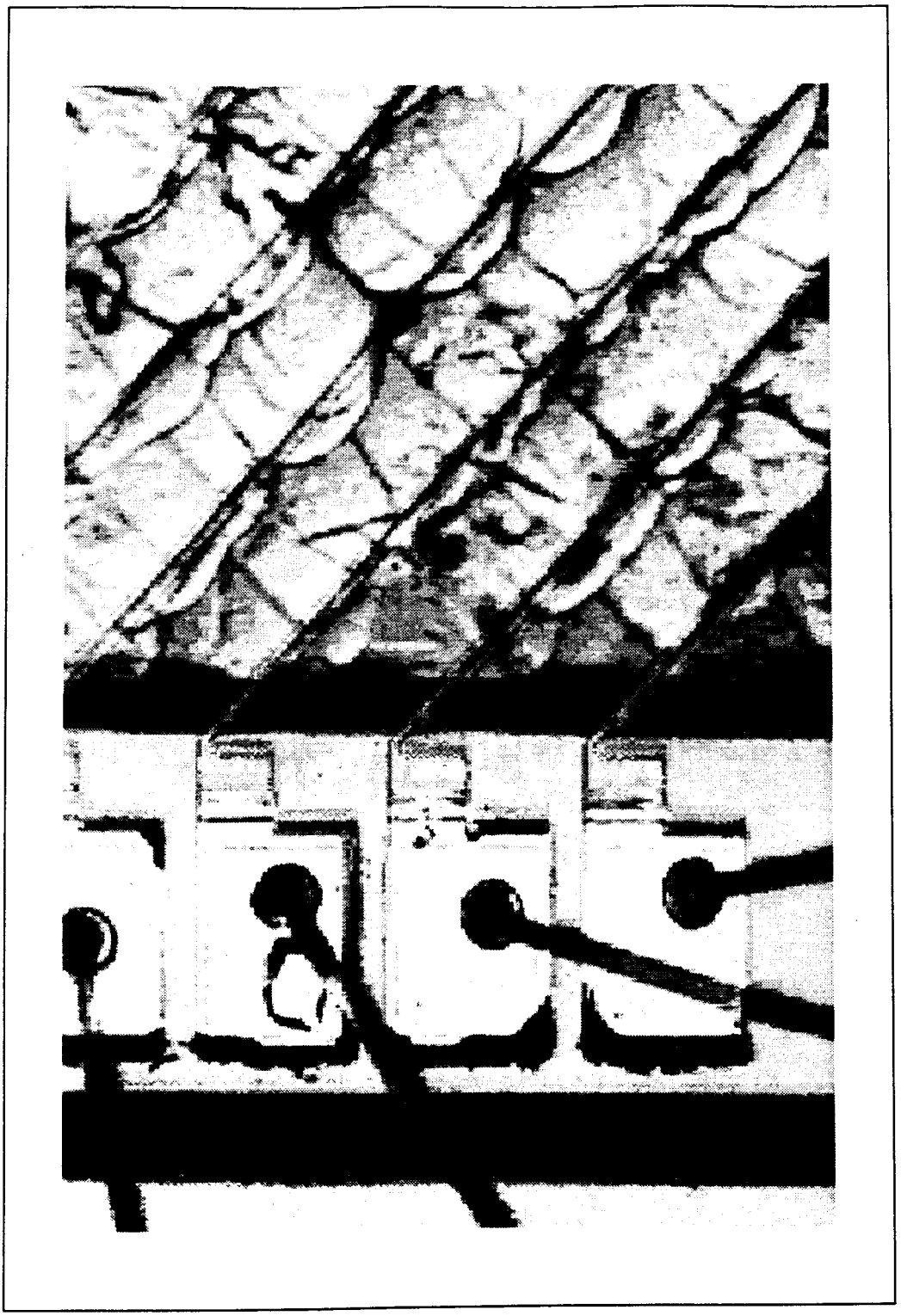

Fig.29 PolySi bridges device. Design1

The underlying supporting SiO_2 layer has very good electrical and thermal insulator properties. Its electrical resistivity is high, $10^{12}(\Omega \cdot cm)$, and the thermal conductivity is $1.4 \cdot 10^{-2} W/(m \cdot {}^{o}K)$, thus it is one hundred times lower than that of polySi.

3.3. Layout Design

The characteristics and precision of the device are influenced not only by the building materials but also by the device geometry/structure. Good mechanical properties of constituent materials lead to good device yields and reproductive characteristics. The accuracy and reproducibility of the sensors is also determined by the precision and uniformity of the machining process across the sample. The ability to get the desired microminiature structure relies on the ability to use the anisotropic etching rules. The layout design considerations regarding bridge release are first presented. Then the device physical dimensions are evaluated based on the modeling and structural analysis results. The number of masking steps is determined by the fabrication scheme.

3.3.1. Machining Process Rules

Any rectangular opening windows to Si(100) substrate, with its edges oriented along <110> crystallographic direction, will generate a pit, a square pyramidal downward grove, when exposed to an anisotropic etchant. If a geometry other than a square is defined, then the resulting cavity will take the shape of the smallest rectangle which can enclose the vertices of the defined geometry (Fig.29). This is the smallest enclosing rectangle rule.

For any deviation, misalignment of patterned opening windows to Si from horizontal or vertical <110> direction, the resulting cavity will be the smallest rectangle with its edges along <110>

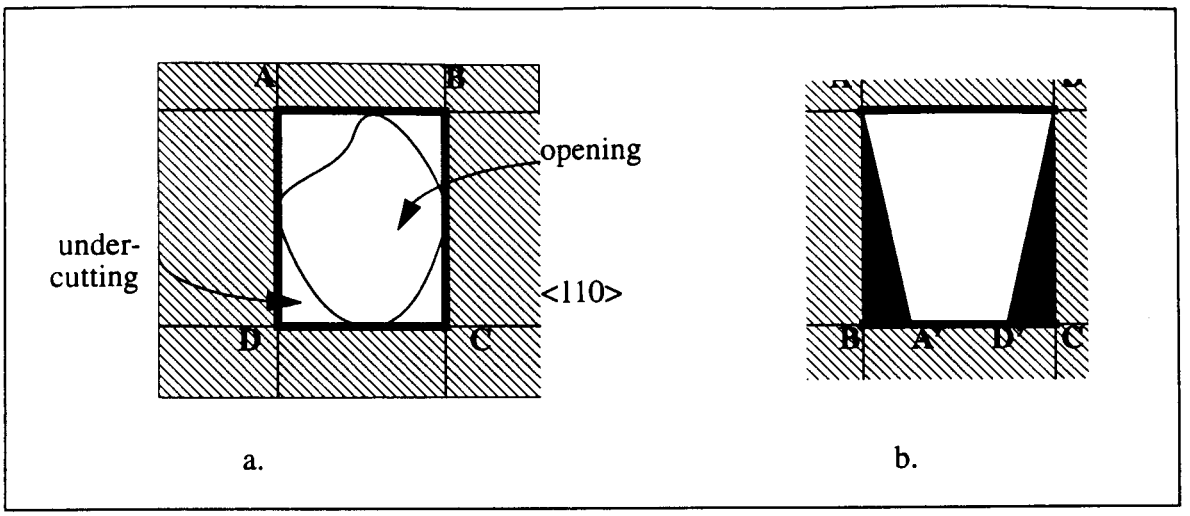

Fig30. The smallest enclosing rectangle rule: a. arbitrary shape: b. misaligned rectangle.

direction, which can enclose the vertices of the defined geometry (Fig.30). The anisotropic etchants property to undercut misaligned edges is used to create free-standing structures.

If two misaligned open areas are defined in close proximity in such a way that the individual enclosing rectangles cavities intersect or touch, then the resulting cavity will be the merged rectangle (Fig.31).

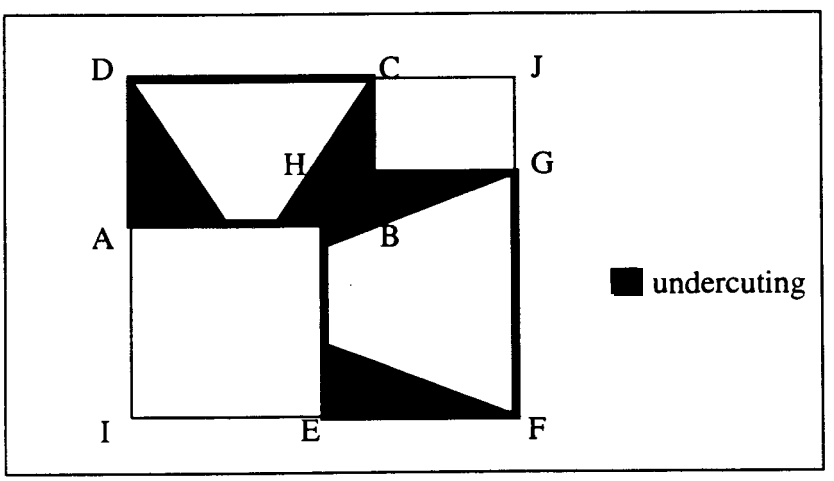

Fig.31. Intersection of the enclosing rectangles rule.

After sufficient etching time, the resulting cavity will be in the shape of the rectangle which encloses all the vertices of each individual intersecting rectangle. This is the intersection of enclosing rectangles rule.

The above rules were used in the layout design of the device. The design consists of parallel, equally separated bridge strips at 45 degrees with respect to the <110> crystallographic direction (Fig.32). The misalignment of 45 degrees in respect with the flat corresponds to the fastest undercutting etch rate. The undercut etch rate is approximately equal to 1/3 of the <100> etch rate in the opening sides. Both silicon and polySi bridges lying on SiO_2 were fabricated using this design approach. The structures present the disadvantage of misalignment in respect with the applied acceleration, if the acceleration is oriented along the device package sides (Fig.33).

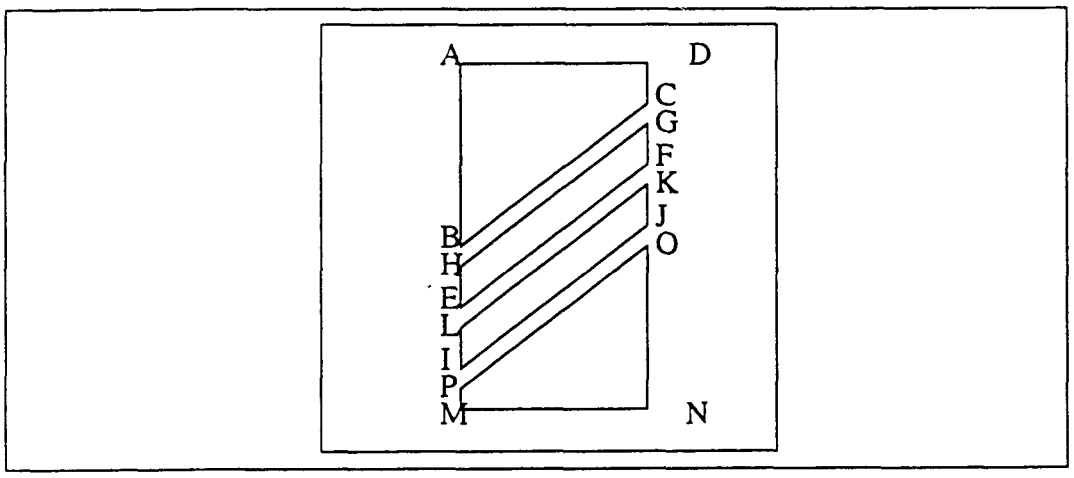

Fig.32. Oblique bridges. Design 1.

To correct for this, a platform like approach was used to generate bridges oriented in parallel with the wafer flat (Fig.34). In this design, the misaligned edges AB, CD, EF, GH are used to create a free-standing platform, AHIJ.

There are two layout techniques for creating free-standing platforms: Manhattan design and Polygon design (Fig.35).

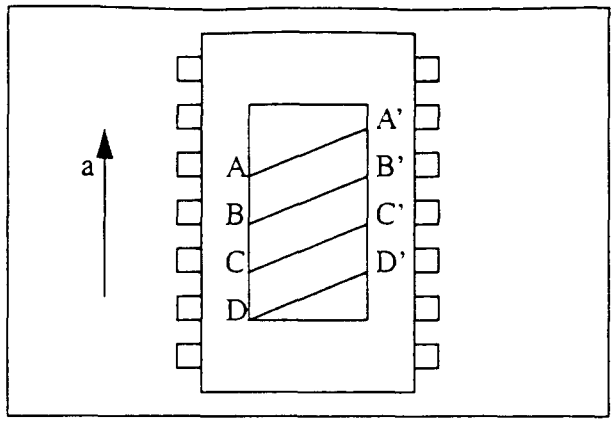

Fig.33. Misalignment of applied acceleration in respect with oblique bridges.

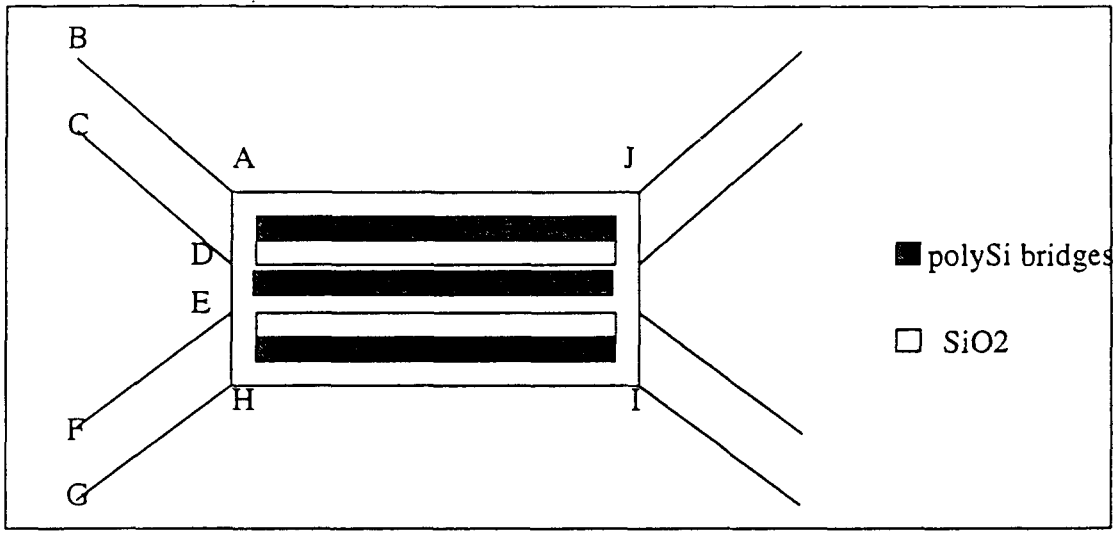

Fig.34. Parallel bridges. Design 2.

Manhattan layout uses small staggered steps arranged in a stair-case like manner. This technique has the advantage of fast undercutting due to the stair-case convex corners. Even with this advantage, it can't be used in designing free-standing structures experiencing thermal cycles. The thermal induced stress will be concentrated on all small sharp edges of the staggered steps, which could lead to mechanical failure.

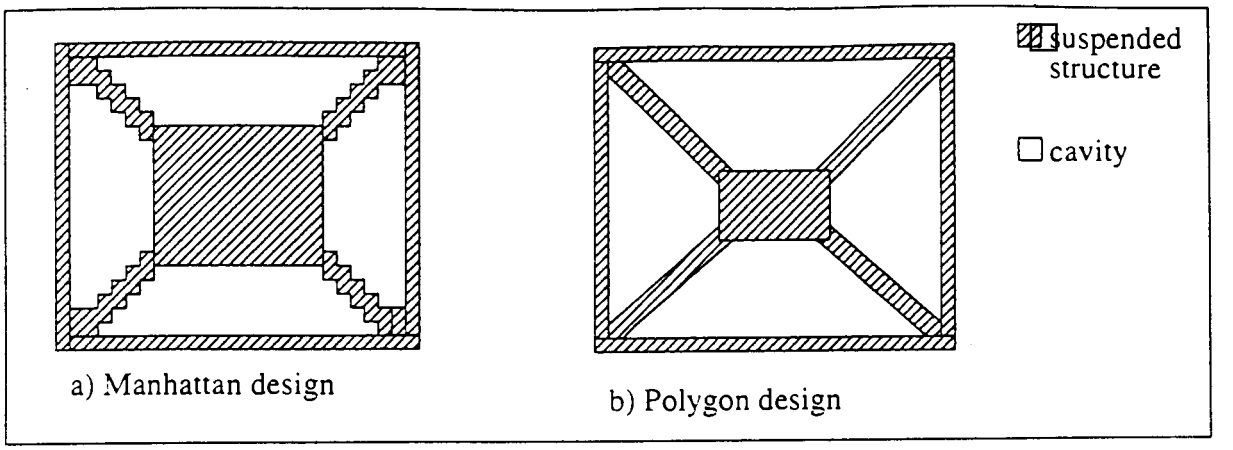

Fig.35. Manhattan and Polygon designs.

The polygon layout creates smooth misaligned edges with all the edges formed by the polygon obtuse. It eliminates the concentration stress points. The disadvantage is a slower undercutting rate.

Twelve successive, equally spaced, suspended polySi bridges were fabricated using this layout technique. The drawbacks are a very long etching time, 12-14 hours in EDP at $95°C$ and the resulting fragile sustaining arms. A limitation to only one symmetrical pair of sensors beside a heater would reduce the platform size, thus the corresponding etch time. An enlargement of the sustaining arms would also reduce the fracture risk. The total thickness of SiO_2/polySi/SiO_2 sandwiched structure was $\sim 1.5\mu m$ below the thumb rule limit of $2\mu m$. The beams are stronger but still fragile. Initial thermally grown oxide thickness was $0.5\mu m$, thus it might be necessary to increase it to $1\mu m$, for a starting deposited polySi layer of $0.8\mu m$ on top of it.

3.3.2. Device Design

Thermal sensing elements for integrated devices with potential high thermal isolation from the

substrate are the boron heavily-doped resistors, polySi resistors embedded in SiO_2, metal/polySi thermopiles and metal resistors. Among them, the thermopiles are the only self-generating sensing elements. The other ones are modulated sensors, as they require power supply. A thermopile based device was designed in BiMOS technology. After post-processing and packaging, the device was fully characterized. It worked well as a very sensitive flow-meter, but 1g acceleration could not be measured. The gain of the amplifier circuit was one thousand and the heater voltage supply ranged from 1 to 5V. The heater electrical resistance was $1k\Omega$. A Seeback coefficient for Al/polySi thermopile of around $60\,(\mu V)/(^{\circ}C)$ was measured. This approach will not be presented here. Sensors made out of diffused resistors, polySi resistors and metal resistors were fully characterized also.

3.3.2a. Layout Design of Device with Si Resistors

Theoretical analysis and simulations were carried out for Si/polySi resistors based devices. The device elements, heater and sensors, might be regarded as long electrical wires at rest in air if the following dimensional requirements are met:

1) minimum wire length, L, so that $mL = \sqrt{\frac{hD}{kA}L^2} \gg 5$ in order to neglect end effects.

   Here $mL = mL(T)$ where T=wire temperature.

   For $T \geq 100^{\circ}C$ above ambient, $L_C = 1\mu m$, the convective heat transfer coefficient h>10000, so that the min. wire length is $600\mu m$. If this criterion is met then the temperature along the wire can be considered constant.

2) sensor characteristic dimension, $L_C < 10\mu m$, so that for any applied acceleration in the range (0.001-10)g and practical temp. values, the conduction path from the sensor to the substrate is much higher than the thermal resistance of the surrounding air. Thus the sensor steady-state temperature will be that of the surrounding air, irrespective of its thermal mass.

3) small sensor thermal mass is also needed in order to get faster response time. the time constant

$\tau = \frac{\rho V C_p}{h A_S}$ is directly proportional to its characteristic dimension $L_C = 4\ V/A$, density ρ

and specific heat c_p . This means small V/A for a given material. It is assumed that h is constant for the temperature change range at detector surface, A.

4) low t/L values will determine low natural resonant frequencies of the beam.

$f_n = \sqrt{\frac{wt^3}{wt^2 L}} = \sqrt{\frac{t}{L}}$ for a given material.

Thus the bridge electrical resistance model of long, isothermal electrical wire at rest, suspended in air, holds for:

i) bridge characteristic dimension < $10\mu m$.

ii) bridge length > $600\mu m$.

From transient analysis, the time for the detector to reach the surrounding air temperature is proportional to the detector radius r_d. Hence, the smaller the radius, the faster the detector. The technological limit is 2 to $3\mu m$ wire width. This corresponds to a maximum bridge length of $300\mu m$.

The corresponding aspect ratio is (100-150):1. For B heavily doped layers of $C_B \sim 10^{20} cm^{-3}$ and sheet resistance $R_S = 5 - 10\Omega/(sq)$, the resulting electrical resistance value is $\sim 1k\Omega$. The detectors are placed in a Wheatstone bridge configuration. Since $R \sim 1k\Omega$, the Wheatstone bridge voltage supply can be in 1V range, which corresponds to an increased sensitivity and resolution of the device. The higher the detector electrical resistance, the higher is the sensitivity. The voltages across the detectors are limited by the pn junction breakdown voltage and by the self-heating effect.

In order to increase the device sensitivity, the temperature gradient at the detectors' location should be optimized, following the device stated principle. Since $grad(T) \sim 1/r$, r = heater-detector separation, the closer is the detector to the heater, the higher is the temperature gradient.

Hence

4) the smallest heater-detector separation is set by the technological limit at $3\mu m$ for $L = 300\mu m$.

5) in order to have free space like conditions, the lateral extension of the device has to be as large as possible.

6) from processing considerations the bridge direction is tilted 45 degrees

Based on the above considerations (1 to 6), a layout with two masking process for silicon suspended bridges was generated as in Fig.35.

The first mask defines the open areas to Si for boron doping. The bridges and contact areas are formed. The second mask opens windows to Si substrate underneath the bridges and also to contact areas.

There are four different bridge width/separations: 3/5, 5/6, 8/9,and 16/6μm, respectively. The bridge length is 300μm. The cavity size is 0.4mm wide, 4mm length and 200μm depth. The space above the bridges is either the package high or open air. Bare, suspended Si bridges are created.

The drawback of this design is that the pn junction is exposed to the environment after the anisotropic Si etching. The structures usually suffer from high leakage currents, which might also be due to the defects induced by heavily doping. The advantages are the lack of thermal stresses

which are added for composite layers. The Si mechanical properties made the structures very robust. The minimum dimensions are given by the photolithographic process only. There are no minimum layout resolution / separation rules which for a composite structure would limit the minimum distance heater-detector. For monocrystalline Si, the temperature coefficient of the resistance is stable over a wide temperature range.

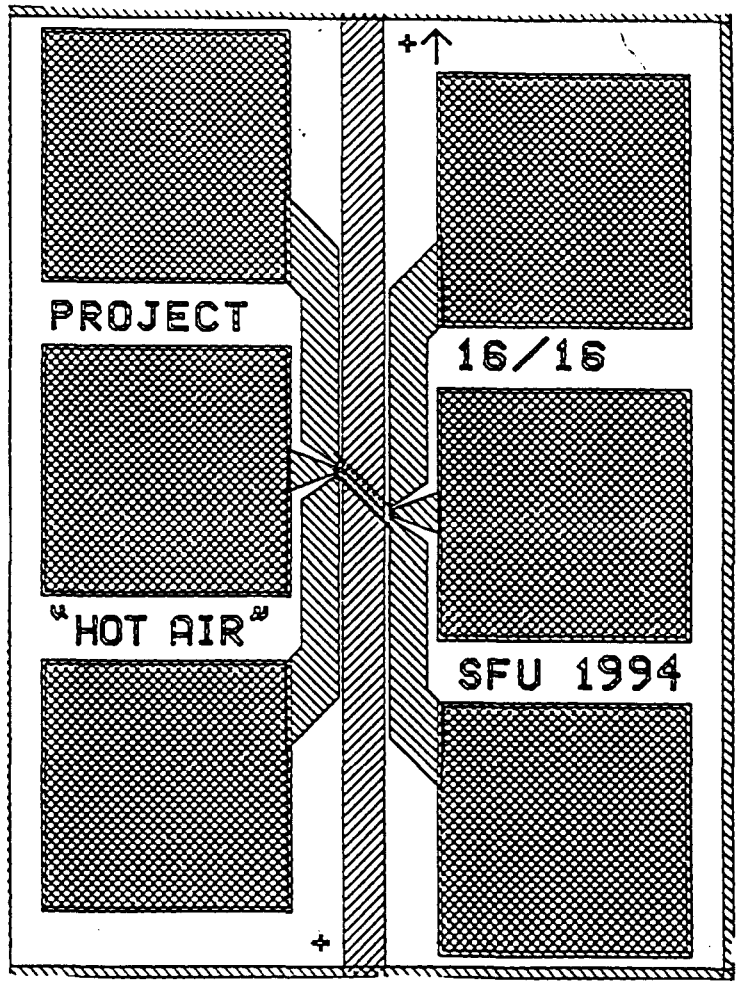

Fig.36. Layout for Si bridges based device. Design1.

3.3.2b. PolySi Resistor Layout Design.

PolySi resistor values can range from hundreds of ohms to megohms as a function of geometry and doping concentration. There are no electrical isolation problems. Hence the voltage supply value to a Wheatstone bridge incorporating the two detectors is limited only by the Joule effect. The temperature resolution of the device depends on detector's temperature coefficient of resistance. The temperature coefficient of polySi resistors increases as polySi doping concentration decreases [37]. It is constant over a limited temperature range, usually $T < 300°C$ above ambient.

It has been shown [4] that there is a threshold power density for the polySi resistor, $p_{th} = 5 \cdot 10^4 (W/m^2)$, which corresponds to maximum electric power through the resistor before permanent changes in R_S and TCR occur.

For cross section area $14\mu m \times 0.5\mu m = 7\mu m^2$, $P_{th} = 35mW$. The cross-section area and the doping level of polySi will determine the electrical resistance value. For a given characteristic dimension L_C = area/perimeter, there will be a minimum resistance length so that the ends effects can be neglected:

$$L_{eff} = L - 2X_m = L_C - 1200\mu m, L_C = 10\mu m, T = 100°C \quad \text{above ambient.}$$

According to the desired device structure and the corresponding fabrication scheme, there are minimum three masks needed. The first mask defines the polySi resistance. The width and the length of the polySi resistances are $14\mu m$ and $2000\mu m$, respectively. The second mask opens the contact areas to polySi resistors. The contact openings are also used as pads. The third mask opens windows to Si substrate underneath the polySi resistors. For the first design, Design1,the bridges are tilted 45degrees in respect with <110> crystallographic direction. Heater-detector separation is $175\mu m$. This corresponds to a location close to the outer side of the thermal boundary

layer for a heater enclosure characteristic ratio of 1000. The mask pattern is shown in Fig.37. In Design2 approach, the bridge direction is parallel to <110> crystallographic direction. Design2 uses polygon design rule. Device layout is given in Fig.38.

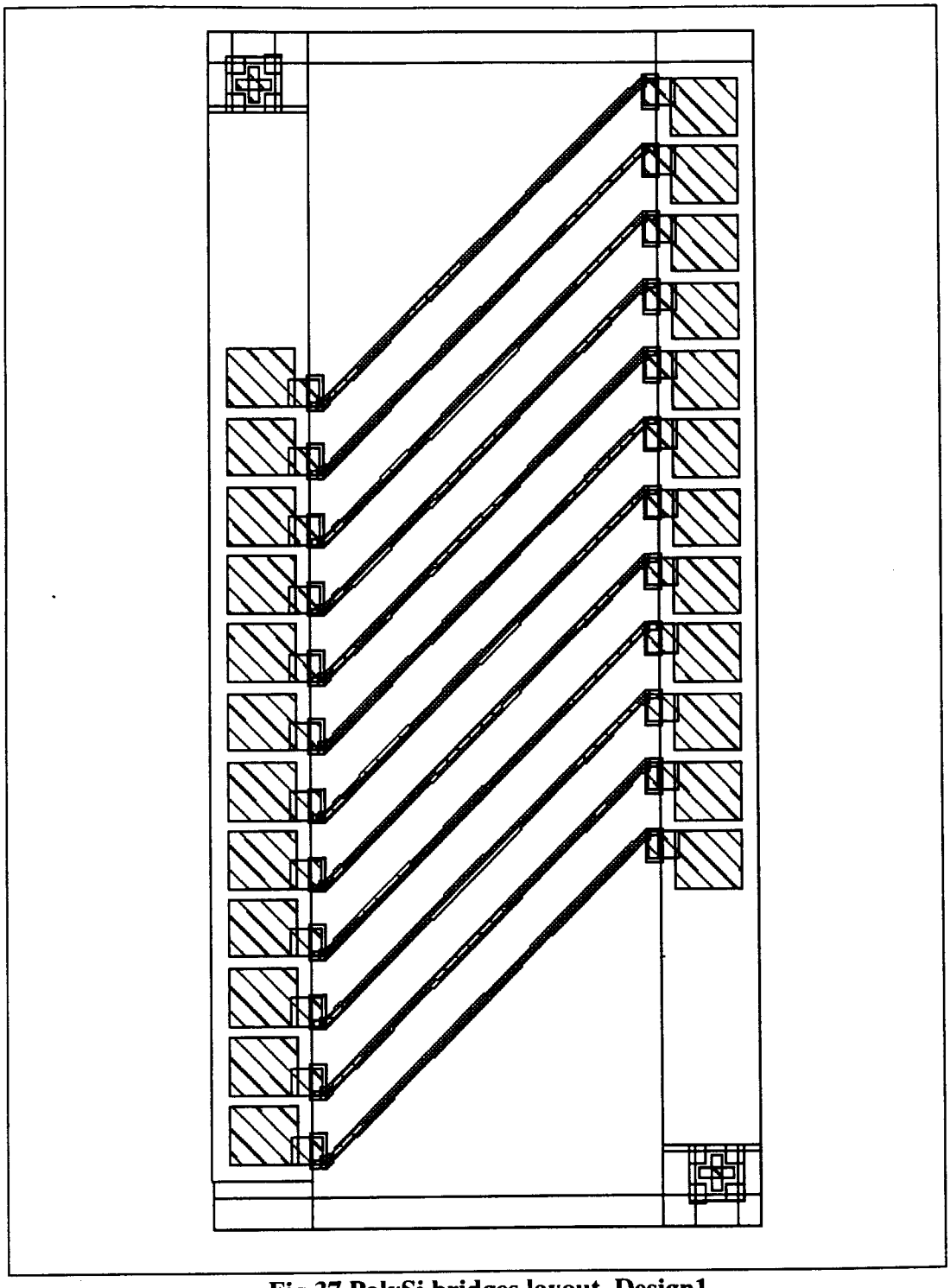

Fig.37.PolySi bridges layout. Design1

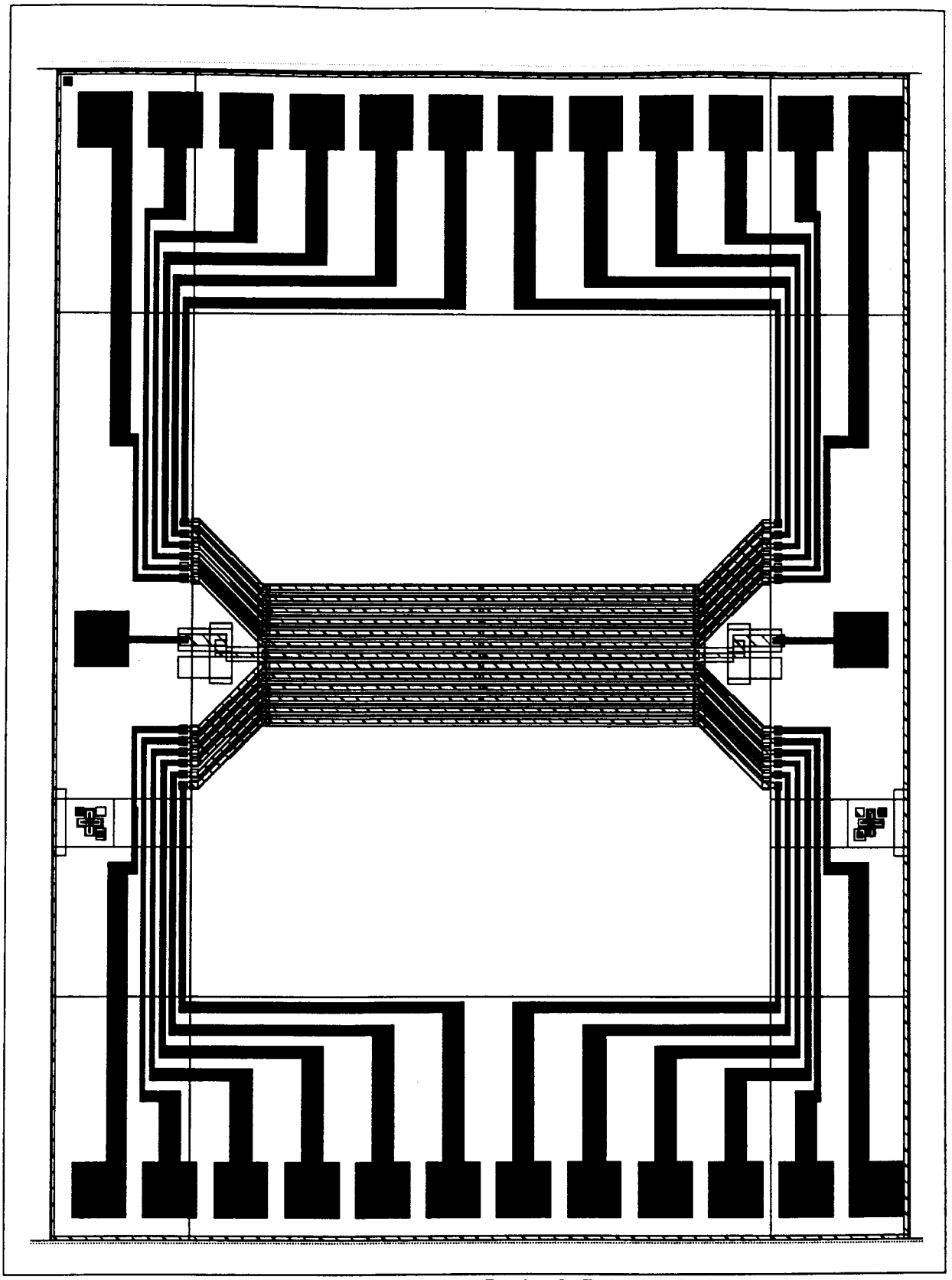

Fig.38 PolySi bridges layout. Design2 (Polygon design).

Chapter 4. Device Characterization.

Devices made out of silicon and polysilicon resistors were fabricated. The heater - sensor separation for devices with polySi resistor is 175μm, There is a 80 μm cavity depth beneath the bridges and about 1 cm high free space above them. The resistance values are 20 Kohm +/- 10%. The measured temperature coefficient of resistance is 5 x 10^{-4} / ^{o} C.

The Si bridges device has 5 and 8 μm, respectively, heater - sensor separation, 100 - 130 μm cavity depth beneath the bridges and 1 mm free space above them. The resistance values are 2.7 Kohm for 5 μm H - SNZ spacing and 1 Kohm for 8 μm H - SNZ spacing. The pn junction breakdown voltage was 15V at 10 μA. The measured TCR is 1.5 x 10^{-3} / ^{o} C +/- 3 x 10^{-5} / ^{o} C. The devices were measured using similar approaches.

The device has an analog output. The two temperature sensing elements are connected in a Wheatstone bridge configuration (Fig.39) operated at constant voltage, V_B. R1, R2 are external resistors. The external resistors are well matched in order to minimize the bridge offset.

The Wheatstone bridge converts the sensor's resistance change due to the differential heat transfer directly to a differential voltage signal, V_{out}. The relationship between the differential output voltage, V_{out}, of an ideally balanced bridge and the resistance change, dR, in response to an applied acceleration, a, is given by

$$V_{out} = [dR / R] \times V_B \qquad (124)$$

For the configuration given in Fig.39, the differential output voltage is independent of the absolute values of the resistors. It is determined by the relative resistance change, dR / R, and the bridge voltage supply, V_B.

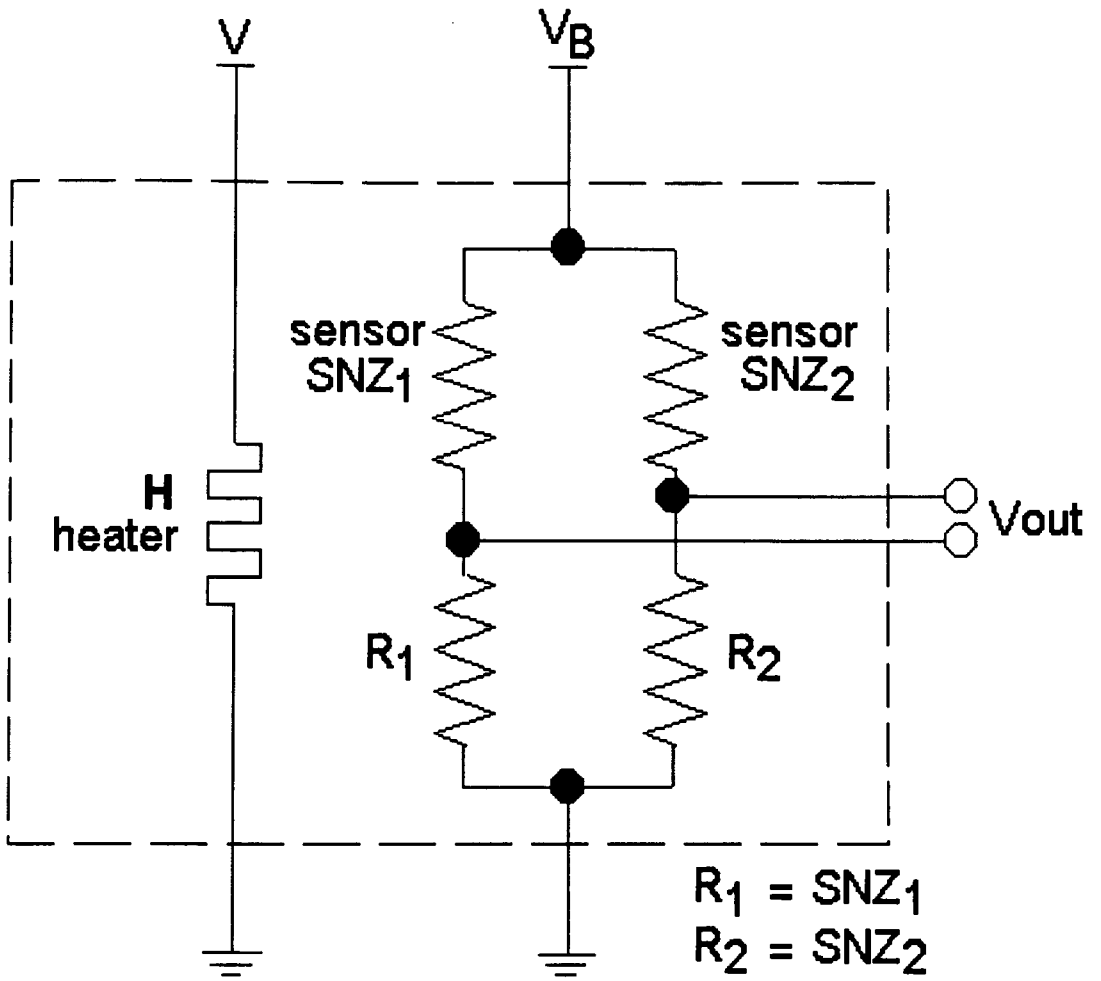

Fig.39 Wheatstone bridge configuration

The bridge output voltage is fed as input to an external instrumentation amplifier. The circuit schematic representation is given in Fig.40. The amplified signal is fed to an oscilloscope for visualization and measurements.

In order to evaluate the device's performances, the following device's characteristics were evaluated: sensitivity, linearity, resolution, frequency response and dynamic range.

4.1. Experimental Set-Up.

The principle of the testing method is to apply known accelerations to the device, which will be referred as reference acceleration, and to measure the corresponding device's response.

In order to apply known accelerations to the device under test, DUT, this and a reference accelerometer are placed on a mini vibration table, MINI SHAKER 4810. The maximum bare table acceleration peak is 71.4g. The performances of the vibration table are limited by the moving element's dynamic mass and by the mounting conditions. The vibration table will be referred to as exciter.

The reference accelerometer is a general purpose, standard piezoelectric accelerometer, Bruel & Kjer 4381, with a side mounted connector. Its voltage sensitivity is 0.994 mV / ms^{-2}. The reference accelerometer's frequency range is 0.1 Hz to 2 KHz for worst case mounting conditions. Its dynamic range goes from 0.1g to 50g.

The signal from the reference accelerometer is read by using a charge amplifier, Bruel & Kjer 2635, which allows the user to set up a frequency range, signal gain, sensitivity and measurand (i.e. displacement, speed or acceleration). The amplified signal from the reference accelerometer is visualized on oscilloscope. It can represents either displacement, speed or acceleration depending on user set-up (because the Bruel & Kjer 2635 type charge amplifier can also integrate the signal once or twice). A reference acceleration range from 0.1g to 10g was used for measurements. The experimental set-up is shown in Fig. 41.

A 50 MHz programmable waveform synthesizer generates a sine signal of known frequency and amplitude. This signal is fed as input to a stereo amplifier, PA 7220. The amplified signal drives the exciter. Thus the wave generator and the stereo amplifier make the exciter's driver.

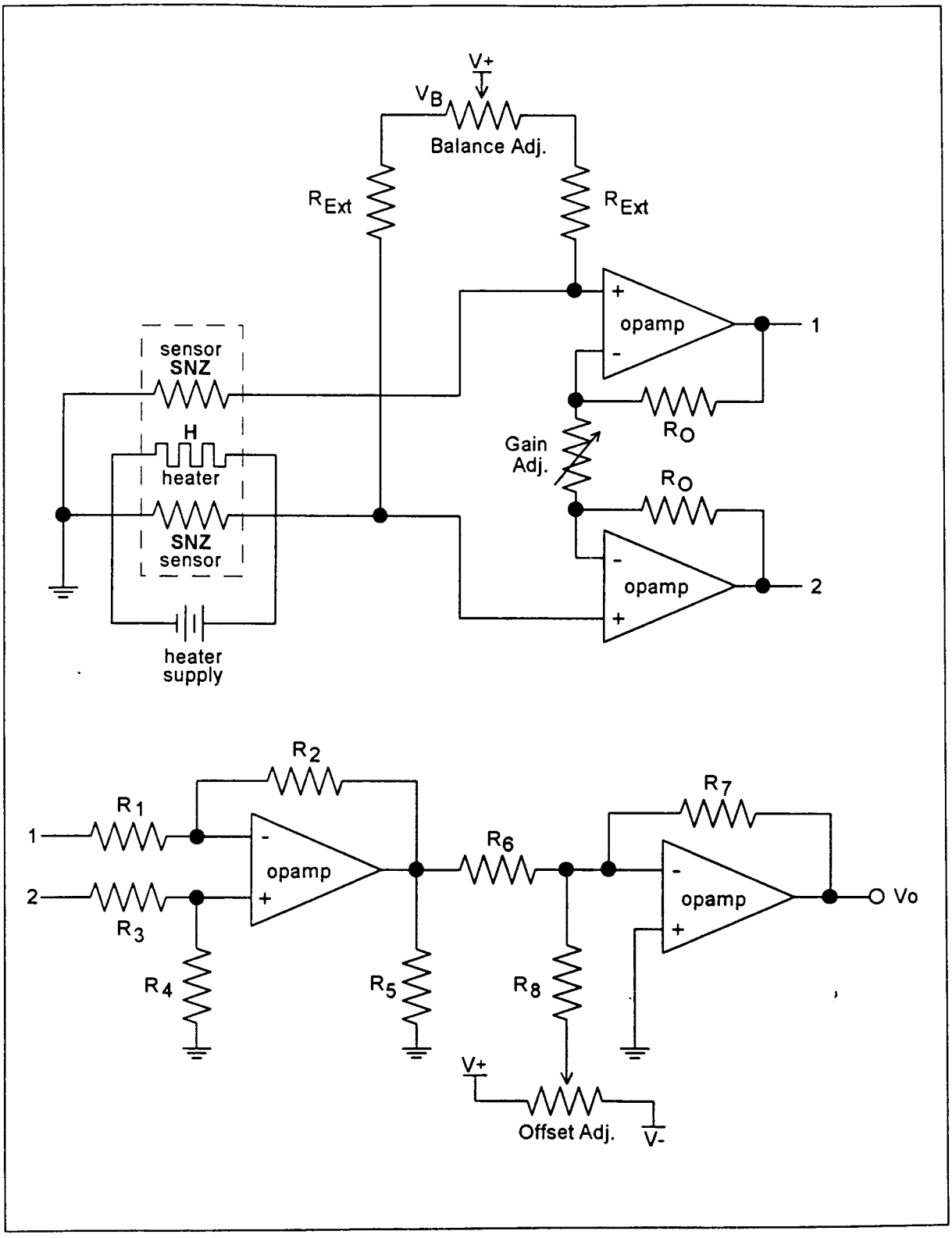

Fig.40 Schematic representation of the amplifier circuit

The amplitude of the sine driving signal will determine the physical displacement to either side of the table's rest position. Thus the form and period of the vibration remain the same whether it is the side displacement, velocity or acceleration that is being measured using the reference accelerometer. The main difference is a phase shift between the amplitude - time curves of x, v, a parameters [40].

The acceleration generated by the exciter (i.e. vibration table) is proportional to $A\omega^2$ for a sine drive signal. The generated acceleration has the same period with the drive signal. I determined experimentally that the reference accelerometer and the device under test, DUT, have also the same period with the drive signal.The measurement was done for frequencies up to 1KHz.

I have measured also the delay time of reference accelerometer in respect with the drive signal. The measurement was done with the reference accelerometer mounted directly on the vibration table. The delay time was less then 10 μsec for drive signal frequencies up to 1 KHz.

4.2 Measurements

In order to characterize device performance, the experimental set-up from Fig.41 was used. The device under test, DUT, and its instrumentation amplifier were connected to a DC voltage source and hence, when the sensors' resistance changes, a signal develops at amplifier's output terminals.

This signal varies accordingly to the applied acceleration. It is visualized simultaneously with the signal given by the reference accelerometer, on the oscilloscope screen. The device's response signal is synchronized in respect with the reference acceleration's signal. An amplitude reading resolution of 0.2 mV can be obtained on screen. This value is very low compared with the noise at the device's amplifier output terminals, which was 10 - 20 mV.

4.2.1.Frequency Response

The device's response versus frequency is measured at a given applied acceleration.The frequency domain of the driving signal of the vibration table for which the reference acceleration is constant is first determined.

The amplitude of the reference accelerometer is measured at different frequencies, f, of the drive signal for a given drive signal amplitude, A. I have determined experimentally that the reference acceleration is constant for 40 Hz < f < 160Hz, A = +/- 40 mV and for 36 Hz < f < 140 Hz, A = +/ - 100 mV.

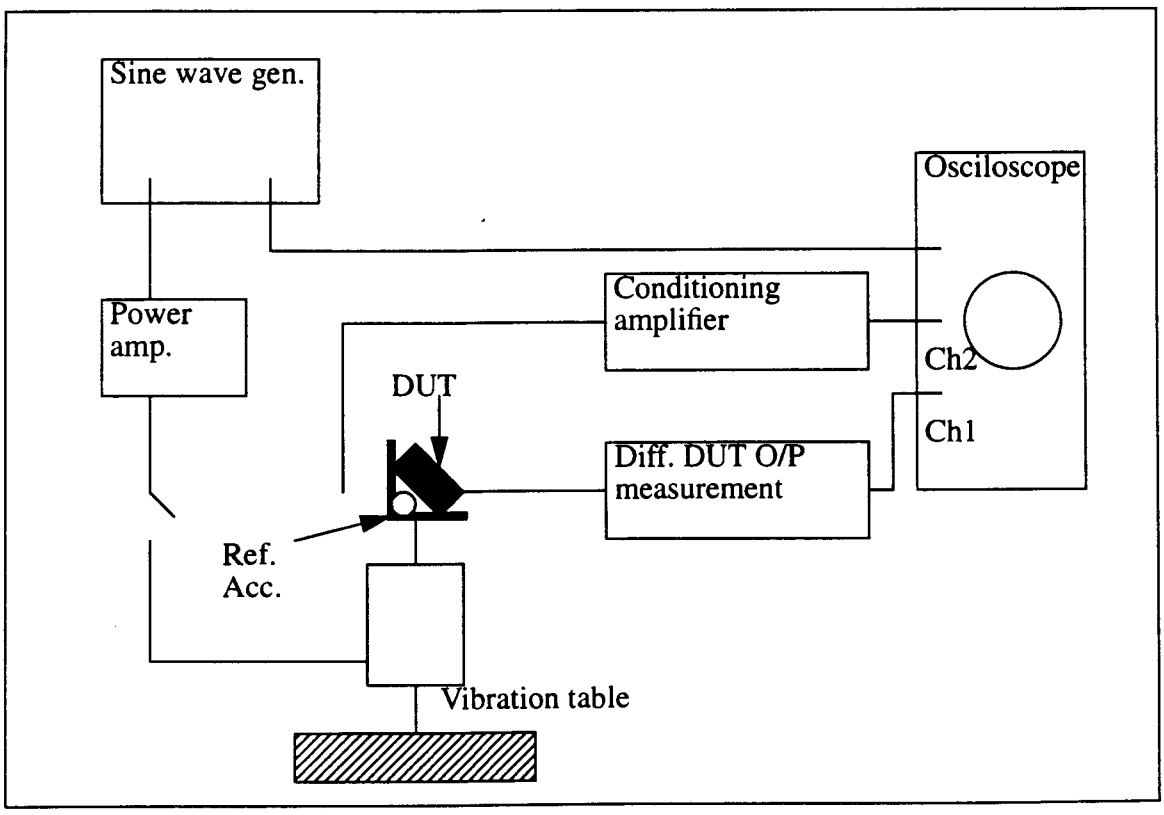

Fig.41 Experimental set-up

Then, the frequency of the drive signal is changed in steps of 2Hz or 10Hz within the above frequency ranges., keeping constant drive signal's amplitude. For each step, the delay of device's response in respect with the reference acceleration is measured.

Using the measured device's delay time value, the phase is calculated with the relationship:

$$\theta = [d / T_{ref}] \times 360 \qquad (121)$$

4.2.1a. PolySi Bridges

The heater and the sensors are polySi resistors of 14 μm width and 2000 μm length with resistance values of 20.8 Kohm for heater and 18 Kohm for sensors. Heater-sensor separation is 175 μm. The cavity depth below them is 80 μm. The high above the heater is around 1cm. The measurements were done at +/- 40 mV and +/- 100 mV drive signal's amplitude, respectively. The heater power, P_H, was a constant parameter during each set of measurements. I have been using P_H values of 45 mW, 20 mW, 11.5 mW and 5mW in my measurements. A constant acceleration of 3.55g +/- 0.1g was applied to the device. The device's response versus frequency for A = +/- 100mV is shown in Figs 42 and 43. The frequency value, f_{-3dB}, is 45 Hz for P_H= 5mW (Fig.42) and 70 Hz for P_H= 45 mW (Fig.43). These values correspond to 3.54 and 2.3 msec device's response time, respectively.

The results are in good accord with the analytical model results. Based on the analytical model, a device response time of 1.2 ms was calculated (Section 2.4.2). I have shown also that the model predicts increase of the device response time as the temperature at the sensor location decreases.

The difference between measured and calculated values of response time could be due to the SiO_2 layer around the polySi resistor which makes its actual characteristic dimension almost three times larger.

4.2.1b Silicon Resistors Device

The devices made out of Si show no response. The heater voltage varied from 1 to 5 V which corresponds to a heater power from 0.9 mW to 12 mW. The heater - sensor separation was 5 and 8 μm, respectively. The cavity depth and the high above the heater were 100 - 130 μm and ~ 1mm, respectively. The device behaved as a very sensitive flow meter, instead. Based on this, it can be concluded that the heater - sensor separation was too small for +/- 1g applied accelerations which could not induce detectable air movement in the close vicinity to the heater. Hence all the measurements were performed for the polySi devices due to the lack of response from Si resistor based devices.

4.2.2 Device Calibration and Linearity

The measurements were done recording device output and corresponding reference acceleration values, at constant drive signal amplitude and different frequencies. The frequency domain of a drive signal for which the reference acceleration was not constant has been used.

The device calibration at drive signal amplitude +/- 40mV was done for heater power values of 45, 20, and 11,25 mW, respectively. The device's calibration curve is shown in Fig.44 for P_H=20 mW, A=+/-40mV and for P_h= 11.5 mW, A= +/-40mV in Fig.45. The straight lines represents first degree polynomial fit. The device response exhibits deviation from linearity. There is mismatch between the device's response curve and a linear behavior. The error is less than 10%.

Considering the experimental results from device frequency response and device calibration, it can be concluded that the drive signal amplitude does not influence the device output.

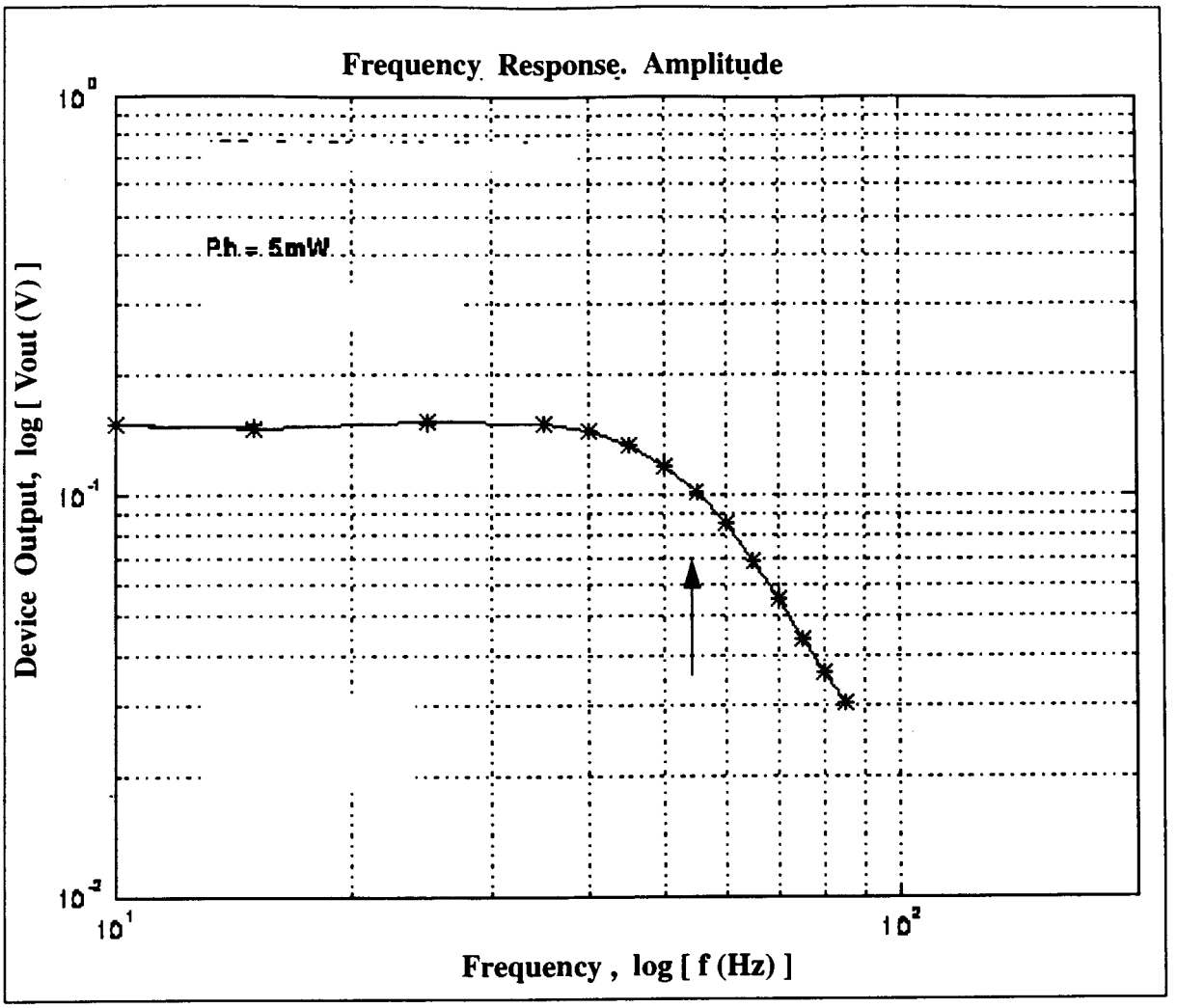

Fig.42 Device's frequency response at P_H = 5 mW. Drive signal's amplitude = 100 mV

4.2.3. Device Sensitivity

The device sensitivity, S is defined as the relative change of the output voltage per unit of applied acceleration, a or differential temperature, dT at the two sensors

$$S = \frac{V_{out}}{dT} \times \frac{1}{V_B}$$

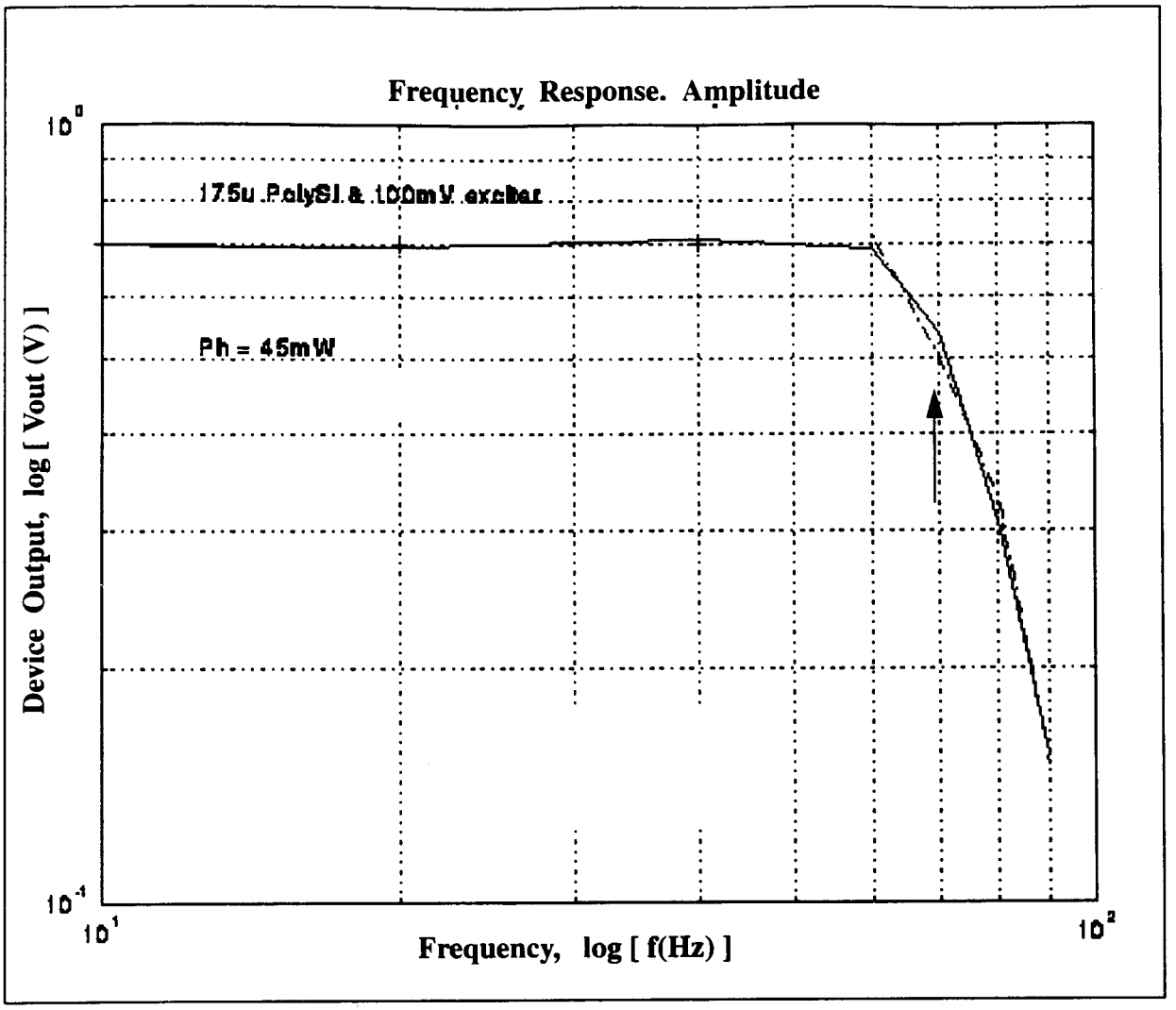

Fig.43 Device's frequency response at P_H = 45 mW. Drive signal's amplitude A = 100 mV

By substituting V_B, the sensitivity can be expressed as:

$$S = \frac{dR}{R} \times \frac{1}{T} \qquad (122)$$

so that the device sensitivity is given mainly by the temperature coefficient of its resistances.

The sensitivity was evaluated from the device calibration curves (Figs. 44 to 47). The experiment

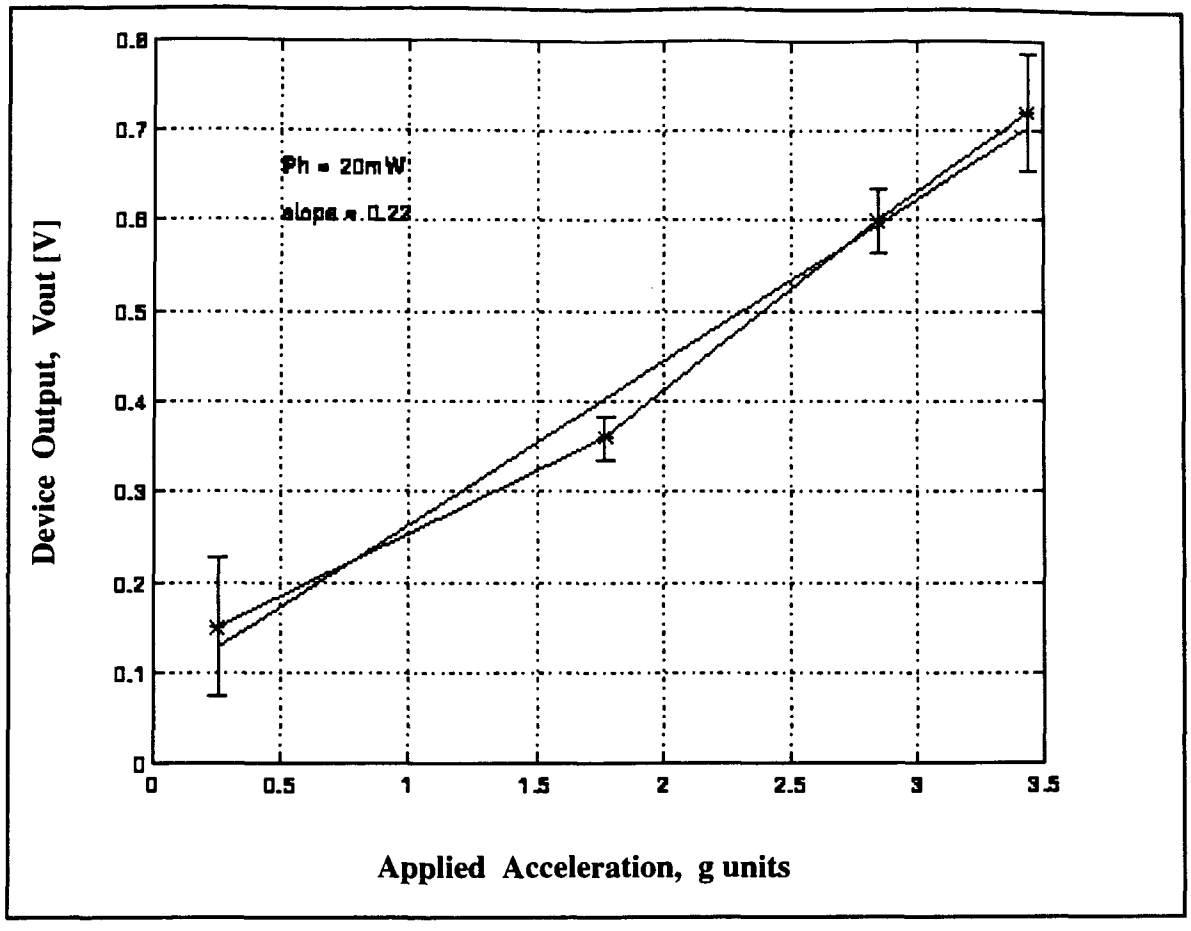

Fig.44 Device Calibration: P_H= 20 mW, A = +/- 40 mV

tal curves can better be approximated with second degree polynomials (Figs.46 to 47), thus V_{out}= c_1 a + c_2. Hence the device sensitivity is S = 2 c $_1$ a and it is changing over the measurand range.

I have calculated the device average sensitivity as the mean approximate derivative of the device calibration curve. The values are listed in Table 16.

Data from Table16 correspond to a device with a cavity depth = 80 μm, high above heater = 1cm, resistance value = 20K +/- 10% and measurement circuit gain, A_V = 1000.

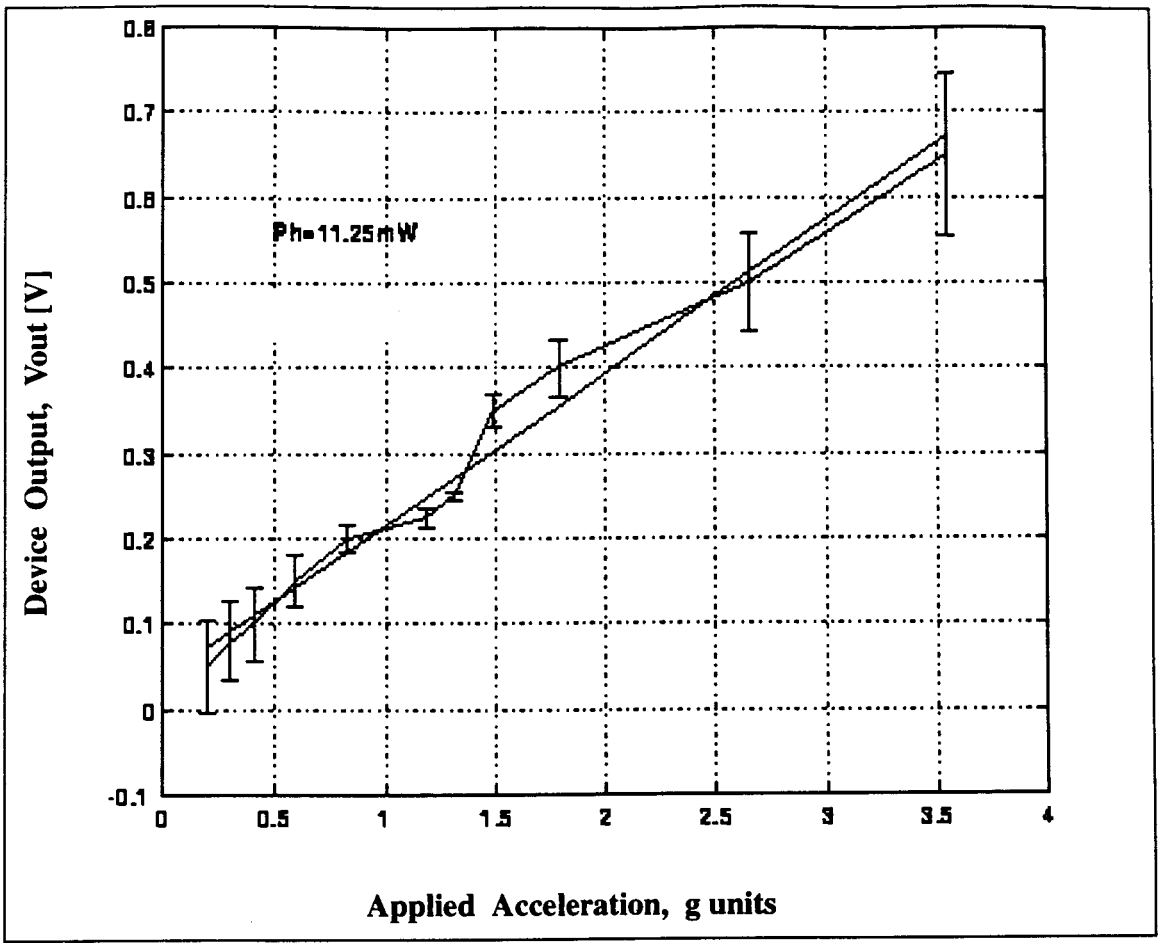

Fig.45 Device Calibration: P_H= 11.25 mW, A = +/- 40 mV

Table 16: Sensitivity vs. heater power

S [mV / m*sec^{-2}]	P_H [mW]	V_H [V]
0.50	45	+/- 15
0.22	20	+/- 10
0.17	12.5	+/- 7.5

It can be seen from Table16 that the device's sensitivity increases as heater's electric power increases. An increase in heater's electric power corresponds to an increase in heater's tempera-

ture. This in turn will determine a temperature increase at sensor location. The temperature gradient increases. Thus the temperature difference induced by an applied acceleration is increased at the same location if the heater's power increases.

I have estimated the heater and air temperatures at equilibrium using the analytical model. The values are given in Table17. A comparison of these values with those evaluated from measurements is given in Table 19.

Table 17: Heater and air temp. at 175um away vs. P_H

P_H [mW]	45	20	12.5
dT_H [° C]	300	200	100
T_{air} [° C]	78	53	36

The sensor temperature was determined experimentally, indirect, by measuring the sensor's resistance versus heater's electric power. The measurement circuit's schematic diagram is shown in Fig.48.

V_{out} corresponds to sensor's resistance change. The voltage change at sensor corresponds to a bridge differential voltage. Thus

$$dV_{SNZ} = V_{out} / A_V = [dR / R] \; x \; V_B \qquad (123)$$

where:

A_V = circuit gain = 21

V_B = bridge voltage = 5 V

dR / R = relative sensor's resistance change.

Here

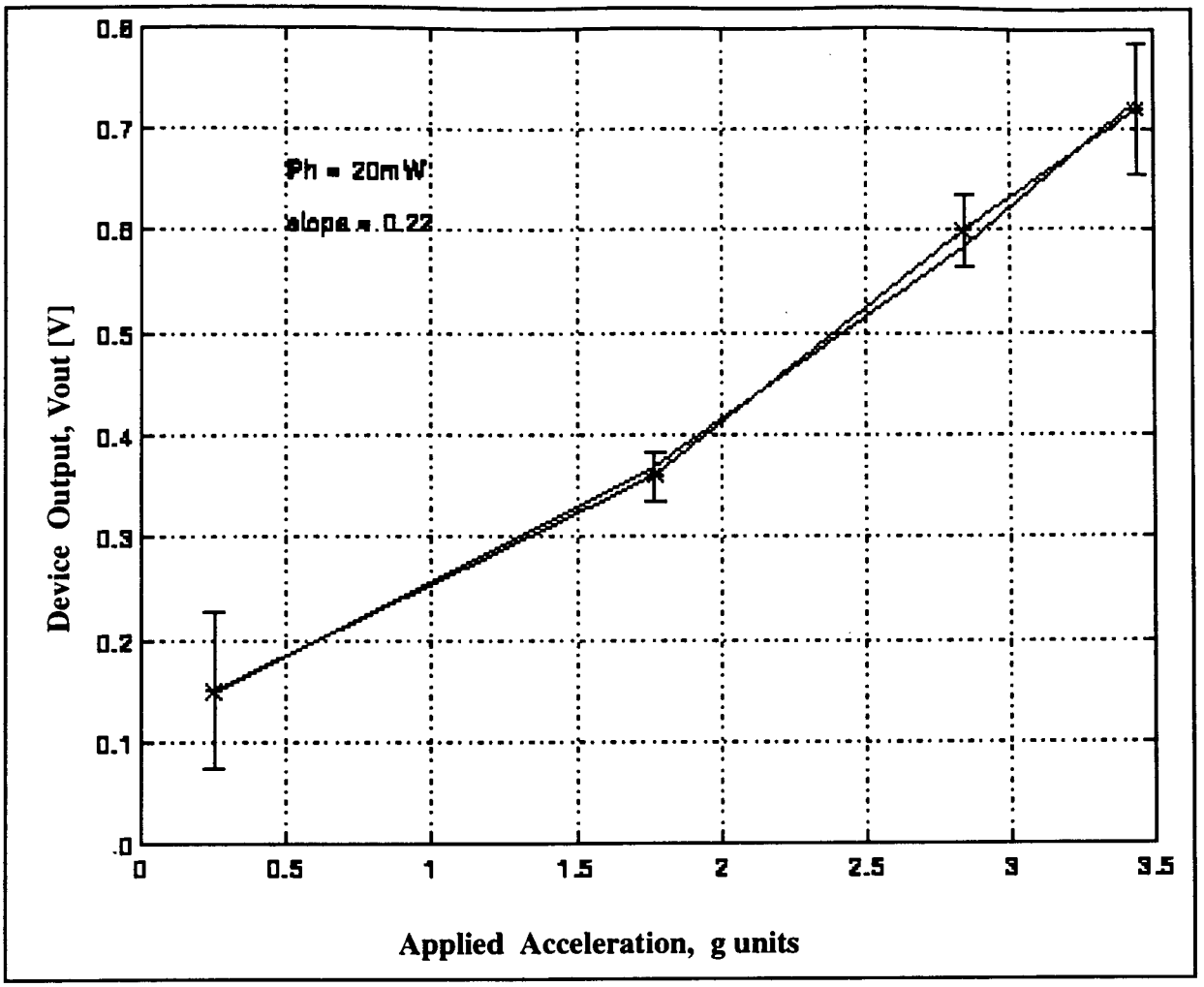

Fig.46 Device linearity: PH= 20 mW, A = +/- 40 mV

$$dR/R = TCR \; x \; dT \qquad (124)$$

with dT = sensor temperature variation

TCR = temperature coefficient of resistance = 5 x 10^{-4} C^{-1}.

By substituting eqn.124 into eqn.123, I get:

$$dV_{SNZ} = V_B \; x \; TCR \; x \; dT \qquad (125)$$

$$dV_{SNZ} / V_B = TCR \; x \; dT = 0.05 \; \% / ^{o} C \qquad (126)$$

Based on measured dV_{SNZ} values, the following sensor's temperatures were estimated:

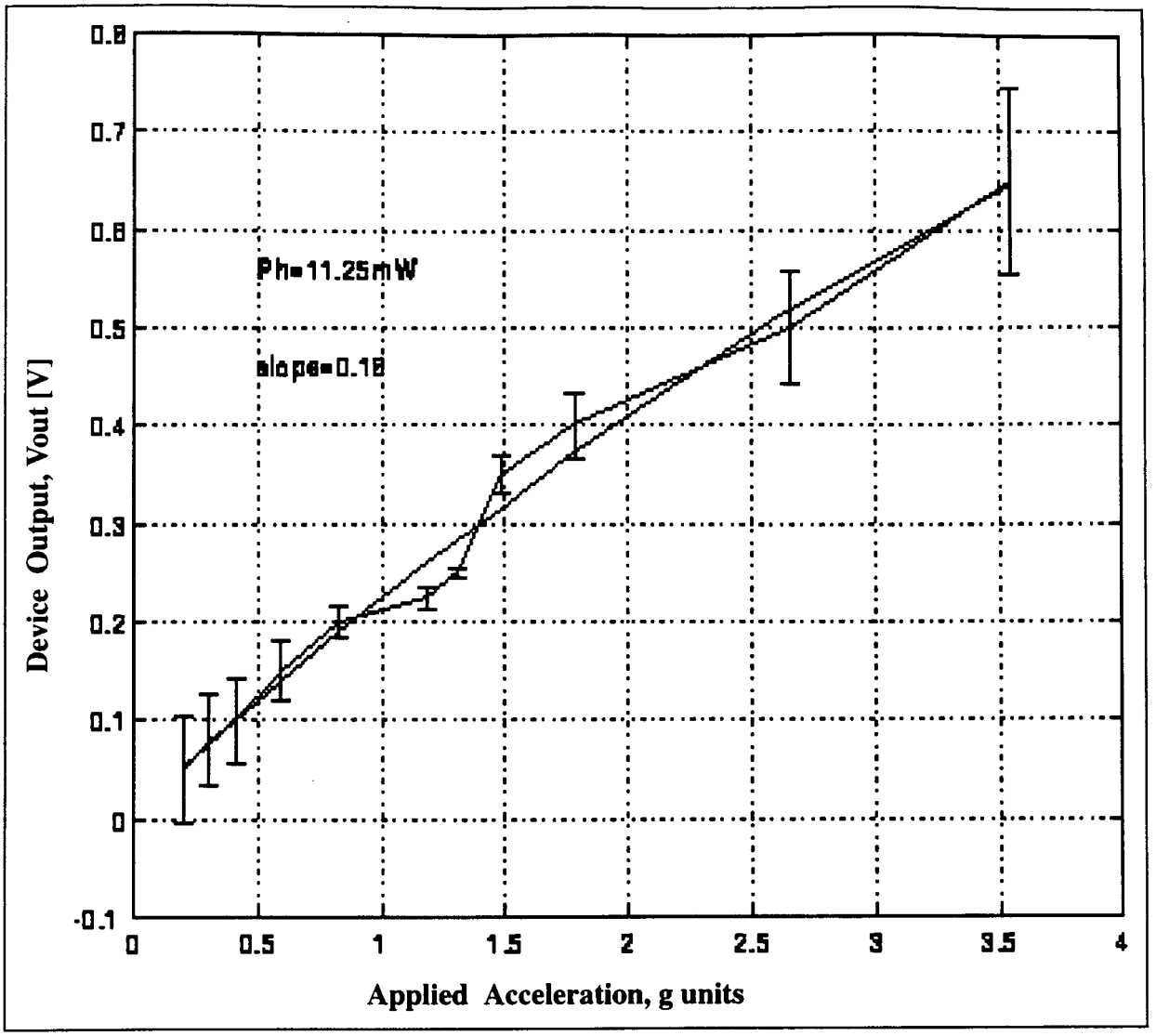

Fig.47 Device linearity: P_H= 11.25 mW, A = +/- 40 mV

Table 18: Sensor temperature evaluated from measurements

P_H [mW]	45	20	12.5
dT [° C]	78	35.2	19.4
T [° C]	98	55.2	39.4

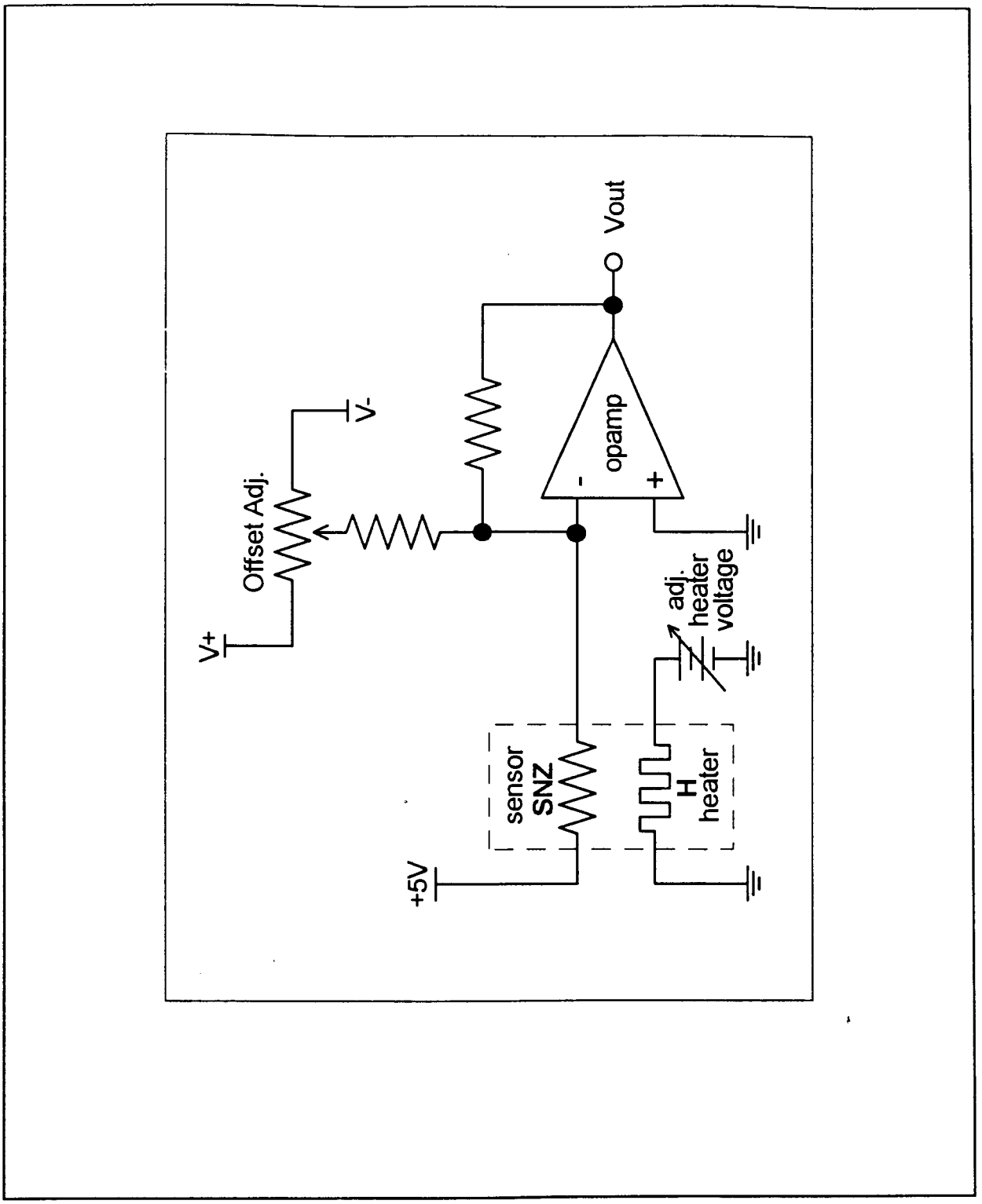

Fig.48. Schematic circuit diagram for sensor's temperature measurements

The calculated and measured temperature values are presented in the same table for comparison, (Table19). The measured values are in good agreement with those given by the analytical model.

4.2.4. Device Resolution

The minimal change of the measurand value necessary to produce a detectable change at the out

Table 19: Calculated and measured sensor temperatures

P_H [mW]	45	20	12.5
T_{model} [°C]	78	53	36
$T_{measured}$ [°C]	98	55	39

put represents, by definition, the resolution. The device resolution is determined by its sensitivity and measurement noise. The experimental measurement noise is 10 - 20 mV (output noise). The measurement resolution, Z, is calculated from experimental data as follows

$$Z = V_{noise} / S \qquad (127)$$

By substituting S values from Table16, I got the reading resolution versus bridge voltage. The values are listed in Table20.

Table 20: Reading resolution

V_B [V]	7.5	5	3.75
Z [g]	0.036	0.08	0.1

The reading resolution increases as V_B increases.

The reading resolution of sensor's temperature is calculated as follows:

For V_B = 7.5 V and dV_{out} = 1V

$$dV_{out} / V_B = 0.013\ \%$$

thus dV_{out} = 1V represents 0.013% in respect with V_B. From eqn.126, dT = 0.013 x 20 ° C = 0.26 ° C. or 0.1 V output voltage for 0.026 ° C temperature change at sensor's location.

For this measurement conditions, V_B = 7.5 V, V_H = +/- 15V, A_V = 1000 and the device sensitivity is S = 0.5 V / g. Hence the output voltage change per unit g corresponds to a temperature change per unit g of

$$dV / g = 0.5\ x\ 0.26\ /\ 1 = 0.13\ ^{o}C / g.$$

This value is in very good accord with that given by the analytical model, 0.1 ° C (Section 2.3.2). The calculated values are based on average sensitivity data. Device resolution and temperature reading resolution at different bridge voltages are listed in Table21.

Table 21: Acceleration and temperature resolution

V_B [V]	7.5	5.0	3.75
Z [g]	0.036	0.08	0.1
Z_{temp} [° C	0.13	0.09	0.096

4.3 Measurand Range

The measurand range is the measurand interval of values over which the sensor is intended to measure. Since the moving component in the device structure is the air, the upper limit of applied acceleration without damaging the device is that given by the mechanical resistance at shocks of the suspended bridges. Due to device working principle, there should be no limitation for device functioning at high accelerations. The maximum applied acceleration during device testing was

+/-5g, value determined by the experimental set-up. No damaging of the device was observed.

The bridge oscillations at high acceleration, vibration levels might be possible. These would induce resistance variations due to piezoresistive coefficient of silicon or polysilicon, respectively. Metal resistors do not exhibit this susceptibility, thus it would be more appropriate for device working at high acceleration levels.

The measured device sensitivity was 0.1 to 0.04 g. Thus a minimum of 0.04 g can be measured with the present device configuration. Further optimization could lead to 0.001g level device sensitivity.

The estimated device measurand range is 0.01 to 10 g.

Chapter 5. Conclusions

A new type of thermal accelerometer fabricated by application of bulk micromachining technique has been demonstrated in this thesis.

Layout and design criteria were presented.

Analytical models were developed to describe device behavior based on its simplified representations. The device response time and temperature values at sensors location predicted by the analytical models are in good agreement with the experimentally determined values.

Device simulations were performed to get insight into device behavior and to compare simulation and analytical results. Simulation results show device behavior similar to that given by the analytical models. The main heat transfer mechanism is conduction with buoyancy effects taking place in the far field region. For heater's characteristic dimensions in the few microns range, the boundary layer assumption is no longer valid. The temperature field around the heater is split into near and far field, with conduction being the predominant heat transfer mechanism in the near field. This behavior prevent devices made with narrow (within near field width) heater - sensor separation to work.

The sensor temperature's values given by the simulation results are different within 20% from those based on analytical calculation. The differences can be attributed to the fact that simulations take into account all air properties changes with temperature, while analytical models consider only air properties at $T_{average} = [\ T_H + T_{ambient}\ ] / 2$.

Two device's type were fabricated using bulk micromachining technique. Micromachined SiO_2 bridges sandwiching a polySi resistor were employed as temperature sensors to measure the device's acceleration. Resistors made out of heavily B-doped silicon bridges were also used as temperature sensors. Both device types were characterized.

Silicon suspended resistors exhibit potential advantages of minimum width, high TCR, thus fast response and high sensitivity. Also, the TCR of Si resistors is almost constant over a wide temperature range. Fabricated devices based on Si bridge structures behaved as very sensitive flow meters, showing no response to applied accelerations in +/- 1g range. The lack of response may be due to close proximity ($5\mu m$ and $8\mu m$, respectively) of sensors to the heater, which might prevent sensing of air movement. Thus all measurement results are for polySi resistors device type.

The measurement set-up for device characterization was configured using a miniature vibration table. Known accelerations were applied to the device under test. The two device's temperature sensors were placed into an Wheatstone bridge configuration operated at constant voltage. Electrical signal output from the resistor bridge was amplified using a standard instrumentation amplifier configuration. The amplified signal was visualized and measured on a two channel oscilloscope. Applied accelerations ranging from +/- 0.1g to +/- 5g were measured with an accuracy of 0.04g. A device response time of 3.18 msec was determined based on its -3dB frequency values. This experimental value is in a fairly good accord with the value of 1.2 msec predicted by the analytical models. The difference between measured and calculated values of the response time is mainly due to a difference in actual characteristic dimension of temperature sensor. The SiO_2 layer around the polySi resistor makes its actual characteristic dimension about three times larger.

The device's sensitivity was evaluated from device's calibration curves. An average sensitivity of 0.2mV / g was experimentally determined. Experimental data have been shown that the device's sensitivity is a function of heater power. It increases as heater power increases, at a given TCR of

temperature sensors. A sensitivity of 0.5 mV / g was measured for P_H = 45 mW.

The device response is almost linear. The deviation from a linear behavior may be due to a change in TCR with temperature change.

The new accelerometer's structure presented in this work has two main advantages over the existing devices. One is that the device has no moving solid parts. That makes it robust and reliable. The second is that the device's sensing range and sensitivity can be adjusted, for the same physical device's configuration, by changing the heater's electric power. The heater's temperature can be maximized to measure the smallest acceleration which can be detected for a given accelerometer size. The same accelerometer can be used to detect larger accelerations by reducing the heater's temperature. Thus both high and low-g acceleration ranges are available with the same device. This is a distinctive feature of the new proven structure compared with the existing ones, which can be used only for either low or high-g levels. Another advantage of the new device is its simplicity,. which makes it less costly and easy to fabricate.

Some of the demanding applications of acceleration sensors are in automated manufacture, automotive and other vehicles, vibration and seismic monitoring and in scientific measurement. The new device can be used as a durable and inexpensive sensor in car air-bag actuators as well as other automotive sensors (suspension systems, locks). Another possible applications are tennis balls impact acceleration detection and vibration monitoring.

References List

1. S.M.Sze, "Semiconductor sensors", John Wiley & Sons Inc. ,(1994).
2. Prof.Dr. Albert Leung, patent application, June 1996.
3. "Precision Sensors Interfaces", Analog Devices, (1990).
4. Mitel -MEMs, Internal Report, (1994).
5. Prof. Dr. John Jones, 1994 - 1996 Memos.
6. G.C.M. Meijer, A.W. van Herwanrden, " Thermal Sensors ", Adam Hilger, Bristol, (1994).
7. F.Kreith, W.Z.Black, " Basic Heat Transfer ", Harper & Row, Publishers, New York, (1980).
8. B.Gebhart, Y.Jaluria, R.L.Mahajan, B.Sammakia, " Buoyancy -Induced Flows and Transport", Hemisphere Publishing Corp., Springer - Varlag, (1988).
9. B.V.Karlekar, R.M.Desmond, " Engineering Heat Transfer ", West Publishing Co., St.Paul, Minn., (1977).
10. H.S Carslaw , J.C. Jaeger, " Conduction Heat Transfer", Clarendon Press, Oxford, 2nd Edition, (1959).
11. J.H.Lienhard, " A Heat Transfer Textbook ", Prentice Hall,(1981).
12. R.Hiratsuka, D.C.van Duyn, T.Otaredian, P.de Vries, " A novel Accelerometer Based on a Si Thermopile ", Solid State Technology, (1991).
13. A.Bajtsa et.co., "Thin Film Resistor Thermometers for Use in Aggressive Surroundings ", Sensors and Actuators, A30, (1992).
14. "PolySi as a Material for Microsensors Applications ", Sensors and Actuators, Oct.1991.
15. N.C.MacDonald, "Selective Chemical Vapor Deposition of Tungsten for MEM Structures ", Sensors and Actuators, 20, (1989).
16. S.Bouwstra, "Resonating Microbridge Mass-Flow sensor", Sensors and Actuators, A21 - 23, (1990).
17. S.Bouwstra et.co., "Resistivity and Gauge Factor for In-Situ P-Doped PolySi ", Sensors

and Actuators, A30, (1992).

18. K.Petersen, J.Bryzek, W.McCulley, "Micromachined made of Silicon ", Spectrum, May 1994.
19. G.A.McDonald, "A Review of Low Cost Accelerometer for Vehicle Dynamics ", Sensors and Actuators, A21 - 23, (1990).
20. A.W.van Hervaarden, D.C.van Duyn, B.W.van Oudheusden, P.M. Sarro, " Integrated Thermopile Sensors ", Sensors and Actuators, A21 - 23, (1989).
21. K.E.Petersen, "Silicon as a Mechanical Material ", Proc. of IEEE, 70, (1982).
22. D.W.Huges, "Polycrystalline Silicon Resistors for Use in ICs", Solid State Technology, May (1987).
23. M.Parameswaran, A.M.Robinson, Lj Ristic, K.Chau, W.Allegretto, " A CMOS Thermally Isolated Gas Flow Sensor", Sensors and Materials, 2,1, (1990).
24. M.Parameswaran, H.P.Baltes, A.M. Robinson, "PolySi Microbridge Fabrication Using Standard CMOS Technology", Digest of Techn. Papers, IEEE Solid State Sensors and Actuators Workshop, Hilton Head Island, SC, June 6-9, (1988).
25. H.Seidel, "The Mechanism of Anisotropic Si Etching ", Digest of Techn. Papers, 4th Int. Conf. on Solid State Sensors and Actuators, Tokyo, Japan, June 11-14, (1987).
26. C.Lu, M.Lemkin, B.E.Boser, "A Monolithic Surface Micromachined Accelerometer with Digital Output", IEEE Journal of Solid State Circuits, Dec.1995.
27. O.Tabata, K.Kawakata, Ugiyama, I.Igarashi, " Mechanical Property Measurements of Thin Films Using Load - Deflection of Composite Rectangular Membranes ", Sensors and Actuators, 20, (1989).
28. Yu.C.Tai, R.S.Muller, " Lightly - Doped PolySilicon Bridge as a Flow Meter ", Sensors and Actuators, 15, (1988).
29. S.Bouwstra, R.Legtenberg, Harrie A.C.,Tilmans, M.Elvenspoek, " Resonating Microbridge Mass Flow sensor ", Sensors and Actuators, A21 -23, (1990).
30. B.W.van Oudheusden, " Silicon Thermal Flow Sensors", Sensors and Actuators, A30, (1992).

31. S.Middelhock, S.A.Audet, "Silicon Sensors ", Academic Press, London, (1989).

32. W.Minkina, "Non - Linear Models of Temperature Sensor's Dynamics ", Sensors and Actuators, A30, (1992).

33. D.C.Satchell, J.C.Greenwood, "Silicon Microengineering for Accelerometers ", Proc.Instr. Mech.Eng., 1987-2, Mechanical Technology of Inertial Devices, UK, Apr.7-9, (1987).

34. H.Guckel, D.W.Burns, H.A.C.Tilmans, "Mechanical Properties of Fine Grained PolySi", Tech.Digest, IEEE Solid State Sensors and Actuators Workshop, Hilton Head Island, SC, USA, June 6-9, (1988).

35. H.Huraoka, T.Ohhaashi, Y.Sumitomo, "Controlled preferential Etching Technology ", in Semiconductor Silicon 1973, H.R.Huft and R.R.Burgers Eds.

36. "A Surface - Micromachined, Monolithic Accelerometer ", Analog Devices, 27, 2, (1993).

37. F.Volklein, H.Baltes, "Thermoelectric Properties of PolySi Films Doped with P and B ", Sens.Mater., 6, (1992).

38. A.Bejan, "Convective heat transfer", 2nd ed., NY, John Wiley, (1994).

39. T.Baumeister, E.Avallone, "Mark's Standard Handbook for Mechanical Engineers", 8th ed., p.S-67 to S-76.

40. Bruel & Kjer's Manual : "Measuring Vibration", Sept.1982.